Amorphous Selenium (a-Se) and Its Compounds: Photo-Induced Metastability and Application in a Novel Gamma Camera

A Dissertation Submitted

by

Anastasiia Mishchenko

to

Faculty of Graduate Studies

in Partial Fulfillment of the Requirements of

the Degree of

Doctor of Philosophy

in the Subject of

Chemistry and Materials Science,

Lakehead University

Thunder Bay, Ontario, Canada

Abstract

Despite the large number of successful commercial applications of chalcogenide glasses (ChGs) ranging from memory devices to photonics and medical imaging detectors, the understanding of a fundamental property – photo-induced structural metastability is not yet complete. The inherent trend of amorphous chalcogenides to convert to its crystalline counterpart, can on the one hand, be directly utilized in phase-change memories, while on the other hand can degrade glass properties for applications in sensing. Furthermore, because the structure of amorphous semiconductors is not fixed by thermodynamic equilibrium conditions, its transformation can be triggered by optical/X-ray excitation and influenced by thermal heating or applied electric field. Each case has its own peculiarities of transformation. Thus, to ensure effective application of a given ChG, a solid understanding of the causes for the structural transformation on the microscopic level has to be developed.

This thesis is devoted to the study of photo-induced metastability of the most widely used ChG – amorphous selenium (a-Se), and archetypal a-Ge_xSe_{100-x} glass compounds relevant for applications in sensing. We focus on the research of defect creation and defect relaxation processes in these materials since it is hypothesized to be the root cause for structural transformations affecting stability. The detailed experimental and theoretical study is carried out to reveal the pathways from a micro-level, i.e. defect creation/relaxation, to the macro-level photo-induced effects formation, namely photodarkening (PD), photobleaching (PB) and photo-induced crystallization (PC) and their kinetics.

The effects of temperature and energy of excitation on PD kinetics are studied in a-Se. Distinctly different PD effects are observed in the case of sub-bandgap and above-bandgap excitation. It is found that above-bandgap excitation causes only transient photodarkening with a temperature independent relaxation time and no significant structural rearrangements. In contrast, sub-bandgap excitation causes both transient and metastable PD effects. Whereas the mechanism responsible for transient PD for sub-bandgap excitation is analogous to that in the case of above-bandgap excitation, metastable PD is controlled by the formation of self-trapped excitons resulting in

structural transformations into configuration defects. Subsequent relaxation in the latter case is shown to be a thermally activated process at elevated temperatures; or configuration tunneling below the room temperature. It is confirmed that if left unrestored, metastable PD acts as a precursor for photo-induced crystallization.

Detailed investigation of the effects of different substrates and temperature on photo-induced crystallization in a-Se demonstrates that the onset of PC is suppressed by softening of the film-substrate interface and/or by operating at temperatures near the glass transition.

Further, photodarkening and photobleaching effects are investigated in a-Ge_xSe_{100-x} as a function of composition across the glass forming region. The Ge:Se ratio is found to play a decisive role in the observed effects. The critical concentration of Ge ≈30% is highlighted to correspond to the crossover from transient PB to a mixture of transient PD and metastable PB. The underlying microscopic mechanism is governed by the availability of lone pair (LP) states at Se atoms. For low-Ge content films (x<20%) LPs are primarily involved in photoexcitation, causing a photodarkening effect (like in a-Se). As Ge concentration reaches 30%, Ge-Se bond breakage becomes prevalent under light exposure, which results in the generation of dangling bonds and the saturation of the available LP states. This is found to be responsible for the transient PB effect. With further increase of Ge %, the amount of homopolar Ge-Ge bonds starts to increase along with the obvious deficiency of lone pairs. This leads to Ge-Ge bond breakage upon excitation, which causes transient photodarkening. In the post-excitation period, however, it initiates transition to a more ordered state with the main feature of the formation of 3D nanostructures. This is reflected in a bandgap increase and an experimentally observed metastable photobleaching effect.

Finally, our understanding of a-Se properties allowed us to extend its application in low-energy nuclear medicine devices. A novel fluence integrating gamma camera is proposed, which if commercialized, will be used to guide advanced breast cancer treatment that involves the placement of low-energy radioactive seeds. The feasibility of the proposed approach is confirmed in realistic breast phantom studies. Our results demonstrate the potential of the gamma camera to fulfill the clinical requirements of both spatial resolution and sensitivity.

Acknowledgement

Firstly, I would like to express sincere gratitude to my advisor, Prof. Alla Reznik for providing me with learning environment and opportunities to grow as a scientist; for her support, guidance and encouragement throughout the course of my PhD studies.

I am grateful to Dr. Olivier Tousignant for introducing me to the field of digital mammography, organizing my Internship at Analogic Canada; for his mentorship, shared expertise, encouragement and support.

I acknowledge Lakehead University and Thunder Bay Regional Research Institute communities; Physics department for the opportunity to teach lab components and assist in teaching thermodynamics. I thank Giovanni DeCrescenzo and Sergey Reznik for their coaching on different experimental techniques. I am thankful to Vlad Sukhovatkin for the chance to work on XLV detectors and for his willingness to support my development as a researcher. I acknowledge collaboration with Dr. Maria Mitkova (Boise State University) and Dr. Bernard A. Weinstein (SUNY at Buffalo) for the joint work, valuable scientific discussions, access to the research facilities and samples. I thank my colleagues at Analogic Canada for the great working and learning environment. I would like to recognize that this research would not have been possible without NSERC, ORF-Research Excellence program and Ontario Graduate Scholarship, who provided me with funds for international students in Canada.

Many thanks go to all my closest Ukrainian and Canadian friends with whom many moments of this journey were joyfully shared.

I am deeply grateful to my family Roman, Nadiia and Igor Mishchenko, for their love, care and presence throughout my life; for their understanding and support of my choices in life and in particular of this 4-year endeavor.

Last but not least, I believe that true gratitude becomes possible when one realizes the great gift of own life and learns to appreciate every challenging moment and change on the way towards highest, truest self. I embrace the desire of own mind and strength of own body to strive for the new and unknown.

Table of Contents

Abstract i

Acknowledgement iii

Table of Contents iv

List of figures vii

List of abbreviations and symbols xi

CHAPTER 1. Introduction and thesis scope 1

1.1. Chalcogenide glasses and their applications 1

1.2. Significance of photo-induced metastability for practical use of ChGs 4

1.3. Thesis scope 5

CHAPTER 2. Properties of a-Se and its compounds 7

2.1. Basic properties of a-Se 7

2.1.1. a-Se atomic structure 7

2.1.2. Raman spectra of a-Se 12

2.1.3. Density of states and role of the disorder 16

2.1.4. Defect classification in a-Se 19

2.2. Basic properties of Ge-Se glasses 24

2.2.1. Ge-Se bonding configurations 25

2.2.2. Raman spectra for a-Ge_xSe_{100-x} 27

2.2.3. Density of states in Ge-Se glasses 29

2.3. Photo-induced metastability in ChGs 31

2.3.1. Photodarkening and photo-induced crystallization in a-Se 32

2.3.2. Photodarkening and Photobleaching in a-Ge_xSe_{100-x} 40

CHAPTER 3. Experimental techniques and setup details 43

3.1. Two-laser beam technique for PD/PB study 43
3.2. Raman spectroscopy 45
3.2.1. Setup details for Ge-Se light-induced effects study 45
3.2.2. Setup details for a-Se photo-induced crystallization study 46
CHAPTER 4. Photodarkening and Photocrystallization in a-Se 48
4.1. Photodarkenig in a-Se 48
4.1.1. Experimental results and discussion on PD in a-Se 49
4.1.2. First-principle simulation of photo-excitation and subsequent relaxation 56
4.1.3. Conclusion 62
4.2. Photocrystallization in a-Se layers 63
4.2.1. Spatial mapping of PC profiles 64
4.2.2. Temperature dependence of PC onset 70
4.2.3. Discussion and summary 72
CHAPTER 5. Photodarkening and Photobleaching in a-Ge_xSe_{100-x} 76
5.1. Experimental results on two-laser beam technique combined with Raman analysis 76
5.2. First-principles simulation results and Discussion 81
5.2.1. a-Ge_xSe_{100-x} structural evolution up to 30% of Ge content and respective light-induced effects 82
5.2.2. a-GexSe100-x network peculiarities for x≥30%. Insights into the mechanism of the metastable changes 85
5.3. Conclusion 87
CHAPTER 6. Application of a-Se in a novel gamma camera for low-energy imaging ... 89
6.1. a-Se FPXI for digital mammography 89
6.2. Radioactive seeds procedures in breast cancer management 94

6.2.1. Radioactive Seed Localization, requirements for image guidance. 95
6.2.2. Permanent Breast Seed Implantation, requirements for image guidance..... 96
6.3. Novel a-Se based gamma-camera 98
6.4. Proof of concept studies 100
6.4.1. Experimental setup 100
6.4.2. Results and discussion 101
6.5. Conclusion and future work 103
CONCLUDING REMARKS 105
APPENDIX 108
APPENDIX A. Samples preparation 108
A.1. a-Se deposition 108
A.2. a-Ge_xSe_{100-x} deposition 110
APPENDIX B. List of Publications and Presentations from Thesis Research 111
B.1. Journal publications 111
B.2. Conference presentations 111
REFERENCES 112

List of figures

Figure 1. Schematic representation of Se atom bonding configuration, in case of two covalent bond formation with another Se atom (arrows is grey correspond to electrons of the other Se atom). 7
Figure 2. Left: trigonal or hexagonal Se [32]; Right: monoclinic α -Se [33]. 8
Figure 3. Schematic representation of a-Se local molecular order, where chain-like segments are characterized by same phase of dihedral angle and ring-like fragments by the alternating one [34]. 10
Figure 4. Cis- and trans- coupling configurations for molecular bonding in Se, re-drawn from Ref. [39]. 10
Figure 5. Two adjacent chains of a simulated a-Se structure [25]. 11
Figure 6. Typical Raman spectra featuring main vibrational modes of amorphous or glassy Se (g-Se) (lower part) with corresponding vibrational density of states (VDoS) (upper part) [30]. 13
Figure 7. Cis- and trans- coupling configurations for molecular bonding in Se with corresponding frequencies of atomic displacement [41] 14
Figure 8. Raman spectra obtained in a-Se under illumination for various exposure times, from 1.3hrs to 7.4hrs [46]. 15
Figure 9. Schematic density of states (DOS) distribution in amorphous semiconductors. 16
Figure 10. a-Se DOS by M. Abkowitz (1988) [51]. 18
Figure 11. Generalized DOS for pure and stabilized a-Se (stabilization refers to alloying with ≈0.5% of As and doping with Cl in ppm range). The central part indicates the total concentrations of deep traps for electrons and holes whose energy distributions were not resolved due to the limitations of applied methods [56]. 19
Figure 12. Electronic configurations for possible bonding types in lone-pair semiconductors with corresponding energetic positions. On the left: straight lines correspond to σ orbitals, lobes to LP orbitals and circles to anti-bonding orbitals. On the right: Eb is the bonding energy, Δ destabilization energy due to bonding/antibonding states splitting, U_{σ^*} and U_{LP} increase in energy when electron is placed on σ^* or LP orbital due to electronic correlation [64]. 22
Figure 13. Different types of VAP defects: (a) two-chain VAP; (b) IVAP and (c) IVAP pair [56]. 23
Figure 14. Schematic representation of $GeSe_4$ tetrahedra unit and Se-Se fragments in germanium selenide amorphous network. 25

Figure 15. Illustration of corner-sharing (CS), edge-sharing (ES) configurations of $GeSe_4$ tetrahedra; and ethylenelike (ETH or ET) Ge-Ge homopolar bond configuration. 26
Figure 16. Elastic phases of Ge_xSe_{100-x} glasses showing evolution from flexible to rigid, nanoscale phase separation (NSPS) phase [66]. 27
Figure 17. Raman spectra of Ge_xSe_{100-x} with glass compositions given alongside the spectra [78]. 28
Figure 18. Normalized fraction of ES:CS species vs. atomic % of Ge. Dots represent experimental data [81] and solid line represents theoretical prediction [76]. 29
Figure 19. Electronic density of states for different Ge-Se compositions [79]. 30
Figure 20. Compositional variation of optical band gap in Ge-Se glasses, reported by different research groups, where E_{53} corresponds to absorption coefficient $5x10^3cm^{-1}$ and E_T to Tauc edge [66]. 31
Figure 21. Energy- configuration model for PD effect. X corresponds to the lowest energy initial ground state, Z to the excited state and Y to the metastable state responsible for the photodarkening effect. 34
Figure 22. Potential diagram describing an excitation of the A state and contribution of the photoinduced lattice relaxation into the stabilization of the excited state A*. The energy scale reflects the total energy of a system [25]. 35
Figure 23. Schematics of local structural disordering and transformation as the result of light irradiation [44]. 36
Figure 24. Thermal behavior of the PC onset times. On the left: comparison of typical and post-exposed a-Se Raman spectra at given temperatures and time of illumination. On the right: PC T-regimes [46]. 38
Figure 25. Experimental apparatus for PD temperature-dependent measurements carried out on a-Se samples. 44
Figure 26. PD for selected temperatures: -20^0C, 20^0C, 45^0C in the case of 655nm excitation. 49
Figure 27. PD for selected temperatures: -40^0C, 0^0C, 30^0C in the case of 405nm excitation. 50
Figure 28. (a) Single-exponential fit of the 3rd restoration cycle in case of above-bandgap excitation. (b) Double-exponential fit of the 3rd restoration cycle in case of sub-bandgap excitation; equations of the respective fitting curves with characteristic times τ_1 and τ_2 are displayed. 52
Figure 29. Characteristic relaxation time τ_2 vs. temperature. The dotted curve gives the best fit to Eq.4. 54

Figure 30. The VAP defects with a distribution of a net charge (a) two-chain VAP defect. (b) Single IVAP defect; the C_3^+ site corresponds to the threefold coordinated site for which the third bond between the C_{13}^- and C_3^+ sites is elongated (denoted by the dashed line) due to the strong dipole moment. (c) Pair of IVAP defects; the bond between the C_{13}^- and C_3^+ sites is shortened as the defect dipoles are partially compensated due to defect pairing..... 58
Figure 31. Photoinduced crystallization of the increased crystalline order system. The final state is t-Se containing the IVAP defect..... 61
Figure 32. Microphotographs of PC-spots in two a-Se/ITO/Glass samples: a) spots created by laser-light incident on the glass (LH) and film (RH) sides; b) reflection image of RH spot; c) and d) analogous images of a PC-spot in another a-Se/ITO/Glass sample; and e) high-power view of t-Se cylindrites in latter spot..... 65
Figure 33. Raman map of PC-spot in an a-Se film on Si, profiling the intensities of the t-Se (green) and a-Se (red) Raman peaks. RH inset shows a y-axis scan at x=17.5μm (white line) giving the fraction of the total intensity contributed by each peak. LH inset is a blow-up of a-Se/t-Se boundary. Probing laser was focused at the film-air interface. 66
Figure 34. AFM maps of same PC-spot shown in Figure 31(a) and (b) 3d-views from two angles; dashed black circles outline t-Se high-content region in Figure 31(c) Depth profile across spot center..... 67
Figure 35. Model of change in morphology under the focused laser spot for saturated growth of PC in an a-Se film on a rigid Si substrate. A boundary through forms due to the density increase in t-Se..... 68
Figure 36. Results of attempt to produce PC in an aged a-Se/ITO/Glass sample. (a) 3d-AFM profile of a laser-induced spot; (b) Raman map of 10μm^2 area around spot. Only a-Se (in red) is found. Inset is y-axis scan at x=4.2μm of a-Se and t-Se A1 intensities; (c) 3d-AFM map of subsequent swelling in a-Se phase caused by Raman probe. 69
Figure 37. Comparison of the effect of T on the Raman-observed PC onset times in (a) an a-Se/ITO/Glass sample, (b) a similar sample fabricated in a different laboratory, and (c) an a-Se/Glass sample. Note jump in the onset time on heating through Tg in each sample..... 71
Figure 38. Time evolution of (a) $Ge_{29.2}Se_{70.8}$ film transparency shows transient PB; (b) $Ge_{32.1}Se_{67.9}$ and $Ge_{39.5}Se_{60.5}$ demonstrate mixture of: transient PD (during pump cycle) and metastable PB (during rest period). 77

Figure 39. Raman spectra of the virgin and post-illuminated films with the following compositions: (a) $Ge_{29.2}Se_{70.8}$ and (b) $Ge_{32.1}Se_{67.9}$. 79
Figure 40. Raman spectra of the virgin and post-illuminated $Ge_{39.5}Se_{60.5}$. 80
Figure 41. Observed structural changes in $Ge_{29.2}Se_{70.8}$, $Ge_{32.1}Se_{67.9}$ and $Ge_{39.5}Se_{60.5}$ films before and after light exposure, as determined through integration of deconvoluted bands in Raman spectra with curve-fitting error: (a) ES/CS ratio; (b) ETH bonds; (c) Se-Se. 80
Figure 42. (a) The $Ge_{19}Se_{81}$ structure possesses high amorphicity with almost uniform distribution of the atoms. (b) The $Ge_{28}Se_{72}$ system is distinguished by the well-defined layered structure and appearance of the Ge-Ge bond. 83
Figure 43. The photo-induced transition of the $Ge_{36}Se_{64}$ system to a more ordered state. (a) Pre- excitation regime: the layered structure with weakly defined molecular cages. (b) Post- excitation regime: clustering of the molecular cages into 3D nanostructures. 86
Figure 44. Left: schematics of AMA in combination with a-Se layer, peripheral electronics and computer enabling sensor operation. Right: individual pixel schematics, including: top and bottom electrodes and *n-i-p* a-Se structure, TFT, storage capacitor and glass substrate**.** 92
Figure 45. X-ray images of the breast and hand acquired by Analogic a-Se flat panel X-ray imagers [171]. 93
Figure 46. PBSI procedure, showing treatment planning on the right and illustration of the actual procedure on the left. 97
Figure 47. Experimental setup: (a) schematic representation of all setup components; (b) example of the phantom mimicking dense breast tissue with the implanted radioactive Palladium-103 seeds at different depth and separation distance..... 100
Figure 48. Left: Analogic Large Field of View AXS-2430 a-Se digital X-ray sensor. Right: specially designed lead collimator enclosed in aluminum ring for safety considerations..... 101
Figure 49. Images of 4 seeds separated by 5, 10, 15mm in a phantom mimicking 1cm, 2cm and 4cm of fatty breast tissue, phantom-to-detector distance is 7cm. 102
Figure 50. An example of Gaussian fit of the imaging profiles from Figure 49: four seeds separated by 5, 10 and 15mm in a phantom mimicking 0, 1, 2 and 4cm of fatty breast tissue with phantom-to-camera distance of 7cm. Imaging time is less than 2 min. 103
Figure 51. Vacuum deposition system utilized for a-Se deposition in Thunder Bay Regional Research Institute clean rooms facilities..... 109

List of abbreviations and symbols

a-Ge_xSe_{100-x}	amorphous germanium selenide
AFM	atomic-force microscopy
AMA	active matrix array
APBI	accelerated partial breast irradiation
As	arsenic
a-Se	amorphous selenium
a-Si	amorphous silicon
BCT	breast conserving therapy
CB	conduction band
CdTe	cadmium telluride
ChG	chalcogenide glass
Cl	chlorine
CS	corner sharing
CZT	cadmium zinc telluride
DFT	density fluctuation theory
DOS	density of states
DQE	detective quantum efficiency
E_B	energy barrier
E_C	conduction band edge
E_g	energy gap
EHP	electron-hole pair
E_V	valence band edge
ES	edge sharing

E_{SC}	energy of Compton scattered photons
ESR	electron spin resonance
ETH	ethylenelike
EXAFS	X-ray absorption fine structure
$E\gamma$	energy of incident gamma photons
FPXI	flat panel X-ray imagers
g-Se	glassy selenium
HARP	high-gain avalanche rushing photoconductor
^{125}I	iodine-125
IR	infrared
IP	intermediate phase
ITO	indium tin oxide
IVAP	intimately bonded valence alternation pairs
LP	lone pair
NaI	sodium iodide
NSPS	nanoscale phase separation
PAN	photo-induced anisotropy
PB	photobleaching
PbO	lead oxide
PBSI	permanent breast seed implantation
PC	photo-induced crystallization
^{103}Pd	palladium-103
PD	photodarkening
T_g	glass transition temperature
RSL	radioactive seed localization

RT	room temperature
^{99m}Tc	technetium-99m
TFT	thin film transistor
^{201}Tl	thallium-201
TOF	time-of-flight
T/T_0	relative changes in the transmittance
t-Se	trigonal selenium
VAP	valence alternation pair
VB	valence band
WBI	whole breast irradiation
WGSB	wire-guided surgical biopsy
XLV	X-ray light valve

CHAPTER 1

Introduction and thesis scope

1.1. Chalcogenide glasses and their applications

Chalcogenide glasses (ChGs) are glasses containing elements of the VI-A subgroup of the Periodic Table, namely sulphur, selenium and tellurium. GhGs hold a special place in the field of amorphous semiconductors, since they were the first non-crystalline solids, discovered to possess semiconductive properties in the mid-50s [1] and are extensively used today in a variety of fields including phase-change memories, sensors and photonics [2,3,4,5]. Like in any other disordered material, due to the lack of a long-range order or periodicity, *Bloch's theorem, which describes electrons and holes by wavefunctions extended in space with quantum states defined by the momentum* [6], cannot be applied to ChG. For this reason, for many years after the development of modern band theory for crystalline structures, amorphous solids were not considered of practical use as semiconductors; and even after the discovery of their semiconductive properties the concept of density of states and forbidden energy gap in amorphous matter remained puzzling. The majority of ChGs exhibit p-type conductivity (holes are typically more mobile compared with electrons), and they cannot be doped due to the pinning of the Fermi level. Furthermore, ChGs possess a unique characteristic - intrinsic metastability, which can result in reversible and irreversible transformation between amorphous and crystalline phases. Despite these challenging but unique properties, ChGs are widely used.

A prototype elemental ChG, amorphous selenium (a-Se), has been successfully utilized in number of commercial applications, ranging from xerography and xeroradiography in the 50s-70s, to the modern state-of-the-art flat panel X-ray images and ultrasensitive videotubes with high X-ray sensitivity and photoconductivity [5]. Other chalcogenide materials which exhibit reversible structural transformations, so-called phase-change materials, have been used in memory applications, as was first proposed by Ovshinsky in 60s [7]. In fact, ChGs are still applied today in CD/DVD-RW

discs [8,9]. Finally, ChGs are also appealing for utilization in infrared-transmitting optical fibers and as waveguides for telecommunications due to their high intrinsic transparently in the 2-25μm infrared region [9].

The central material of this thesis is amorphous selenium. It possesses unique photoconductive properties which has resulted in various successful applications over the past half century. The first major application of ChGs utilizing a-Se was xerography (from the Greek meaning "dry writing"). The first successful copier, Xerox 914, was introduced to the public in 1959 [10]. The idea behind xerography was that a cylindrical metalized drum coated with a-Se was first uniformly charged positive in the absence of light, and second exposed to light to form an electrostatic latent image. Third, the image was read out and the photoconductive layer cleaned and restored for the future use. Image read out involved image development utilizing toner, image transfer onto a suitable media with the help of an electric field and finally image fixture onto a substrate to make it permanent [11]. Later on, a similar principal was used in the first commercial xeroradiography system, the Xerox 125 Medical Imaging System, where a thicker layer of a-Se on the order of hundreds μm (compared to tens in xerography) was deposited onto oxidized aluminum plates and exposed to X-ray radiation to form the image of the body parts [5]. Soon the xeroradiographic technique was applied in numerous fields, such as mammography, arteriography, venography, and also for the imaging of bones and joints [12]. Although it provided high quality images, with edge enhancement [12], the image development with toner remained inconvenient and resulted in the search for alternative solutions. An alternative technique eliminating toner and enabling digitization was an array of electrometers reading out the latent image. It was employed in a selenium-based digital chest X-ray detector, ThoraVision by Philips Medical Imaging Systems [5,13], that was soon replaced by a new generation solid state detectors [14]. The real boom in a-Se imaging occurred in the late 90s, when the X-ray photoconductive layer was combined with new readout technology based on hydrogenated amorphous silicon thin film transistors (a-Si:H TFTs) forming, so-called active matrix arrays (AMAs) [15]. AMAs initially used in computer and domestic TV screens, were successfully utilized in digital x-ray detectors [14]. A detailed explanation of a-Se flat-panel AMA detectors will be presented in Chapter 6.

Several alternative a-Se based X-ray detector technologies have appeared on the market recently, one of them with a completely different readout method is called the X-ray Light Valve (XLV) [16]. XLV combines an a-Se layer, a thin liquid crystal layer and an optical scanner, which results in cost reduction while preserving high image quality [17,18]. Once X-rays are converted to electronic charges in an a-Se layer, the charge image is formed at the a-Se-glass interface. An electric field induced by charges twists the liquid crystal thin layer which is positioned on the other side of the glass. The liquid crystal reflects light proportional to the local twist. When the optical scanner is employed to illuminate the liquid crystals, the reflected light is captured by a pixelated photodetector and digitized.

Another distinct property of a-Se that has allowed its commercialization in optical imaging is impact ionization or avalanche multiplication. Impact ionization was first reported by Juska and Arlauskas in 1980 [19] and was demonstrated using metal/insulator/a-Se/insulator/metal structures at an electric field higher than 80V/μm. The collected number of holes per absorbed light photon was greater than one, and this number can be increased by increasing the applied electric field further (*n.b*. electrons do not undergo avalanche multiplication in a-Se). Following this discovery in the late 1980s high- gain avalanche rushing photoconductors (HARP) were developed in Japan and utilized in ultrasensitive vidicons, which are still used today. Due to the high photoconductive gain, HARP cameras are capable of producing high quality images at extremely low levels of light, e.g. filming at night, underwater, etc. Recently, there have been studies indicating that avalanche multiplication phenomenon in a-Se may be employed in low-dose radiation medical imaging detectors. It is proposed to replace vacuum photomultipliers or silicon photodiodes in indirect type X-ray detectors. In such devices, light emitted as the result of X-ray interaction with a scintillator will be captured and converted to an electrical signal by an a-Se avalanche photodetector. This would dramatically increase detector performance at low doses [20].

Finally, the potential of a-Se as a photoconductor can be extended to low-energy gamma-ray imaging, which will be proposed under the scope of this thesis in Chapter 6.

1.2. Significance of photo-induced metastability for practical use of ChGs

Despite of the number successful applications of ChGs, the major challenge is its fundamental metastability. There is always a tendency for conversion of the amorphous form to the thermodynamically more stable, crystalline phase of the material. Furthermore, because the structure of amorphous semiconductors is not thermodynamically stable, the transformation can be triggered by optical/X-ray excitation, thermal heating or applied electric field [21]. Each case has its own peculiarities and thus to ensure effective application of a given ChG, a solid understanding of the causes for structural transformations on the microscopic level has to be developed.

This PhD thesis is devoted to the study of photo-induced metastability of the most widely used ChG – amorphous selenium (a-Se), and the archetypal a-Ge_xSe_{100-x} glass compounds. Although photo-induced metastability is generally linked to the promotion of photo-induced defects in the material structure, the underlying physics is not clear to date. There have been several approaches to combat the most undesirable photo-induced metastability effect in ChG-based sensors – photocrystallization. For example, in amorphous selenium based HARP cameras it is suppressed by keeping the structure at 35^0C [22]. The a-Se structure used in flat panel X-ray detectors is stabilized by doping pure a-Se with 0.2-0.5% of arsenic (As) and 10-30ppm of chlorine (Cl), which prevents material crystallization on the timescale of years [5]. Doping also partially balances the inherent defects, called valance alternation pairs (VAPs) [23] which, if left non-compensated, control deep trapping times and consequently degrade imaging performance by introducing "lag" and "ghost" effects [24]. Even in stabilized a-Se, photoexcitation is shown to enhance the concentration of the VAP defects [25] which may lead to deterioration of the photoconductor. Continued research into defect creation and defect relaxation processes and the link to photo-induced metastability in a-Se and its alloys is important to prevent adverse effects on the material stability and consequently on the performance of ChGs based devises.

This thesis is focuses on the relevant processes for ChG photosensors: we study pathways from the micro-level, i.e. defect creation and relaxation, to macro-level photo-

induced effects, namely photodarkening (PD), photobleaching (PB) and photo-induced crystallization (PC). This is done for two materials, a-Se and a-Ge_xSe_{100-x}, where these effects are most important for applications in sensing. We show the effects of temperature and the energy of excitation on PD kinetics in a-Se, and define the root cause for transient and metastable optical transmittance changes. A variety of effects in a-Ge_xSe_{100-x} are investigated as a function of composition across the glass forming region; and the mechanisms triggering transient and/or metastable PD and PB effects are revealed. In addition, we demonstrate that metastable photodarkening acts as a precursor for photo-induced crystallization, which confirms previous findings [122]. We also investigate the effects of substrate and temperature on photo-induced crystallization in a-Se and demonstrate that onset of PC is enhanced by the rigidity of the film-substrate interface.

Finally, our investigation of the physics of a-Se and the understanding of its properties has allowed us to extend the range of a-Se to a new type of device, namely a specialized direct conversion gamma-camera for low energy applications. With a laboratory prototype based on an a-Se flat panel X-ray detector outfitted with specially designed collimator, we demonstrate the potential of the proposed device to fulfill the clinical requirements for image-guidance of radioactive seed procedures.

1.3. Thesis scope

Chapter 2 introduces basic properties of a-Se and a-Ge_xSe_{100-x}, i.e. atomic structure, density of states, defect classification, and characteristic Raman modes. An overview of light-induced effects is presented; in particular photodarkening and photo-induced crystallization in a-Se, and photodarkening and photobleaching in a-Ge_xSe_{100-x}. The major motivation for understanding the origin of these effects and associated photo-induced metastability concludes the chapter.

Chapter 3 develops a methodology for investigation of the light-induced phenomena. For the PD/PB effects study, an experimental two-laser beam technique and Raman spectroscopy used in conjunction with theoretical modeling are outlined. For the photo-induced crystallization, co-localized Raman mapping and atomic-force microscopy (AFM), as well as temperature-dependent Raman spectroscopy techniques are described.

In Chapter 4 & 5 the major results on light-induced effects for both a-Se and a-Ge_xSe_{100-x} glasses are presented and discussed.

Chapter 6 is devoted to the a-Se based gamma-camera that is proposed to facilitate image guidance for a novel, alternative breast cancer treatment options, i.e. Permanent Breast Seed Implantation and Radio Seed Localization procedures. The constructed fluence integrating gamma camera prototype is described and results of its imaging performance evaluation in realistic breast phantom studies are demonstrated.

Concluding remarks summarize the thesis.

CHAPTER 2

Properties of a-Se and its compounds

2.1. Basic properties of a-Se

2.1.1. a-Se atomic structure

Selenium is a group VI element in the periodic table. Its electron configuration is $[Ar]3d^{10}4s^24p^4$, hence it has 6 valence electrons in the outer shell. In the "ideal" a-Se network every atom is covalently bonded with two nearest neighbors. Each of the Se atoms has two paired electrons deep in the valence band (VB) in the *s*-state, which do not participate in bonding. The two singly occupied *p*-states participate in the covalent bond formation, splitting into bonding (σ) and anti-bonding (σ^*) molecular orbitals (Figure 1).

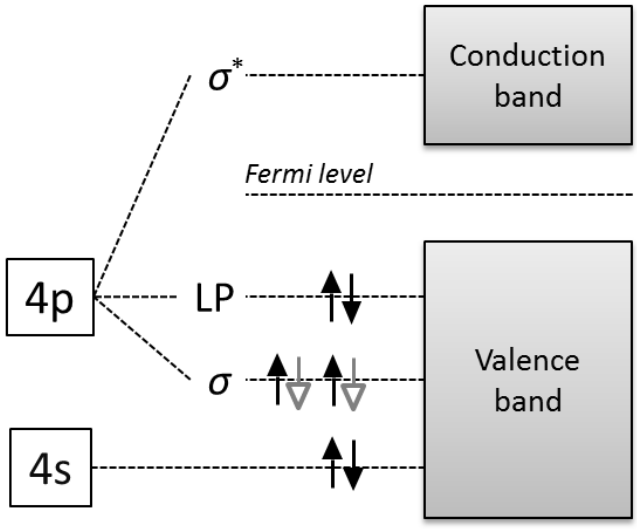

Figure 1. Schematic representation of Se atom bonding configuration, in case of two covalent bond formation with another Se atom (arrows is grey correspond to electrons of the other Se atom).

The remaining p-state is filled with two paired electrons, the so-called *lone pair* (LP), electrons which form the top of the VB, as shown in Figure 1. The LP electrons play an

important role in a-Se, to some extent defining the physical properties of the material as will be discussed later in this Chapter.

Selenium exists in various forms, including crystalline (e.g. trigonal or hexagonal, α-, β- , γ-monoclinic) and amorphous allotropes (e.g. red, brown, black Se) [26]. Whereas the structure of crystalline Se is well defined in the literature [27], the structure of a-Se is not. Like for any other amorphous material, the features of the atomic structure of a-Se are: short range order, long range disorder and coordination defects, thus over- or under-coordinated atoms may be incorporated in a random network [28]. It is important to note that crystalline and amorphous forms of the same material share similar local order, i.e. the average number of nearest neighbors, average bond length and average bond angles. For this reason, for many years the molecular structure of a-Se was represented as a mixture of fragments of the two main forms of crystalline Se, i.e. monoclinic Se_8 rings and trigonal Se_n polymer chains.

Hexagonal or trigonal selenium (t-Se) is thermodynamically the most stable allotrope of crystalline Se, in which the crystal is composed of parallel helical chains, Se_n, with the repeated unit of three atoms (Figure 2, left part). In this fashion, a lattice of

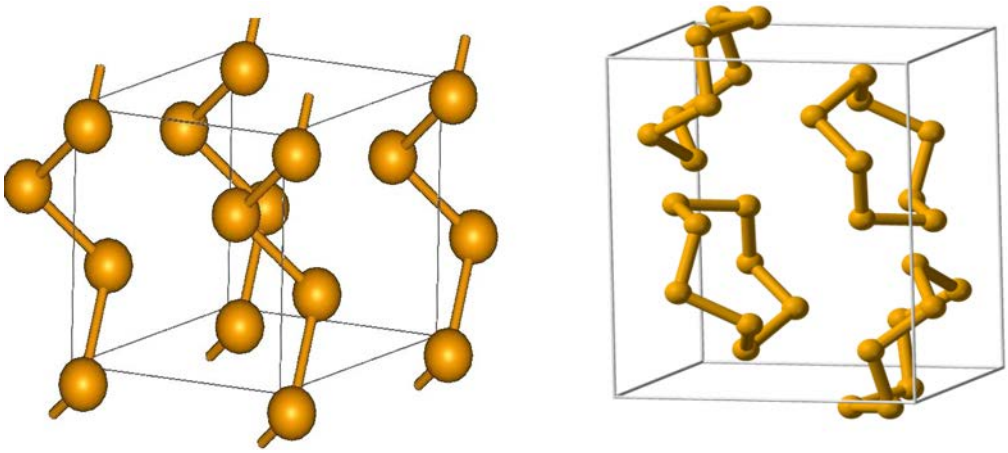

Figure 2. Left: trigonal or hexagonal Se [29]; Right: monoclinic α-Se [30].

trigonal symmetry is formed and every atom has two intrachain covalent bonds with nearest neighbors. The interchain interactions are found to be of two types, weak van der Waals type interactions between chains [31] and strong covalent due to the partial

overlap of the LP and antibonding orbitals of neighboring Se atoms [32]. Monoclinic Se_8 has three forms α, β and γ (α-Se is presented in Figure 2, right part) constructed of eight-member rings. Whereas the unit cell of α- and β- Se is composed of four Se_8 molecules, γ-Se contains eight Se_8 molecules [32]. Another form of crystalline Se which is composed of Se_6 ring-like molecules is called rhombohedral selenium [33]. To have an idea of how the parameters of the crystalline structures differ from one to another, examples are provided. The Bond length and bond angles in the case of α-Se and β-Se are almost identical 2.32 and 2.34 Å and comparable to the 2.37Å for t-Se. The melting temperatures are reported to be 144^{o}C, 100^{o}C for α- and β- monoclinic Se respectively, which is much lower than 217^{o}C for t-Se. Once the temperature reaches 140-160^{o}C the monoclinic form spontaneously transforms to the more stable t-Se. Overall, the crystalline forms of Se are formed in a way that minimizes interatomic interactions of the LP electrons [25].

Amorphous selenium is typically two-fold coordinated with the purely covalent atomic bonds. The molecular structure of amorphous selenium, as mentioned earlier, was believed to be a mixture of ring-like and chain-like structures with no definite ratio, but predominantly Se_n chains. Rings can be composed of 6 or 8 atoms [34]. Different techniques were used in 60s and 70s to probe and explain the a-Se molecular composition [35,36,37,38]. Today, the most widely accepted model of a-Se structure is the *random chain model* originally suggested by Lucovsky [34,39] and depicted in Figure 3. The model states that because the bond length, bond angles and magnitude of the dihedral angle (angle between two neighboring bonding planes) are approximately the same in both Se rings and Se polymer chains, the only difference between them is the sign of the dihedral angle, alternation of which determines cis- or trans- coupling configurations (Figure 4). In such a way, trans- coupling configuration allows for infinite extent of polymer chains, whereas cis-configuration leads to a linkage of "chain" onto itself causing the formation of ring fragments [39]. As the result the local order of a-Se depends on the sequence of dihedral angles.

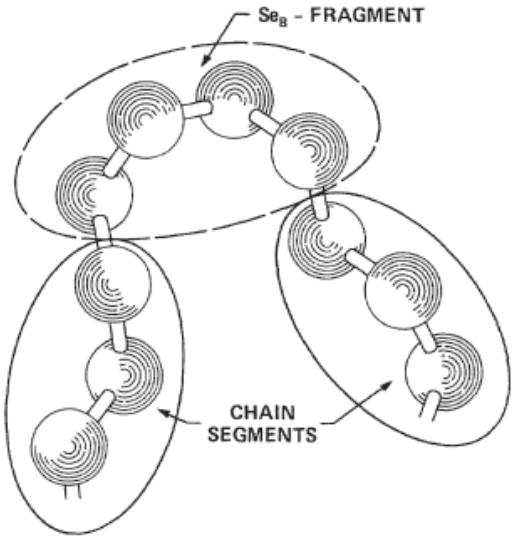

Figure 3.Schematic representation of a-Se local molecular order, where chain-like segments are characterized by same phase of dihedral angle and ring-like fragments by the alternating one [34].

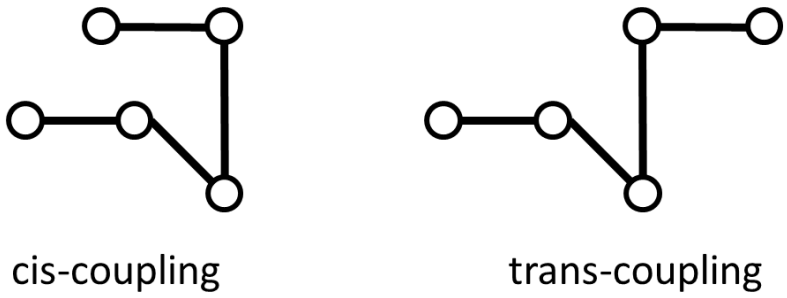

Figure 4. Cis- and trans- coupling configurations for molecular bonding in Se, re-drawn from Ref. [39].

To the best of our knowledge, the generalized *random chain model* is still in favor today supported and enriched by a number of recent publications [21,25,34]. The prevalence of trans-coupling or chain-like structures compared to ring-like Se_8 fragments was recently reported to be 90%-to-10% in a-Se, based on high-resolution off-resonant Raman scattering [32]. Another study explained the energetically favorable chain formation by calculating an energy gain of about -0.025eV per atom when a ring-like structure is transformed to a chain-like one [25]; and also it highlighted the special role of LP electrons in a-Se structure. By first-principles simulation it was demonstrated that the

bond angle and torsion angle in a-Se is essentially defined by a LP electron interaction which pushes the shared orbitals apart. Indeed, in Selenium the interchain distance is close to the intrachain second-nearest distance [40]. In contrast to t-Se, which minimizes the interatomic interactions of LP electrons, in a-Se, LPs are disoriented, resulting in tension along the chains. Thus, tension release via crystalline-like inclusions in a-Se structure is favourable [25]. An example of a simulated "ideal" structure with two adjacent chains is shown in Figure 5, where a combination of polymer-like and ring-like segments reduces the repulsion between LP orbitals.

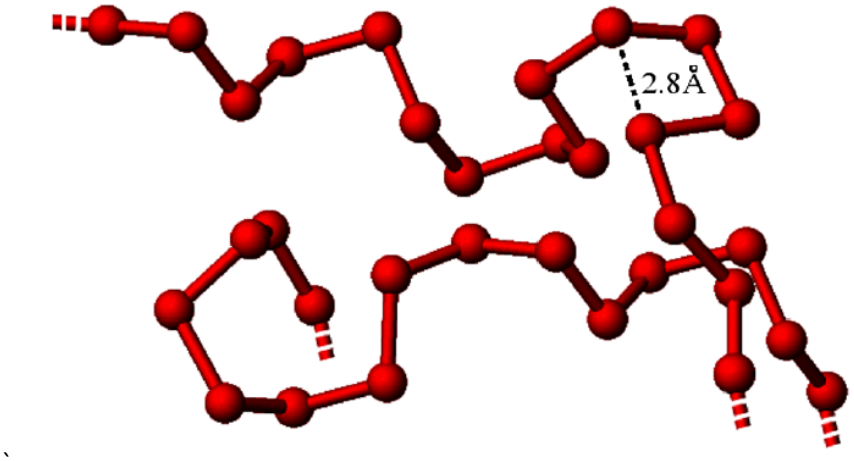

Figure 5. Two adjacent chains of a simulated a-Se structure [25].

In addition, linked rings can minimize the tension along the chains. When the tails of opened ring-like segments close enough to overlap, large repulsion takes place and the formation of closed rings can decrease the total energy by -0.49eV [25]. The average bond length of 2.37 Å for two-fold coordinated Se atoms is reported in the literature [41]. The interatomic distance between the atoms that are not involved in covalent bond formation is reported to vary over a wide range with a lower limit of 2.80 Å (Figure 5). It should be noted that if the average bond length is enlarged to 2.80 Å, some atoms can be considered as three-fold coordinated. Indeed, over-coordinated atoms in valence alternation pairs (VAPs) are well-known structural defects in ChGs and a-Se in particular [42,43,44]. Whereas the entire subchapter 2.1.4 is dedicated to the discussion of defects and VAPs in a-Se, it is important to emphasize that coordination defects also help to

release tension due to the destabilizing interactions of LP orbitals [25]. This explains why in a well-relaxed a-Se structure over- and under- coordinated atoms are found.

2.1.2. Raman spectra of a-Se

Raman scattering is the most frequently used spectroscopic method to probe the symmetry of molecular structures, bonding and the degree of disorder in solids in a non-destructive manner. From a quantum mechanical point of view, Raman scattering is the inelastic scattering of incident optical photons by phonons (lattice vibrations) within the material. When incident light (usually a monochromatic source with photon energies in the range 2-4eV) passes through the material, the spectra of the scattered light consists of several distinct features. The central, strongest signal is at the same frequency as the irradiation source ω_0, and occurs due to the elastic scattering (Rayleigh scattering) of the incident photons. Other spectral lines that are symmetrically spread on both sides of the central line with frequencies $\omega_i = \omega_0 \pm \frac{\Delta E}{\hbar}$ are due to the Raman scattering. The frequency shift to the left or to the right of the spectra depends on whether photon gave up a portion of energy, ΔE, or gained it as the result of interaction with molecules of the probed matter. Raman bands with frequencies lower than that of incident light are called Stokes and higher ones are called anti-Stokes. When energy is transferred from incident photons to the material, it results in the Stokes lines or the redshift of scattered photons. When the energy is transferred from the material to the incident photons anti-Stokes spectral lines appear and a blue shift is observed. In typical Raman spectra the intensity of the scattered light is plotted vs. frequency difference of the incident and scattered photons. It is important to use low enough intensity of incident light not to cause overheating of the material, since the thermal excitation itself will result in different Stokes and anti-Stokes spectral line behavior. When the frequency of excitation does not correspond to the interband transition of the solid, the Raman effect is a second order virtual process. As such, photoexcitation brings the system to a virtual electronic state and during subsequent relaxation, the emitted photon can be shifted up in the spectra due to phonon absorption, or shifted down by phonon emission forming lines in the Raman emission spectra. The intensity of the lines is greatly enhanced when the frequency of

excitation is comparable to the interband transition frequency (this is called resonant enhancement). With increasing disorder of the material discrete spectral lines eventually form a broad spectrum. For structural analysis the Stokes-side of the Raman spectra is analyzed since it represents the equilibrium state of the material. The anti-Stokes part becomes more and more pronounced as atoms and molecules are excited, e.g. by heating. For this reason measurement of the Raman Stokes-to-anti-Stokes ratio is frequently performed to ensure that no significant heating takes place as Raman spectra is being recorded. The peak frequency of the Raman spectra is obtained by spectra deconvolution (frequently with Lorentzian or Gaussian shapes to distinguish the modes).

Figure 6 shows the Raman spectra of a-Se in comparison with t-Se.

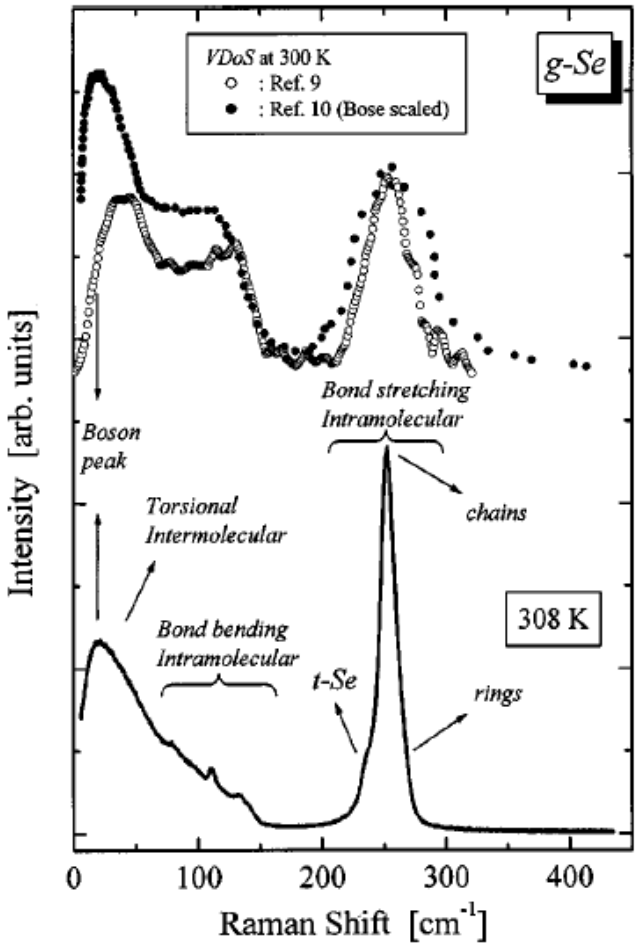

Figure 6.Typical Raman spectra featuring main vibrational modes of amorphous or glassy Se (g-Se) (lower part) with corresponding vibrational density of states (VDoS) (upper part) [32].

The amorphous selenium Raman spectra can be divided into three regions: low-frequency region up to ~70cm^{-1}; intermediate region from ~70cm^{-1} to 150cm^{-1} and the main high-frequency region from ~200cm^{-1} to 300cm^{-1}. The main vibrational mode in a-Se spectra is characterized by a broad band around 250 cm^{-1} related to Se-Se bond stretching vibrations with A1-symmetry, for both chain-like and ring-like structures [45]. The peak broadening in the range from ~240cm^{-1} to ~260cm^{-1} is due to the high level of disorder. When crystalline inclusions are present in a-Se structures the sharp low-frequency peaks around 233cm^{-1} and 237cm^{-1} (usually unresolved) corresponding to t-Se are apparent in the spectra [46]. Weaker lower-frequency Raman peaks in the region 70-150cm^{-1}, at 82, 112, 138cm^{-1} are attributed to the Se_8 bond-bending vibrations of ring-like fragments [47,32], but due to their low intensity are often less analyzed in studies [46]. Finally, the lowest energy region, up to 70cm^{-1} is dominated by the asymmetrical, so-called Boson peak which is due to torsional intermolecular vibrations [32]. The Raman spectra of a-Se, with main vibrational frequencies around 250 cm^{-1} and lower intensity peak at 113 cm^{-1} supports the validity of the *random chain model*, where cis-coupling permits both bond-stretching and bond-bending motions at the corresponding frequencies, whilst trans-coupling representing polymer fragments with only bond-stretching modes possible. In other words, the vibration of all atoms contributes to the peak around 250 cm^{-1} peak, but only vibrations from cis-configuration with alternating dihedral angle appear as a peak at 113 cm^{-1} (Figure 7).

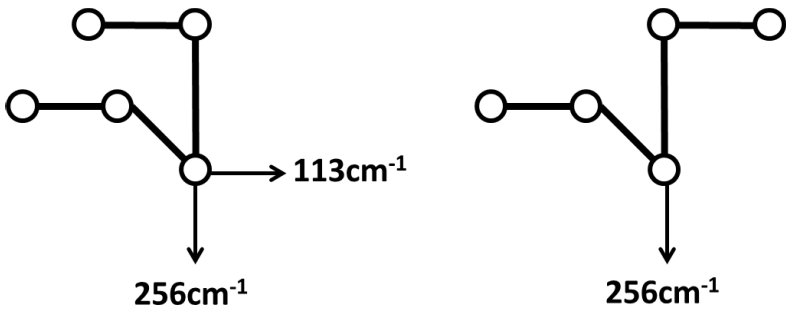

Figure 7. Cis- and trans- coupling configurations for molecular bonding in Se with corresponding frequencies of atomic displacement [39]

Due to its high sensitivity in probing bonding configurations, Raman scattering measurements are instrumental in studies of photo-induced structural transformations in

a-Se. Indeed, previously it was possible to monitor the kinetics of the photo-induced crystallization (Figure 8), as the growth of trigonal selenium was observed under a 17 W/cm^2 or 10 W/cm^2 633nm light flux over the course of 7 hours [46].

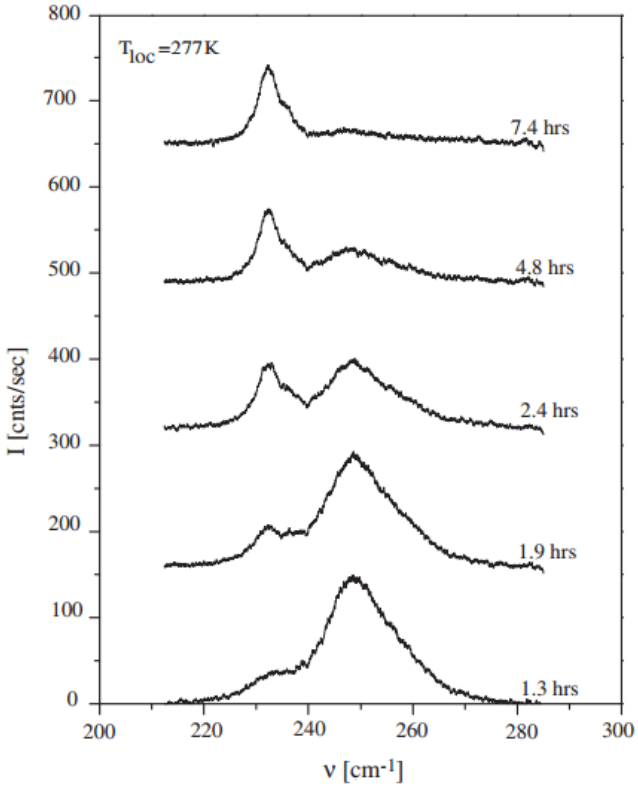

Figure 8. Raman spectra obtained in a-Se under illumination for various exposure times, from 1.3hrs to 7.4hrs [46].

As can be clearly seen from Figure 8, a crystalline Se band (233cm^{-1}, 237cm^{-1}) is becoming more and more pronounced while the a-Se band weakens (250cm^{1}) as the continuous illumination time increases. This reflects structural transformation from amorphous to crystalline phase of Se, and full crystallization is reached in about 7.4hrs of continuous light illumination at 277K. The effect of temperature on the onset time of photo-crystallization is discussed later in this Chapter.

2.1.3. Density of states and role of the disorder

In amorphous semiconductors, because of the loss of momentum conservation in electronic transitions, the energy-momentum band structure of a crystalline semiconductor is replaced by an energy-dependent density of states distribution. Since, short range order is preserved, the band gap energy of amorphous phase remains similar to the crystalline phase. Due to medium and long range disorder which originates from bond angles and bond length deviation, sharp band edges inherent to crystalline semiconductors are replaced by broad tails of states (of limited depth) extending into the forbidden gap (Figure 9). States within the tales are localized. The separation between the extended and localized states is called the mobility edge [6]. The energy gap between mobility edges is called the mobility gap (Figure 9). It is an analog of the forbidden gap in crystalline solids. Overall, there are three main energy ranges: valence band (VB), conduction band (CB), band tail region and defect states in the mobility gap.

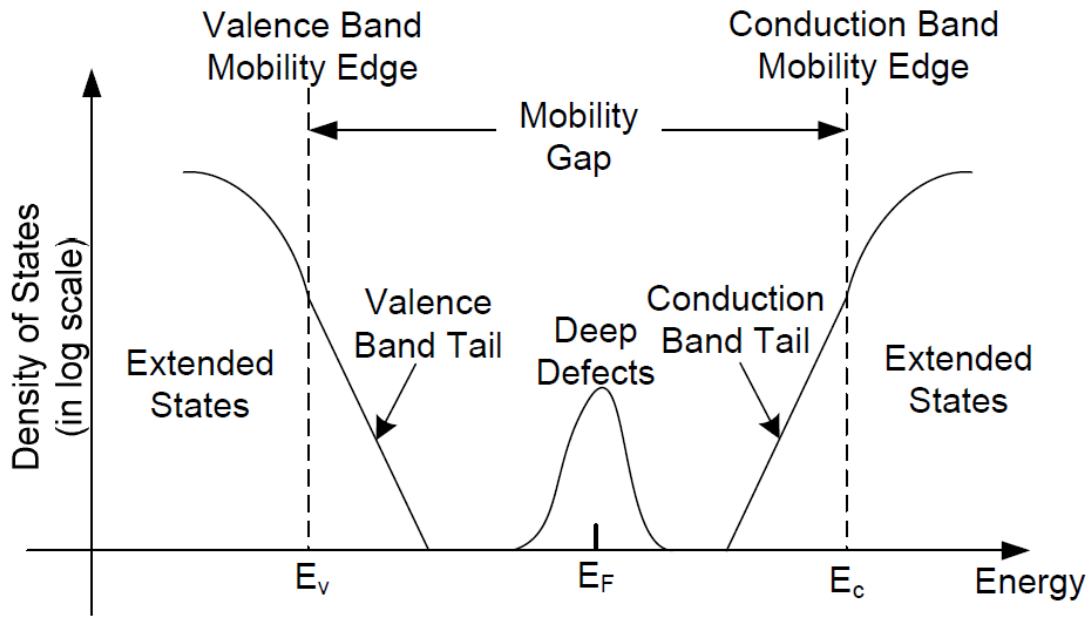

Figure 9. Schematic density of states (DOS) distribution in amorphous semiconductors.

First proposed by Mott and Davis in 1979 [6], the mobility edge, Ec, derived its name from the fact that at zero temperature, the mobility of electrons is 0 below it and

has a non-zero value above it (T=0 electrons are mobile only above Ec and contribute to conduction). In other words, at zero temperature carriers conduct in extended states but do not conduct in localized states. The degree of disorder which is reflected in the "tailing" of the band edges influences not only the mobility edge energy but also the mobility of electrons and holes. For example, for trap controlled transport, called multiple trapping, the conduction of the charge carriers is characterized by frequent trapping in shallow localized states followed by excitation to extended states. The effective carrier mobility, called drift mobility, is lower than actual mobility in extended states and for the majority of disordered semiconductors is temperature dependent due to the thermal activation. The drift mobility is also time dependent in the majority of amorphous semiconductors which causes dispersive transport (consequence of trap release time distribution from the band tails) [6]. Another critical feature of the DOS in amorphous semiconductors is deep electronic states within the mobility gap due to the coordination defects. These effect trapping times and recombination rates in amorphous semiconductors.

The similarity of covalent bonds in crystalline and amorphous Se leads to its similar electronic structure and comparable bandgaps. Amorphous selenium DOS has distinct peculiarities compared with crystalline Se. One of them is the formation of broad band tails due to lone pair electron interactions and disorientation. From the 1960s to the 1990s a number of time-of-flight (TOF) and xerographic measurements were performed [48,49,50] allowing researchers to attain a good understanding of the electronic properties of a-Se. The most influential early work by Abkowitz [51] revealed the DOS for doped and undoped a-Se shown in Figure 10 that was later confirmed by others [52,53]. The DOS diagram defines a mobility gap of 2.22eV as well as the additional features of the mobility edges. The shallow traps for electrons and holes were reported to lie at 0.35eV and 0.26eV below the CB and above the VB respectively. Deep electron states had a broad distribution with mean energy of 1.22eV from the CB mobility edge and deep hole states at 0.87eV from the VB mobility edge. The Fermi level was determined to be pinned 0.045eV below the middle of the mobility gap. However, since Abkowitz's publication other distinct peaks have been reported [54,55].

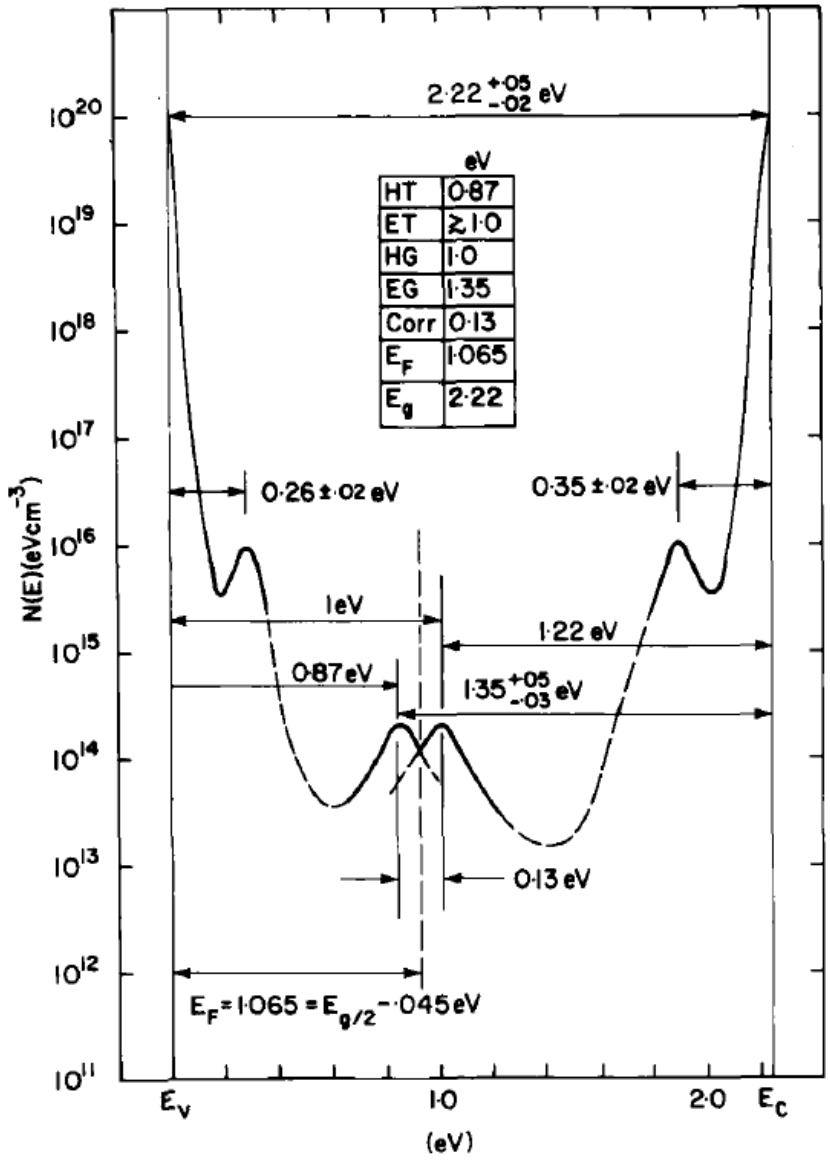

Figure 10. a-Se DOS by M. Abkowitz (1988) [51].

Recently, S. Kasap and co-workers [56] clarified the DOS distribution by means of TOF measurements performed in a wide range of electric fields, temperatures and sample thicknesses. Amorphous selenuim DOS by Kasap et al. is shown in Figure 11.

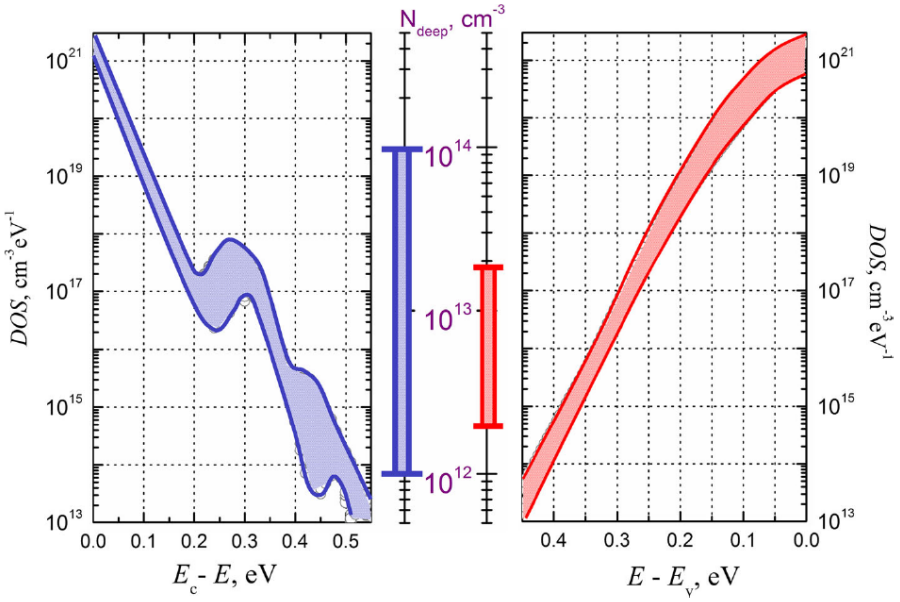

Figure 11. Generalized DOS for pure and stabilized a-Se (stabilization refers to alloying with ≈0.5% of As and doping with Cl in ppm range). The central part indicates the total concentrations of deep traps for electrons and holes whose energy distributions were not resolved due to the limitations of applied methods [56].

Instead of the Gaussian peak at 0.35eV below the conduction band reported by Abkowitz, they proposed two Gaussian-like peaks below conduction band at 0.27-0.33eV and 0.38-0.48eV. These authors also found an exponential-like tail spreading above the E_v down to E_c-0.20eV (Figure 11) in complete agreement with Abkowitz model. In all models, the nature of DOS peaks below E_C was attributed to the structural defects in the forbidden gap, namely valence alternation pairs.

2.1.4. Defect classification in a-Se

The defect classification of non-crystalline solids differs from that of crystalline ones. In crystalline materials any deviation from ideal network is considered as a defect. Commonly, there are three types of defects: point defects (vacancies and interstitials); extended defects (e.g. grain boundaries and dislocations) and chemical impurities (substitutional atoms or molecules) [57]. The primary defect in amorphous semiconductors is a bonding or a coordination defect. An important coordination defect is

a single unsatisfied bond incorporated into the network and is called *dangling bond* defect. Dangling bonds are known to drastically deteriorate the electronic properties (e.g. a-Si has poor photoconductivity and cannot be doped until its dangling bonds are passivated by hydrogen atoms creating hydrogenated amorphous silicon [58]). Another type of coordination defect is an over-coordinated atom or hypervalent defect. Lone pair amorphous semiconductors with non-bonding orbitals can possess specific bonding configurations, as e.g. described below in case of a-Se.

In selenium, due to its low-coordination (normally two-fold), the types of coordination defects are limited to: under-coordinated one-fold and over-coordinated three-fold or four-fold Se atoms. Whereas one-fold and three-fold coordination Se defects are commonly present in the bulk and on the surface, the four-fold coordinated Se atom is found to be a surface defect. The most studied defect in a-Se is a pair of charged under- and over- coordinated defects, the so-called valence alternation pair (VAP). It represents a case where two selenium atoms in close proximity are found as a combination of a positively charged three-fold coordinated and a negatively charged one-fold coordinated Se atom. The first research into VAP defects arose from the controversy around the pinned Fermi level in ChGs and absence of a signal in electron spin resonance (ESR) experiments [59,60]. Fermi Level pinning in non-crystalline chalcogenides is due to the superposition of band tail states extended in the mobility gap. Anderson [61] was first to suggest that due to the strong electron-lattice interaction all spins are paired which results in absence of ESR signal. Indeed, the energy difference between a center with paired spins and that with unpaired spins is due to the Coulomb repulsion between two electrons, the exchange interaction of the two electrons and the bond distortion caused by the additional electrons. This difference is called the correlation energy. In a-Se it turns negative and the center with paired spins is called a negative-U center. The proposed existence of the negative effective correlation energy in a-Se pointed to the instability of the neutral paramagnetic dangling-bond defect against the formation of VAP. Mott [62] proposed the exothermic reaction of defect states which resulted in the absence of unpaired spins, i.e. $2D^0 \rightarrow D^+ + D^-$, where D stands for dangling bond in three states, neutral, positively and negatively charged respectively. At the same time a VAP model

was developed based on carrier transport, luminescence, photo-induced ESR and other experimental data by several scientists, including Mott and Street [63], Kastner, Adler and Fritzsche [64] and Anderson [65]. They described VAP defect formation using Eq. 1

$$C_2^0 = C_1^- + C_3^+, \quad (1)$$

where *C* represents a given atom, subscript indicates its coordination number and superscript its charge state, i.e. neutral, positive or negative. It is appropriate to describe the process of VAP creation in a-Se. When 2 normally-bonded Se atoms are transformed into a defect pair (three-fold over-coordinated and one-fold under-coordinated Se atoms) one electron is transferred to one-fold site to optimize the energy configuration. It has been shown that VAP defect production is energetically more favorable than any other defect configuration, e.g. dangling bond production or neutral over- and under-coordinated atoms [64]. Figure 12 summarizes major bonding possibilities in ChG atoms with corresponding energetic positions, taking the energy of the LP orbital to be zero. When C_1^- and C_3^+ are in close proximity the intimate valence alternation pair (IVAP) is formed. Moreover, the presence of VAP and IVAP do not change the total number of bonds and the energy of formation is small enough to give rise to a high density of VAP in ChGs [64].

Today VAP is considered to be a fundamental defect in non-crystalline chalcogenides. VAPs present in a significant quantity in well-relaxed structures (VAP defect density is about 10^{17} $cm^{-3}eV^{-1}$ in a-Se [57]), and is known to reduce the potential energy of the system due to a thermodynamically favorable formation. Similar to crystalline-like inclusions, VAPs help to resolve destabilizing interactions of LP orbitals along the Se chains.

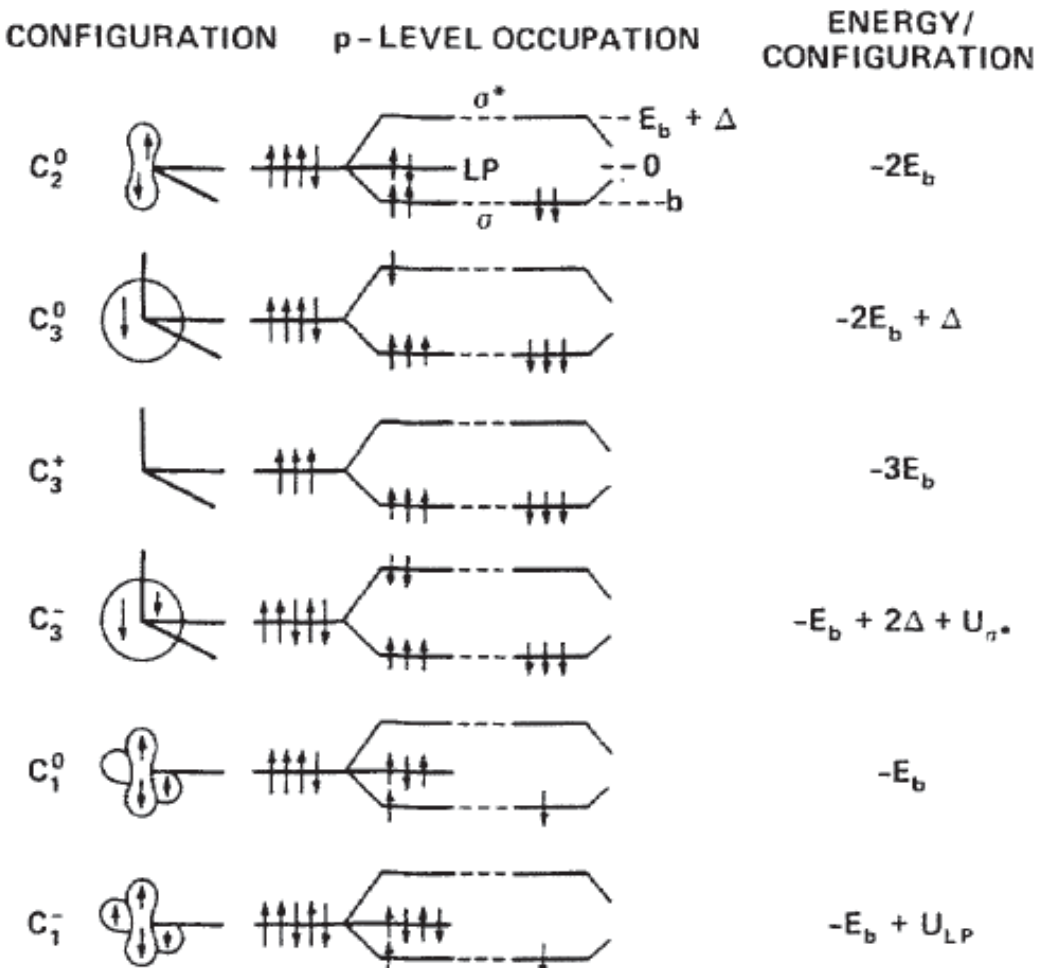

Figure 12. Electronic configurations for possible bonding types in lone-pair semiconductors with corresponding energetic positions. On the left: straight lines correspond to σ orbitals, lobes to LP orbitals and circles to anti-bonding orbitals. On the right: $\boldsymbol{E_b}$ is the bonding energy, Δ destabilization energy due to bonding/antibonding states splitting, $\boldsymbol{U_{\sigma^*}}$ and $\boldsymbol{U_{LP}}$ increase in energy when electron is placed on σ^* or LP orbital due to electronic correlation [64].

VAP defects are reported to have different configurations and consequently can be classified into three different types with corresponding energy levels in the mobility gap (Figure 13, [56]). The following description of VAP defect types is rewritten from our recently published paper (Ref. 25).

The first type (Figure 13(a)) represents VAP in which C_1^- and C_3^+ atoms belong to different chains and the energetic position of the C_3^+ is correlated with a DOS peak 0.27-

0.33eV below the CB (Figure 11). This defect can appear as the result of chain discontinuation. When a-Se chain breaks, one of the C_1^0 sites remains separated, while another connects to a two-fold C_2^0 site of another chain, thus, becoming a three-fold C_3^0coordinated. This process is followed by a charge exchange reaction $C_3^0 + C_1^0 \rightarrow C_3^+ + C_1^-$ and formation of a *two-chain* VAP defect. The total energy in this case is reported to be lowered by -1.22eV compared to an ideal (two-fold) configuration. Thus, it confirms the efficiency of relieving tension with VAP defect formation, despite the strong dipole formed between the C_1^- and C_3^+ sites. In addition, the C_1^- and C_3^+ sites are separated by 3.15 Å and the C_3^+ bond is lengthened to 2.4–2.6 Å for this VAP defect [25].

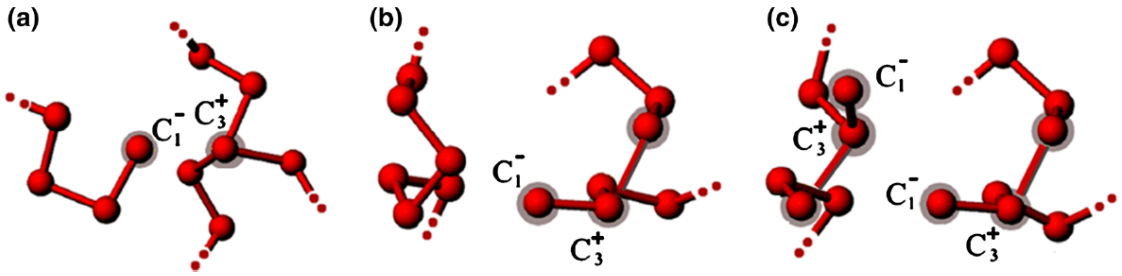

Figure 13. Different types of VAP defects: (a) two-chain VAP; (b) IVAP and (c) IVAP pair [56].

The second and third VAP types are based on the concept of intimately bonded valence alternation pairs (IVAPs), when C_1^- and C_3^+ Se atoms belong to the same chain and Coulomb and exchange forces act between IVAP partners. Whereas the second type (Figure 13 (b)) represents a single IVAP with the C_3^+ state 0.45eV below E_C , the third type (Figure 13 (c)) is a combination of two IVAPs from different chains and is found to be the most effective in tension relief [25]. The IVAPs combination occupies the deepest localized state at 0.61eV below E_C. In general, IVAP defects appear on a single chain of an ideal network and do not affect the electronic and structural configurations of the other chains. The mechanism of IVAP formation is the same as for the VAP: one broken end remains detached while a second attempts to convert into a threefold site denoted in Figure 13(b) as the C_3^+ site. Because the induced charge redistribution is restricted to a single chain, the strong dipole keeps apart the C_3^+ and C_1^- sites at a distance of 2.82Å, i.e.,

the third bond associated with the C_3^+ is elongated. Moreover, the strong dipole moment masks the stress-relieving effect and as a result, no decrease in energy is detected with the formation of this defect. However, when two IVAP defects appear in a pair (see Figure 13(c) showing two IVAP defects separated by a distance of approximately 3.8Å [25]), the interaction between the defects reduces the total dipole moment. The bond shortens to 2.78Å, and the total energy decreases by −0.04eV per atom uncovering a stress-relieving effect. As a result, the IVAP pair is more stable than the single IVAP defect (the total energy difference is −1.08eV), and IVAP defects are expected to appear predominantly in pairs. It should be noted that the structural rearrangements of IVAP pair formation are restricted to the two involved chains and do not affect the rest of the network. The IVAP combination is believed to be responsible for deep trapping in a-Se with slow (on the order of hours, sometimes days) thermal excitation mechanisms.

In surface layers of amorphous selenium pairs of four-fold and three-fold hypervalent coordination defects were recently reported by T. Scopigno et al. [43]. Surface atoms are no longer in equilibrium conditions due to the absence of nearest neighbours, consequently anisotropic fields of interatomic forces are exerted on them. This may result in normal relaxation with normal coordination or bond rearrangements if the normal coordination cannot be preserved. The surface of a-Se was shown to have increased stiffness due to the different topology compared with the bulk structure. Notably, hypervalent four-fold and three-fold coordination defects incorporated into an a-Se surface network serve as strain release not only in the top-most layer, but within a few nanometers. Considering negligibility of surface-to-bulk ratio for the studies carried out in the aim of this thesis, surface defects are beyond the scope of this work.

2.2. Basic properties of Ge-Se glasses

Germanium selenides (a-Ge_xSe_{100-x}) are the archetypal covalently bonded binary class of glasses with the unique feature of a transition from flexible to stress-rigid phases as the Ge content rises from 5% to 30% and above [66]. The interest in its physical properties, and light-induced effects in particular, is not only fundamental from the glass science

point of view [67,68,69] but also due to the potential they hold for applications in optics and optoelectronics [70,71,72].

2.2.1. Ge-Se bonding configurations

Germanium is a group IV element in the periodic table. Its electron configuration is $[Ar]3d^{10}4s^24p^2$, hence it has 4 valence electrons in the outer shell, consequently Ge atom has a tendency to form four bonds with its nearest neighbors. Over the past two decades a wide range of spectroscopic studies reveal the dominant character of the four-fold Ge atoms and the two-fold Se atoms in the Ge-Se glass forming system [73,74,75,76,77,78]. This is due to covalent heteropolar Ge-Se bond formation, usually in the form of $GeSe_4$ *tetrahedra* units (Figure 14).

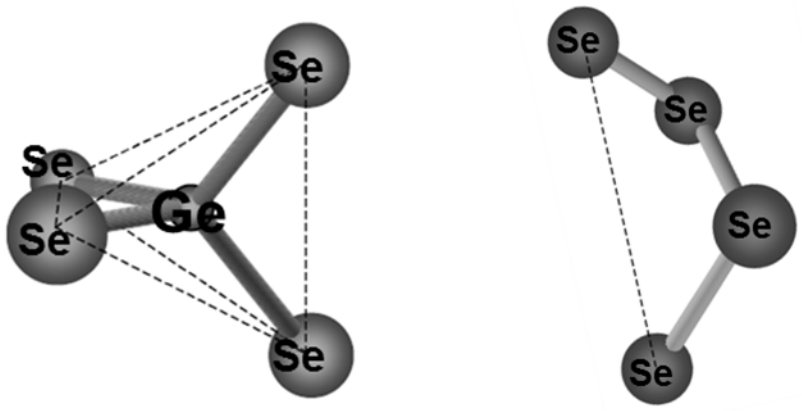

Figure 14. Schematic representation of $GeSe_4$ tetrahedra unit and Se-Se fragments in germanium selenide amorphous network.

The higher the concentration of Ge, the more the Se-Se chain/ring-like structures are replaced by $GeSe_4$ tetrahedra. Various combinations of tetrahedra are possible in the glass. The most common are the so-called corner-sharing (CS) and edge-sharing (ES) configurations (Figure 15). As can be seen from Figure 15, in the corner-sharing combination, two neighboring tetrahedra share one Se atom. In edge-sharing two Se atoms are shared. Another important bonding configuration which becomes more and

more frequent as Ge content exceeds 33% is so-called ethylenelike (ETH or ET) Ge-Ge bond (Figure 15, bottom configuration).

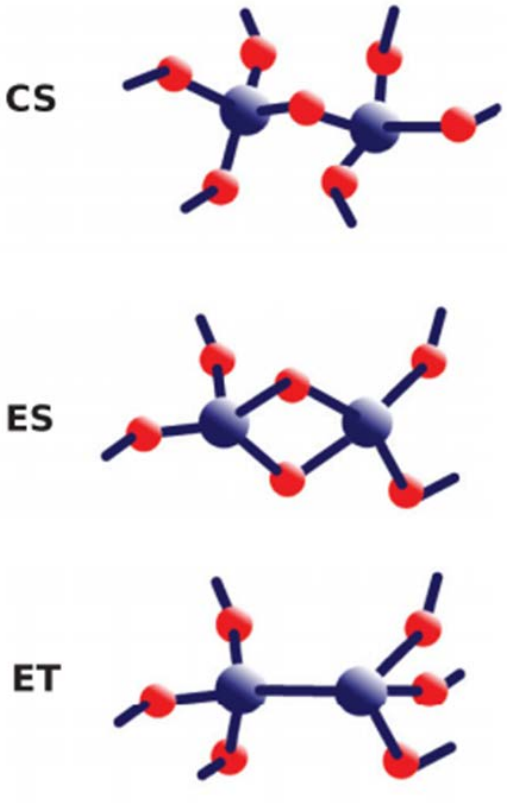

Figure 15.Illustration of corner-sharing (CS), edge-sharing (ES) configurations of $GeSe_4$ tetrahedra; and ethylenelike (ETH or ET) Ge-Ge homopolar bond configuration [79].

Naturally the more Ge atoms introduced into the flexible Se-Se matrix the stiffer the material network becomes due to the progressively increased mean coordination number [79]. This corresponds to transitions from the flexible phase with dominant Se-Se bonding configuration to an intermediate phase (IP) with a significant fraction of ES and CS configurations and eventually to a high rigidity phase rich in Ge-Ge ETH units [66,80] (Figure 16). This phenomena is of critical importance for both the fundamental understanding of the disordered states and promising technological applications of the Ge-Se class of glasses.

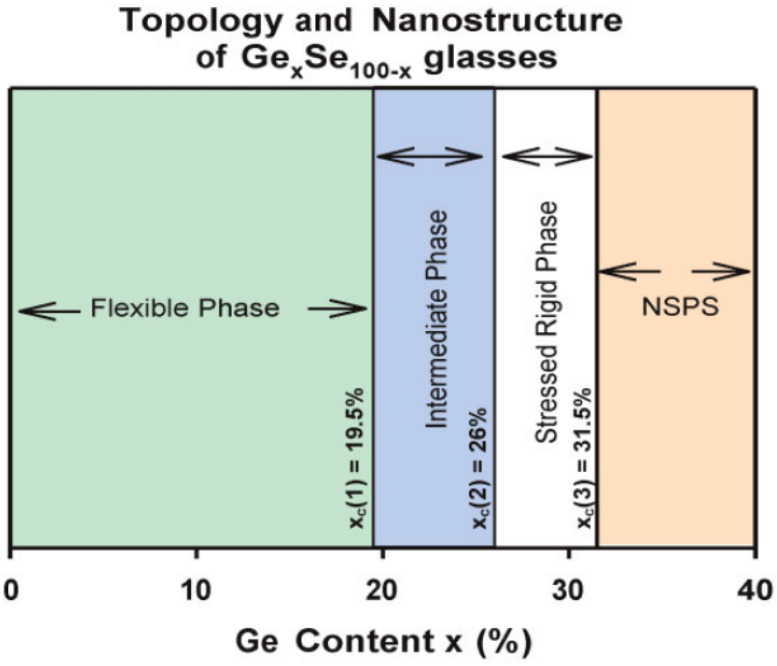

Figure 16. Elastic phases of Ge_xSe_{100-x} glasses showing evolution from flexible to rigid, nanoscale phase separation (NSPS) phase [66].

2.2.2. Raman spectra for a-Ge_xSe_{100-x}

Classification of Raman-active modes of Ge-Se system is more complex than that of pure a-Se, since different concentrations of four-valence Ge atoms permits different bonding with Se or Ge atoms in the amorphous network. Raman spectra of Ge_xSe_{100-x} compounds typically have four main features: (1) 179cm^{-1}peak is due to Ge-Ge homopolar ethylenelike (ETH) structural units; (2) and (3) 195cm^{-1} and 214cm^{-1} peaks are due to the symmetric stretching of all Ge-Se bonds of $GeSe_4$ tetrahedra in corner-sharing (CS) and edge-sharing (ES) configurations respectively; (4) a wider frequency band centered at about 250cm^{-1} corresponding to the bond stretching in Se-Se ring-like and chain-like fragments. Sometimes, the asymmetrical stretching of ES bonds at 305cm^{-1} are mentioned as the 5th region [75]. Aforementioned, intensities of the bands, especially ETH and Se-Se vary depending on the Ge content, as shown in Figure 17 [81].

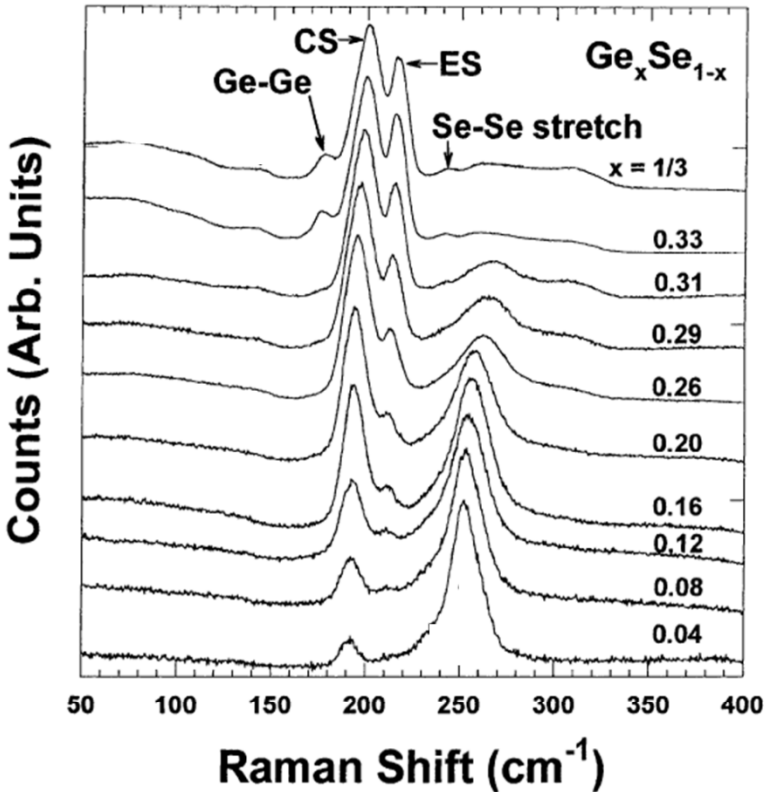

Figure 17. Raman spectra of Ge_xSe_{100-x} with glass compositions given alongside the spectra [78].

The Stokes part of the Raman spectra for different glass compositions demonstrates that as Ge concentration increases from 4% to 33%, the intensity of the ES (195cm^{-1}) and CS (214cm^{-1}) peaks increases, while bond stretching vibrations of Se-Se at ~250cm^{-1} naturally fade out as more and more Ge atoms are introduced into the network and are making bonds with Se atoms. In addition, as Ge % reaches 33.3% the ETH units with corresponding vibrations start to appear (Figure 17).

Usually, the edge-sharing to corner-sharing ratio is monitored to probe the variation in glass bonding as a function of Ge content or as the result of light-induced transformations. Light-induced effects on this ratio will be discussed in Chapter 5 based on our experimental data [82], however an example of an increase of ES:CS ratio due to an increase in atomic fraction of Ge is demonstrated in Figure 18. The non-linear increase in ES:CS ratio as a function of germanium concentration is observed. The ratio reaches

its maximum at 33.3% of Ge, which corresponds to the maximum Ge % investigated under the scope of the study [81].

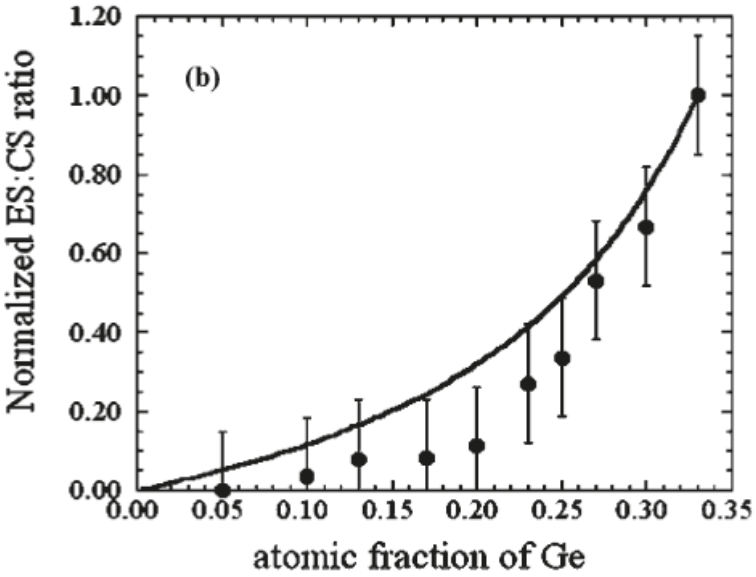

Figure 18. Normalized fraction of ES:CS species vs. atomic % of Ge. Dots represent experimental data [81] and solid line represents theoretical prediction [76].

2.2.3. Density of states in Ge-Se glasses

The most recent, comprehensive electronic density of states diagram for germanium selenide glasses for different % of Ge by Micoulaut et al. is shown in Figure 19. The black line represents computed DOS using Density Functional Theory (DFT) in comparison with other theoretical band theory work in red opened circles [83] and experimental data from x-ray photoemission spectroscopy (black opened circles [84] and red filled squares [85]. The valence band structure consists of two Ge and Se 4s bands deep in the valence band from -15eV to -5eV (C and B respectively), followed by 4p bands (A_2-A_3 for Se and A_1 for Ge) from -5eV to -2eV the intensity of which varies with Ge content. The conduction band is characterized by α and β peaks from 2eV to 4eV. Whereas α peak is assigned to the Ge 4p electrons, Se 4s and 4p electrons contribute to both α and β peaks. The change in CB structure takes place when Ge concentration reaches 20% and one broad conduction band is transformed into two distinct peaks.

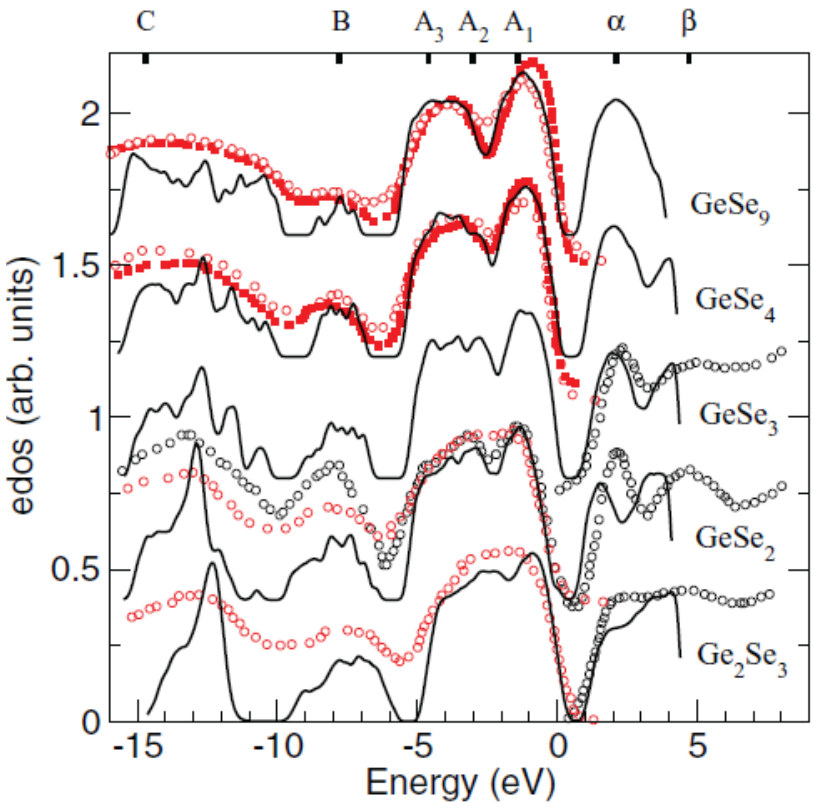

Figure 19. Electronic density of states for different Ge-Se compositions [79].

This transition also corresponds to the stiffness change from flexible to rigid phase through the intermediate phase [66]. However, at x=40%, the α peak is smeared out and β becomes dominant. In terms of energy gap (E_g), its width increases from 1.5eV to 1.8eV across the glass compositions, but one has to take into account the well-known error of DFT in E_g underestimation [79]. For instance, other experimental studies reported optical energy gap varying in the range from 2.0 to 2.3eV when Ge % changes form 15% to 33% (Figure 20) depending on the sample preparation methods and ways to calculate optical band gap [66]. Bandgap estimation based on optical absorption measurements (corresponding to absorption coefficient of $5x10^3 cm^{-1}$) resulted in an open circles data marked as E_{53} in Figure 20. The Tauc edge method revealed slightly different results E_T shown as filled circles in Figure 20.

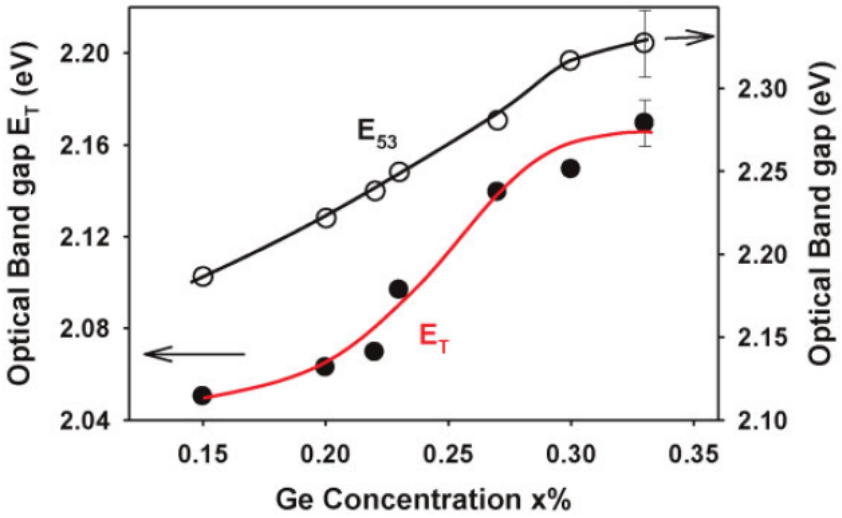

Figure 20. Compositional variation of optical band gap in Ge-Se glasses, reported by different research groups, where E_{53} corresponds to absorption coefficient $5x10^3 cm^{-1}$ and E_T to Tauc edge [66].

2.3. Photo-induced metastability in ChGs

Structural disorder of amorphous semiconductors permits alternative bonding configurations. This variation is thermodynamically driven due to the fundamental metastability of the amorphous phase with respect to the crystalline one and it can be further enhanced by excitation of different kinds, e.g. by means of optical and X-ray radiation, heat or electric field. On the microscopic level this is caused by electron excitation which destabilizes the bonding configuration of an atom. This change in the atom coordination can be adapted due to the amorphisity of the random network. Thus, an electron excitation from bonding to anti-bonding state can trigger structural rearrangement or *metastable* defect creation. Word *metastable* means that the lifetime of the change is relatively long but a more stable configuration (with respect to metastable one) exists. Thus, there is always a possibility for the system to come back to its initial or thermodynamically more stable form. In other words, metastability is a stable state which is higher in energy than lowest possible energy state, the so-called ground state of the system.

Structural transformations triggered by optical excitation, i.e. photo-induced structural metastability, is typical for chalcogenide glasses. It manifests itself in changes in the macroscopic properties of the glass under the action of strongly absorbed light. Photo-structural changes can involve creation of defects (e.g. dangling bonds and over-coordinated atoms) as well as bond switching. Understanding photo-induced metastability is important for two major reasons; first, it has to be prevented when causing material instability and thus degradation in e.g. applications in sensing; second, it can be tamed for the direct application of light-induced metastability effects in e.g. memory devices. [86,87,88].

The metastable nature of the photo-induced effects is usually subdivided into two types: reversible and irreversible. Reversible effects may occur on a time scale of less than a second to hundreds of hours, whereas irreversible are considered permanent. In addition to metastable photo-induced effects transient effects are observed. Transient changes are observed only when the photo-excitation occurs.

Within the scope of this thesis, several unique light-induced effects, including photodarkening (PD), photobleaching (PB) and photo-induced crystallization (PC) are studied and discussed.

2.3.1. Photodarkening and photo-induced crystallization in a-Se

The photodarkening (PD) effect is the red shift of the absorption edge (or decrease of the bandgap) as the result of prolonged exposure to light is a well-known consequence of photo-induced metastability in chalcogenide glasses. Reported in the 60s-70s in films and bulk glasses of selenium and sulfur compounds [89,90] it is still studied today and not understood conclusively [21,91,92]. A distinction is made in the literature between the PD effects for freshly as-deposited films compared with well-annealed structures. On the one hand, in the annealed amorphous glasses, reversible photodarkening effect is usually observed, which is well repeatable and is independent of sample irradiation history. Freshly deposited films, on the other hand, are more prone to an irreversible red shift in absorption which is attributed to the non-settled structure after evaporation. This shift can

be partially restored after subsequent annealing near the glass transition temperature (T_g) [57]. Glass transition (occurs around T_g) is one of the three phases, namely glass transition, crystallization and melting, which a-Se exhibit as an inorganic polymer glass when heated at constant rate [34]. T_g marks the onset of softening or can be also defined as the transforming temperature below which viscosity grows exponentially and supercooled liquid possesses properties of glass [6]. It has to be noted that T_g in not strictly defined and depends on heating or cooling rate, in a-Se it is reported to be around 42^{o}C or 315 K [93,94]).

There is a consensus in the scientific community that photodarkening is caused by band broadening due to increased local structural disorder and defect creation, including: bond switching phenomena [95], VAP creation [42] or homo- to hetero- polar bond conversion in multicomponent solids [96,97]. Several models have been proposed to explain the PD in terms of an *exciton model* by Street or an *energy/configuration model* by Tanaka.

The exciton model hypothesizes that the photodarkening effect in ChGs is caused by the creation of a metastable state corresponding to a self-trapped exciton. When an optical photon is absorbed, an electron-hole pair is created which generates an exciton. Two scenarios are then plausible; the exciton can recombine or it can become self-trapped. In the case of recombination, the original ground state configuration is restored with no distortion in the lattice. In the case of trapping, strong electron-phonon coupling diminishes the exciton energy and the radiative recombination is not possible. This results in strong distortion in the lattice [98]. Consequently, some photo-generated excitons become self-trapped forming metastable states within the band tails which causes the PD effect. In order for the system to relax back to the original ground state thermal excitation is necessary, since radiative recombination is not possible.

Tanaka has proposed an energy/configuration diagram to explain and quantify the photodarkening effect (Figure 21) [99]. He characterized the ground state of the system by a double-well potential with the local minima X and Y separated by potential barrier E_B. Illumination corresponds to excited electronic state characterized by a single-well

potential, with the single minimum Z. Excited state Z is exactly above the local minimum of ground state Y.

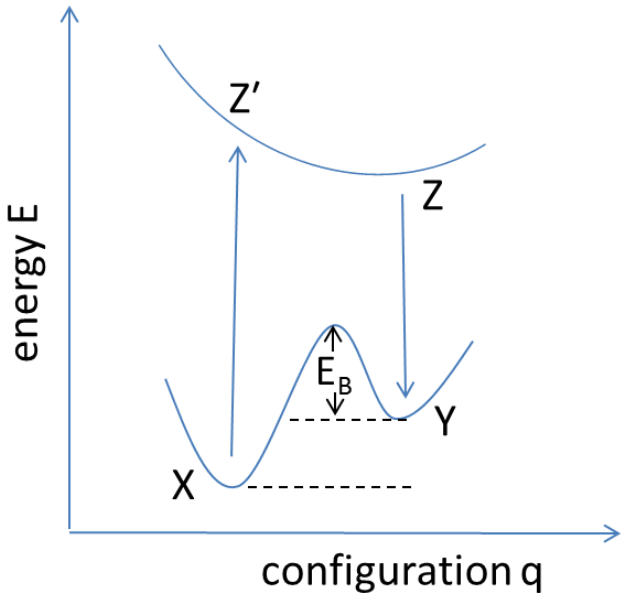

Figure 21. Energy- configuration model for PD effect. X corresponds to the lowest energy initial ground state, Z to the excited state and Y to the metastable state responsible for the photodarkening effect.

An electron from its ground state configuration X is photo-excited to Z′ state. Following photoexcitation carriers can either recombine restoring the initial X-state or can thermalize to Z (Z′→Z) and become trapped in the upper potential well Y (Z→Y). Thus, the metastable state creation follows the path X→Z′→Z→Y. Accumulation of sites in the Y configuration enhances the density of deep states in the band tails causing the amorphous structure to become more disordered, thereby giving rise to a wide range of photo-induced phenomena, including the PD effect [22,99,100,101,102,103,104,105]. Subsequent thermal annealing provides energy to overcome the barrier E_B and for the structure to relax back to its ground state X. This configuration-coordinate picture, or proposed variations that include a 3rd intermediate configuration [106], are quite general, and can encompass the formation of coordination defects [21,107], as well as the self-trapped exciton model proposed by Street [98]. The barrier height can be quantified from

temperature dependent measurements assuming the photodarkening amplitude is proportional to the density of Y configuration defects.

Tanaka's phenomenological approach was clarified in our recent paper (Ref. 25). A diagram of the photo-excitation process extracted from this paper is presented in Figure 22 and can be explained as follows: excitation of electrons brings the system from a ground state A (an analog of X configuration in Tanaka's model) to an excited state A^*, assuming that an electron excited into the conduction band leaves behind a hole in the valence band tail. The state in the valence band tail is missing one or two electrons and thus induces lattice relaxation of the immediate neighbourhood needed for its stabilization. As a result, the excited A^* state converts either into a B^* or C^* state. The B^* state accounts for the insignificant lattice relaxation involving the bond shortening or elongation and as such is characterized by a small decrease in energy ΔU_{EB}. When the missing electron returns, the B^* state is able to relax into the original ground state A.

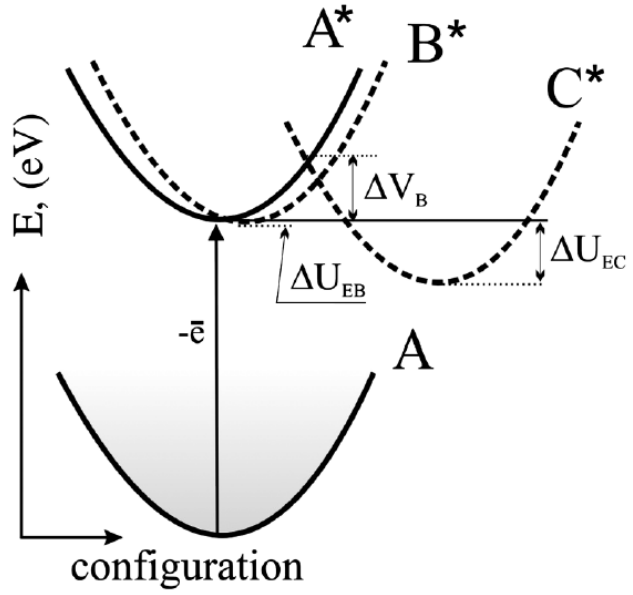

Figure 22. Potential diagram describing an excitation of the A state and contribution of the photo-induced lattice relaxation into the stabilization of the excited state A*. The energy scale reflects the total energy of a system [25].

This mechanism is assumed to be responsible for transient photodarkening that exists only while the optical excitation lasts. In contrast, the C^* state results in bond

rearrangement reflected in the large ΔU_{EC}. The $A^* \rightarrow C^*$ transition requires overcoming the potential barrier ΔV_B, and it is hypothesized that the former is responsible for metastable photo-induced effects since C^* is not restored to the original A^*. As a result C^* relaxes to a fundamentally more stable configuration (an analog of the Y state in Tanaka's model).

All of the above mentioned models are focused on a metastable PD explanation. In contrast, the transient photo-induced effects are assumed to be caused by electron transitions between ground and photo-excited states, with no metastable states being involved [108]; or by dynamic bond formation and its almost immediate restoration. The latter was experimentally demonstrated by Kolobov et al. by their *in situ* EXAFS study, where the average coordination number of a-Se was shown to increase by 5% upon bandgap light irradiation at 30K [42]. This was explained as the formation of a threefold dynamic bond between excited atoms, which causes structural disorder. Overall, three pathways for relaxation were suggested after a threefold dynamic bond is created (Figure 23).

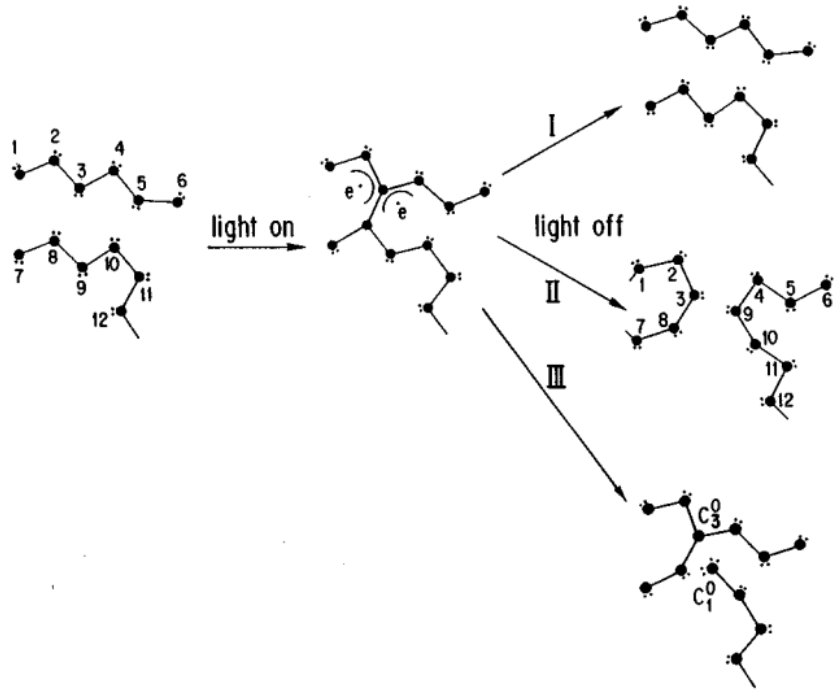

Figure 23. Schematics of local structural disordering and transformation as the result of light irradiation [42].

Path I results in restoration of the initial bonding configurations; while in the path II a bond switching process occurs with no change in coordination of the participating atoms and in path III coordination defects are introduced, namely the combination of one-fold and three-fold coordination sites. Naturally the first two would be responsible for transient light-induced effects that are observed due to the structural disorder and disappear as the illumination is terminated.

Photo-induced crystallization (PC) of a-Se is an irreversible relaxation phase change that occurs well below the amorphous selenium crystallization temperature when optical excitation enhances the transition from an amorphous phase to the thermodynamically preferred crystalline phase. The rate of PC is fast at temperatures above the glass transition. However, when a-Se layers are deposited on rigid substrates PC occurs even at temperatures well below the T_g [21]. This behavior is related to the substrate-generated shear strain which is known to promote the PC process [46]. In spite of studies by many researchers [109], a full understanding of factors that control PC in film structures, i.e. different substrates, growth conditions and temperature remains elusive. It has been established that: (1) crystallization is initiated preferentially at the substrate interface [110,111,112]; (2) strain is an important factor in this tendency [113,114] and (3) that crystallization is enhanced by light [111, 113, 112, 114].

Several studies have employed Raman spectroscopy [46,115,116,117], X-ray diffraction, and atomic-force microscopy [118,119] to investigate aspects of the PC process related to the microscopic changes in structure that drive the *primary* nucleation of t-Se domains. There is a broad consensus that at the atomic level these changes are caused by a variety of bonding defects, such as dangling bonds and valence alternation pairs [120]. Surprising thermal behavior near the glass transition was reported by Tallman et. al.[46], showing a discontinuous increase in the PC onset time (time when t-Se peak becomes detectable) as a function of temperature (Figure 24). This was observed by means of Raman spectroscopy when the crystal growth kinetics were monitored at different temperatures. As the result, distinct temperature regimes are defined [46]. Whereas no photo-induced crystallization was seen below 260K and around the glass transition, temperature-dependent PC is evident from 260K to 302K and above the glass

transition (Figure 24). Temperature dependent regimes are shown to exhibit Arrhenius behavior with activation energies of 0.8-1.0eV. Another study [121] of glass-deposited a-Se structures found similar jumps in the PC onset times near T_g, but the temperature ranges varied widely.

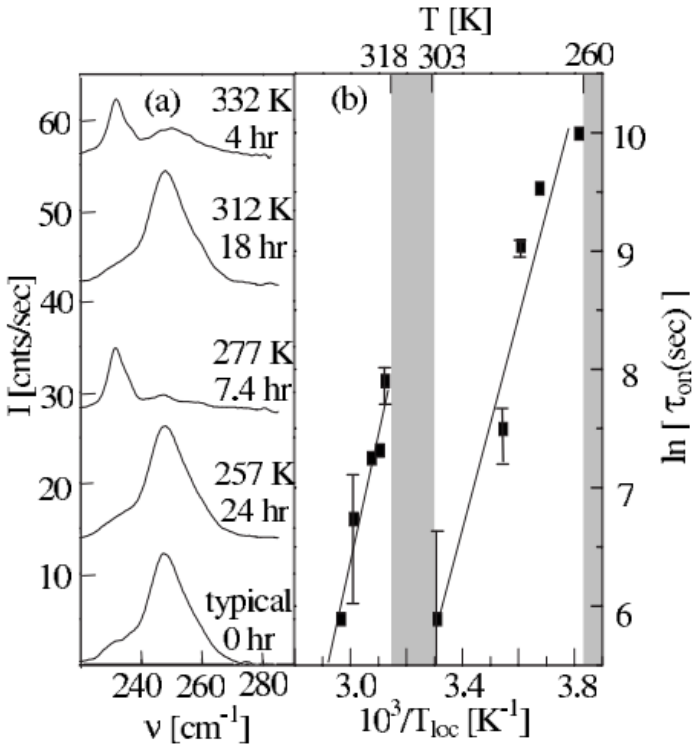

Figure 24. Thermal behavior of the PC onset times. On the left: comparison of typical and post-exposed a-Se Raman spectra at given temperatures and time of illumination. On the right: PC temperature regimes [46].

Historically, PC and PD were treated as independent processes, although as was discussed above, several studies suggest that structural changes are caused by an increased level of structural disorder and/or defect creation process. Recently Reznik et al. linked photo-induced crystallization and photodarkening [122]. They have estimated the height of the barrier E_B in the energy-configuration model for photodarkening and showed that photo-induced crystallization is a thermally activated process with an activation energy identical to E_B. Due to the similarity between the activation energies for both processes Reznik et al. suggested that PD and PC are of the same nature, and

agglomeration of states in Y configuration (Figure 21) can cause an increase in barrier height, thus making relaxation from Y to X state less probable. An additional argument to support the similarity between PD and PC was provided by an experiment at elevated temperature, just below the glass transition temperature for a-Se (35^0C). At this temperature both the irreversible component of PD and PC were not observed [46, 92]. Although elevated temperatures cannot prevent the appearance of Y states upon excitation (indeed a double-well configuration is a fundamental feature for a-Se), structural relaxation at temperatures close to T_g does prevent agglomeration of Y states and as such restricts transformation to a crystalline phase. Indeed, direct Raman measurements of PC at 35^0C, does not show an appearance of a t-Se peak, although this peak appears at other temperatures after several hours of continuous illumination (Figure 24).

The majority of studies on PD have been done using *sub-bandgap* illumination (which was shown to be effective in causing the pronounced effects). The effect of *above-bandgap* illumination on PD has been studied far less, particularly for a-Se, although it was reported that the photodarkening amplitude levels off or decreases for short wavelength excitation [103]. This finding is quite encouraging since it suggests that the resistance of a-Se to photo-induced structural changes at higher energies of excitation is enhanced, which is particularly important for applications of a-Se in optical and X-ray sensors. As such it deserves further analysis and theoretical support.

A comprehensive study of different PD components under sub-bandgap and above-bandgap illumination is carried out over a wide temperature range as a part of this PhD work. Our experimental results demonstrate dramatically different PD kinetics for above-bandgap and sub-bandgap excitation and allow us to define different relaxation mechanisms responsible for transient and metastable photodarkening in different energy regimes [123]. Chapter 4 is dedicated to the results, discussion and conclusions of our findings.

Due to the obvious need for clarification and explanation of the connection between strain and the thermal aspects of the observed PC effects we explore the influence of different substrates (Si and glass), and different film-layer-substrate

combinations, for a variety of a-Se films and multi-structures. Intermediate layers (indium tin oxide and polyimide) are chosen to promote conductivity and/or to buffer against interface strain in the structures of interest for digital imaging applications. The PC characteristics in these samples are evaluated and analyzed using optical microscopy, atomic-force microscopy, Raman mapping, and temperature-dependent Raman spectroscopy. Our findings and conclusions are published in Ref. 124 and presented in Chapter 4.

2.3.2. Photodarkening and Photobleaching in a-Ge_xSe_{100-x}

A short overview of PD/PB effects in a-Ge_xSe_{100-x} glasses is reproduced here from our recent publication [82].

The reverse process of photodarkening is the photobleaching (PB) effect. Photobleaching is a blue shift of the absorption edge or an increase of the bandgap under light irradiation commonly observed for Ge-containing chalcogenides [70]. In Ge-Se glasses two types of light-induced effects are observed, namely photodarkening and photobleaching. Similar to other ChGs, PD and PB arise from unique electronic and atomic structural peculiarities and the lack of periodicity in Ge-Se systems, as well as from a special feature, the availability of lone pair states [125]. The former allows structural reorganization with or without bond breaking [25,126], including a combination of inter-molecular and intra-molecular bond scission or weakening under light irradiation [127]. Thus, both PD and PB effects are predominantly related to structural transformations [128,129]. While the PD mechanism is better understood in a-Se due to extensive study and explained using the models described in section 2.3.1, the underlying mechanism for photobleaching is still the subject of controversy. Two different causes have been reported in the literature. One explanation assigns PB to the local structural reordering as the result of excitation-triggered conversion of homo-polar Ge-Ge bonds to hetero-polar Ge-Se ones [67,130]. The second attributes the phenomena to the photo-oxidation process which involves Ge-O bond formation [68,131]. The latter effect is difficult to observe directly with available methods of structural analysis such as Raman spectroscopy because of the limited oxygen and low vibration intensity of the

oxygen-containing bonds. For oxide-containing compounds, the key methods used to investigate the structural changes are indirect, such as infrared (IR) spectroscopy. Tichy et al. [132,133] ascribe the increase in the amount of oxygen to a shift in the IR spectra to smaller wavenumbers associated with an increase in local electronegativity. Controversial results about weight and thickness loss in obliquely deposited films are reported by Rajagopalan et al. [134] and Harshavardhan et al. [135], which were related to the formation of volatile, chalcogen-based oxides. They do not describe such effects for normally evaporated films however. One investigation of photo-oxidation suggests that an oxide film is formed on the surface, thus producing strain at the interface that in turn induces states in the band gap [131]. Bearing in mind the basic relationship between structure and optical performance, this contradicts the general view that oxidation is identified with bleaching of the glass [136]. In addition, both metastable and transient PB/PD effects in Ge-based glasses are reported in the literature [67,68].

Recent results have demonstrated that in a-Ge_xSe_{1-x}, glass composition plays a key role in the observed photo-induced transformations [137]. A few groups published the results showing that as Ge content increases, the crossover from PD to PB is seen experimentally [67,138]. In particular, for x<20% only photodarkening was observed and further Raman analysis revealed that the effect is caused by structural rearrangements, i.e. photocrystallization of Se [138]. As the Ge content is increased photo-induced crystallization is suppressed and around x=20% is no longer present. Beyond 20% experimental data showed a mixture of PD and PB effects. It is important to emphasize that one of the main challenges of revealing the nature of PD/PB effects is the inherent alteration of the glass topology in Ge-Se glasses [79]. With the increasing number of Ge atoms in the glass network, the mean coordination number increases, and this results in an evolution from flexible (x<20%) to a stress-rigid network (x>30%), separated by an intermediate phase (IP) (20%<x<30%) [66].

While, there are many studies dedicated to the flexible phase, not much investigation has been done for the stress-rigid phase, including $GeSe_2$. In addition, most of the photo-induced effects data available is on its fast kinetics (time intervals of fs and ns) due to the high priority of short response times for practical applications. Very limited

data has been reported on slow kinetics (time intervals of seconds), although it has been recently shown that by increasing the exposure time the transition between PD and PB effects becomes apparent, which demonstrates the dual role of light for the occurrence of photo-induced effects in ChGs [67,138,139].

To reveal the microscopic nature of the light-induced effects in a-Ge_xSe_{100-x} we have conducted a comprehensive study of transient and metastable PD and PB effects across the glass-forming region, with a special emphasis on high-rigidity compositions (x~>30%). Our findings are presented in Chapter 5.

CHAPTER 3

Experimental techniques and setup details

Two optical techniques were utilized to study photodarkening and photobleaching effects in a-Se and a-Ge_xSe_{100-x} glasses. (1) A two-laser beam technique was employed to introduce photodarkening and photobleaching effects by generation of defects and to simultaneously monitor PD/PB kinetics. (2) Raman spectroscopy was chosen as a nondestructive method to probe the structural changes associated with photo-induced effects.

The photo-crystallization study was performed by means of temperature dependent Raman Spectroscopy and co-localized Raman - atomic-force microscopy (AFM) mapping.

3.1. Two-laser beam technique for PD/PB study

The two-laser beam technique is based on the idea of monitoring changes in sample transmission with a non-destructive low-intensity laser beam (*probing* beam), while another high-intensity laser (*pumping* beam) induces photodarkening/photobleaching effects. This provides several advantages over conventional one-laser beam methods, where one illumination source is employed to introduce photo-induced effects and to record changes in transmission [21]. The two-laser beam method allows us to study both defect creation and subsequent defect relaxation kinetics, and it can distinguish between metastable and transient light-induced effects.

The schematics and photo of the experimental setup that was built and utilized over the course of the PhD studies is shown in Figure 25. The pumping laser of the high intensity worked in an on/off regime, introducing the light-induced changes when it is "on" and allowing the structure to relax when it is "off". Low-intensity probing light was used to continuously monitor changes in the transmission (T), so that relative changes in the transmission (T/T_0) as a function of time were collected.

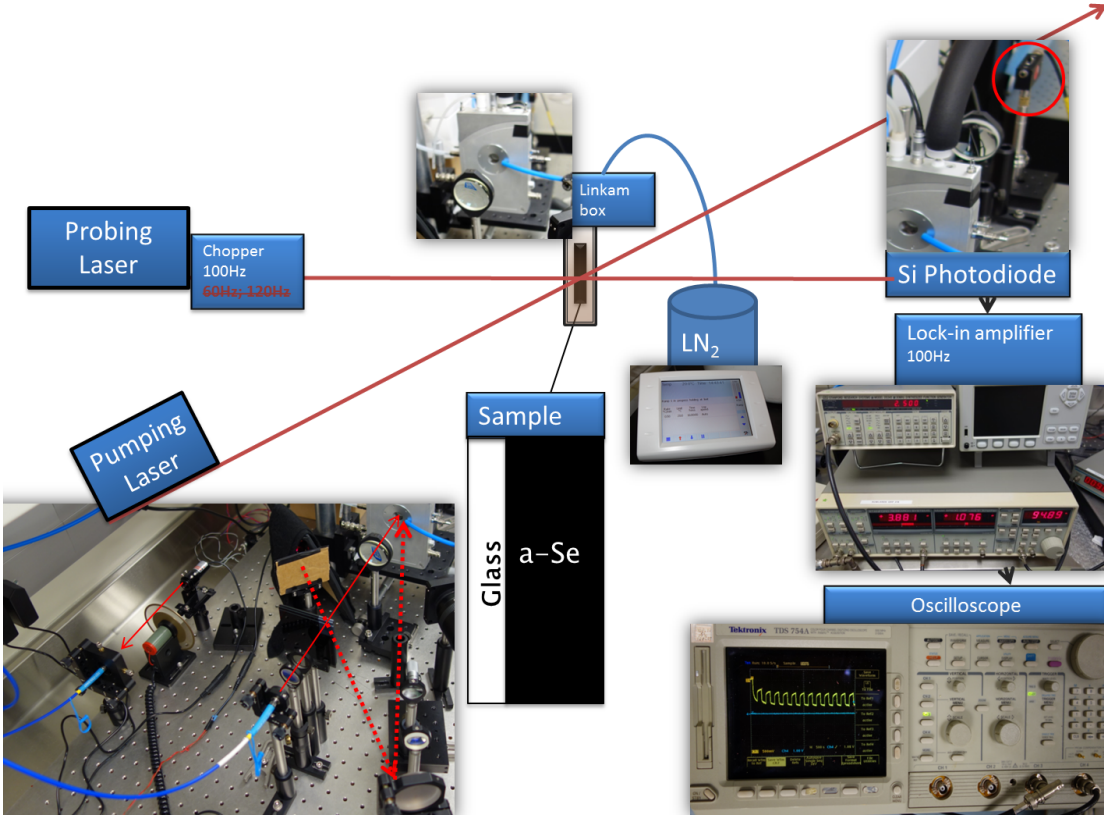

Figure 25. Experimental apparatus for PD temperature-dependent measurements carried out on a-Se samples.

In our setup the probing light was first chopped at 100Hz frequency and then guided by fibre optic cables and series of lens to pass through the sample and to be collected by Si photodiode (Thorlabs 201/579-7227). A mechanical chopper and lock-in amplifier (Stanford Research Systems SR830 DSP) were used to completely eliminate the effects of ambient light. Lenses and additional attenuator glasses were used to provide low intensity probing light. The on/off cycling of the pump was produced by a function generator (Stanford Research Systems DS345). To ensure complete overlap between pump and probe beams, the beams diameters were set to 4.4mm and 1.6mm respectively. A temperature controlled stage Linkam Box (LINKAM LTS350) was employed for heating/cooling control and temperature stabilization. Liquid Nitrogen was used as a cooling agent allowing for a wide temperature range of measurements. The heating/cooling rate was set to 0.5^{0}C/min. Data was gathered with an oscilloscope (Tektronix TDS 754A).

In the beginning of each experiment the initial transmittance of the sample (T_0) was measured with weak probing beam for 30 min to ensure that the probing beam did not cause changes in transmission.

For the photodarkening study in a-Se, a probe beam of 655nm wavelength and 0.29mW/cm^2 intensity was utilized. The pump beam was chosen to be either 150mW/cm^2 at 655nm for sub-bandgap excitation or 200mW/cm^2 at 405nm for above-bandgap excitation. Both were found to be high enough to produce the PD effect but low enough not to cause sample overheating. The pump cycling period was set to intervals of 200s separated by 200s periods of rest. The intervals were found to be optimal for our investigation. Amorphous selenium samples were annealed after each photodarkening experiment at 35^{0}C (slightly below the glass transition temperature T_g~42^{0}C [123]) for a period in the range 24-48hrs until the initial transmittance level was restored. It was empirically found that depending on the magnitude of metastable PD component that was produced during the experiment, if the sample was not annealed at 35^{0}C, transmittance would take from 4 days to weeks at room temperature to recover to the initial level. Different areas of the same sample as well as samples from different deposition runs (see Appendix A for samples details) were tested to confirm the reproducibility of the results.

In the case of photodarkening/photobleaching study of a-Ge_xSe_{100-x} films, the probe beam was the same 0.29mW/cm^2 at 655nm and a high-intensity 200mW/cm^2 pump laser of 405nm was used to produce PD/PB effects. The pump laser worked in an on/off regime with a period of 400s.

3.2. Raman spectroscopy

3.2.1. Setup details for Ge-Se light-induced effects study

Raman analysis for a-Ge_xSe_{100-x} was performed on pre- and post-exposed samples to track the structural changes linked to the metastable photodarkening and/or photobleaching effects, or to confirm that the observed transient PD/PB effects did not cause any structural transformations. Raman spectra were obtained in backscattering geometry in macro mode using a Horiba Jobin Yvon T64000 triple monochromator with

a liquid-nitrogen-cooled, multichannel coupled charge device detector. Films (for the preparation details see Appendix A) were excited with the 441.6nm blue line from a He-Cd laser at a power of 25mW and with a circular area of ~0.2mm. This light intensity did not cause any structural changes itself. In addition, to avoid photo-induced changes by the laser light of the Raman system in the studied glasses, we conducted measurements at liquid-nitrogen temperature and at a pressure of 10^{-5}Torr. Each Raman spectrum was collected over a period of 60 seconds and normalized to the corner-sharing (CS) peak centered at 195cm^{-1}. Deconvolution of the Raman vibrational modes with a Gaussian shape distinguished each of the peaks. After fitting the areas under the individual peaks, integration of the bands centered at 195cm^{-1} and 219cm^{-1} revealed the fractional quantities of CS and edge-sharing (ES) structural units [81]. The accuracy of the fitting procedure is represented by the error bars on respective graphs in Chapter 5.

3.2.2. Setup details for a-Se photo-induced crystallization study

Co-localized Raman–AFM maps were recorded with a Horiba J-Y LabRam model HR800 spectrometer linked to an AIST-NT SmartSPM 1000 AFM unit. PC was induced using 632nm laser light at a power of 1mW focused (numerical aperture 0.7 lens) through the film at the film-substrate interface. The flux at the focus was ~ 0.15μW/μm^2 (decreased from 0.5μW/μm^2 at the surface, including absorption and refractive index corrections). The Raman mapping was performed using 632nm or 671nm laser lines at 10^{-2} lower power focused at the film-air surface to allow for comparison with the AFM surface profiles. The Raman maps were recorded with a 0.5μm step size (~1/3 the focused beam waist), and the resolution of the AFM profiles was 25nm. The sharp focus of the Raman mapping system and the film absorption reduced the flux by ~ 10^{-4} at the film-substrate interface where the PC initiated.

A different apparatus was used to study the onset-time of PC as a function of temperature. We employed conventional Raman spectroscopy recorded with the 647nm line of a Kr^+-laser at a flux of 1.3μW/μm^2. The same laser beam was used to induce the PC and to monitor the changes in Raman spectra; the exposure was continuous until the PC onset (the detectable peak) was observed (durations of ~ 5-500min.). For temperature

measurements samples were mounted in an optical cryostat that allowed precise temperature stabilization (+/-1K) over a wide temperature range. For each temperature a different sample spot was illuminated through the substrate side. The Stokes to anti-Stokes Raman ratio was calculated to determine the actual local temperature at this spot. The local temperature exceeded the cryostat set temperature by 32+/-5K and varied between 285-345K. The local temperatures are used in the discussion of the onset-time results in Chapter 4, i.e. the exposure time for the onset of crystallization. The recorded Raman spectra allowed us to monitor the frequency region $200cm^{-1}$ – $300cm^{-1}$, containing the strong A1-symmetry peaks of t-Se ($237cm^{-1}$) and a-Se ($256cm^{-1}$) [38,140]. PC was detected by an increase in strength (from zero intensity) of the t-Se peak and a simultaneous decrease of the a-Se peak.

CHAPTER 4

Photodarkening and Photocrystallization in a-Se

4.1. Photodarkenig in a-Se

To investigate the effects of above-bandgap and sub-bandgap illumination in a-Se and get insight into the microscopic nature of the effect, the photodarkening kinetics were studied experimentally by means of a two-laser beam technique on a high quality amorphous selenium (a-Se) layers (see Appendix A for sample preparation details). Throughout the experiment relative changes in the transmittance, T/T_0, are monitored. T/T_0 were measured in a wide T-range from -40^0C to 50^0C for different optical excitations: 655nm and 405nm. Distinctly different PD relaxation mechanisms are shown to be responsible for the above-bandgap excitation versus sub-bandgap excitation. In the case of above-bandgap only transient PD is observed, while in case of sub-bandgap, both transient and metastable PD are present.

The difference in PD behavior under above- and sub- bandgap excitations is confirmed by first-principle simulation. A so-called "double-electron" excitation is found to trigger the bond rearrangements and structural transformations responsible for the metastable PD. In contrast, a so-called "single-electron" excitation causes very weak lattice relaxation with no structural changes and is shown to be responsible for the transient PD.

These results have been published in Applied Physics Letters 105, 2014 (Ref. 123) and Physical Review Applied 1, 2014 (Ref. 25) and are presented in the next two subsections.

4.1.1. Experimental results and discussion on PD in a-Se

The collected data is presented in Figure 26 and Figure 27 for sub-bandgap and above-bandgap excitation respectively. It is clear that the kinetics and magnitude of PD are temperature and wavelength dependent, and there is a distinct qualitative difference in the observed behavior for sub- vs. above- bandgap illumination.

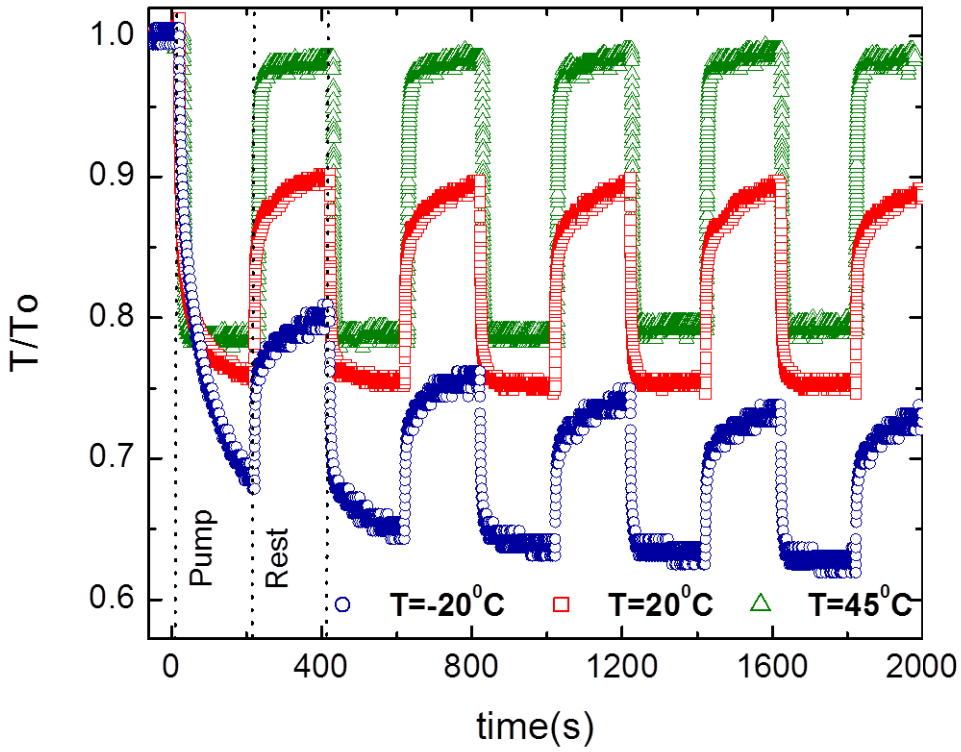

Figure 26. PD for selected temperatures: -20^{0}C, 20^{0}C, 45^{0}C in the case of 655nm excitation.

The results of the PD measurements with sub-bandgap illumination at three selected temperatures are shown in Figure 26 for five pump/rest cycles. Each cycle consists of 200s of pumping period followed by 200s of rest. It was found that, at all temperatures below the glass transition (T_g ~ 42^{o}C or 315K [93]), the transmittance drops during the 200s pump period followed by partial restoration during the subsequent 200s rest period (the results for -20^{o}C and 20^{o}C are shown in Figure 26 are the most illustrative). The lower the temperature, the larger the overall decrease in transmittance, which is

consistent with previously reported results [99]. Indeed, for T=-20^{0}C, T/T_0 drops by ~33% during the first pumping period, while for T=20^{0}C the corresponding decrease is ~25% only. During first rest period transmittance recovers partially at both temperatures. Partial recovery indicates the presence of both *transient* PD and *metastable* PD components at these temperatures [22]. For the transient component, full recovery is almost immediate on the time scale of our experiments. For the metastable component, the transmittance can be restored, but thermal annealing near T_g is required to reverse the decrease in T/T_0.This decomposition of the PD kinetics is supported by the noticeably different PD response measured at 45^{o}C (i.e., close to the glass transition temperature). For this temperature, T/T_0 is completely recovered at the end of each 200s rest period, and the required time of restoration is short, showing that the *metastable* component of PD has vanished, and only *transient* PD is present (Figure 26). This agrees well with

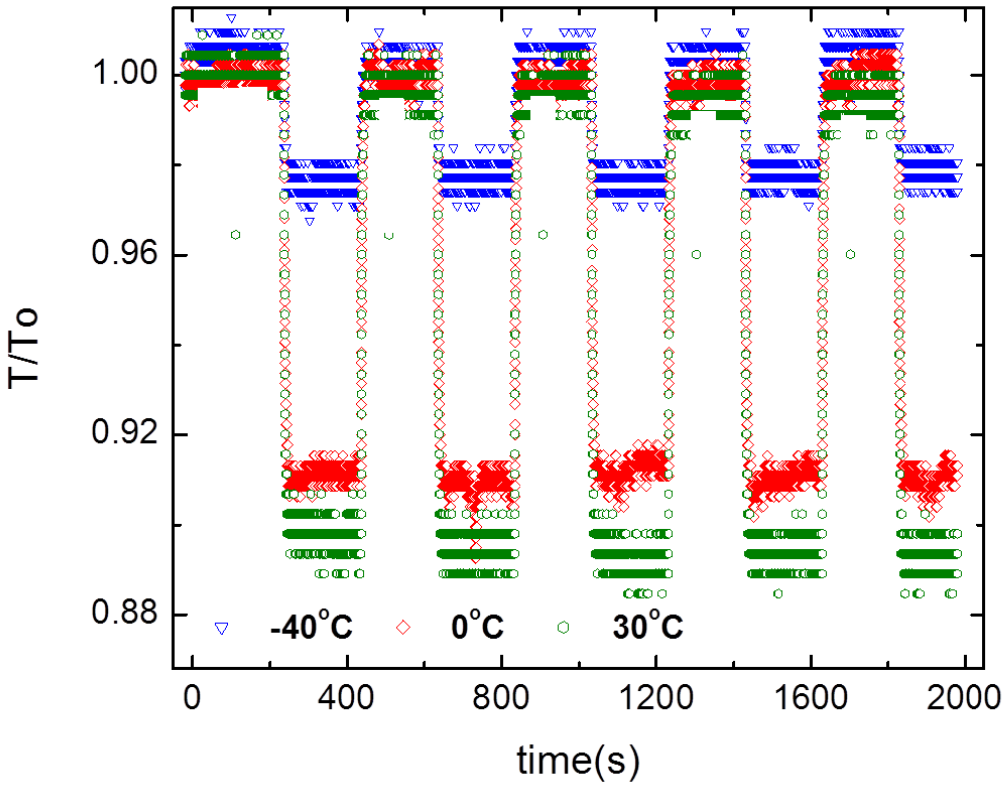

Figure 27. PD for selected temperatures: -40^{0}C, 0^{0}C, 30^{0}C in the case of 405nm excitation.

the kinetics of PD reported previously for a-Se samples that were not As-stabilized [92].

For 405 nm pump excitation the temperature behavior is markedly different. Only transient PD is observed in the wide temperature range from -40^{0}C to 30^{0}C: once the pump light is turned off the initial transparency is completely recovered (Figure 27).

To describe the observed relaxation kinetics of the PD we assume that the amplitude of darkening is linearly proportional to the number of excited electron-hole pairs (whether or not correlated), as has been shown in Ref. 92. Consider first the situation for above-bandgap excitation. When the pumping light is switched off the time dependence of the transmission can be described by the equation:

$$\frac{T}{T_0}(t) = 1 - A\exp\left(-\frac{t}{\tau_1}\right), \qquad (2)$$

where τ_1 is the characteristic time constant of relaxation, and A is the maximum PD amplitude. From the experimental data in Figure 27, we determine the characteristic time constant for each recovery cycle at different temperatures. It is found that for 405 nm wavelength excitation, T/T_0 recovers with τ_1 = 2.5s, identical for all temperatures under investigation here (example of fitting of one restoration cycle at 30^{0}C is shown in Figure 28(a) with the respective single-exponential fitting equation displayed on the graph). In fact, from the experimental data, averaging τ_1 for 32 cycles at every temperature gives a standard deviation of only $\pm$ 0.2s, showing that τ_1 has essentially no temperature dependence over a wide temperature range.

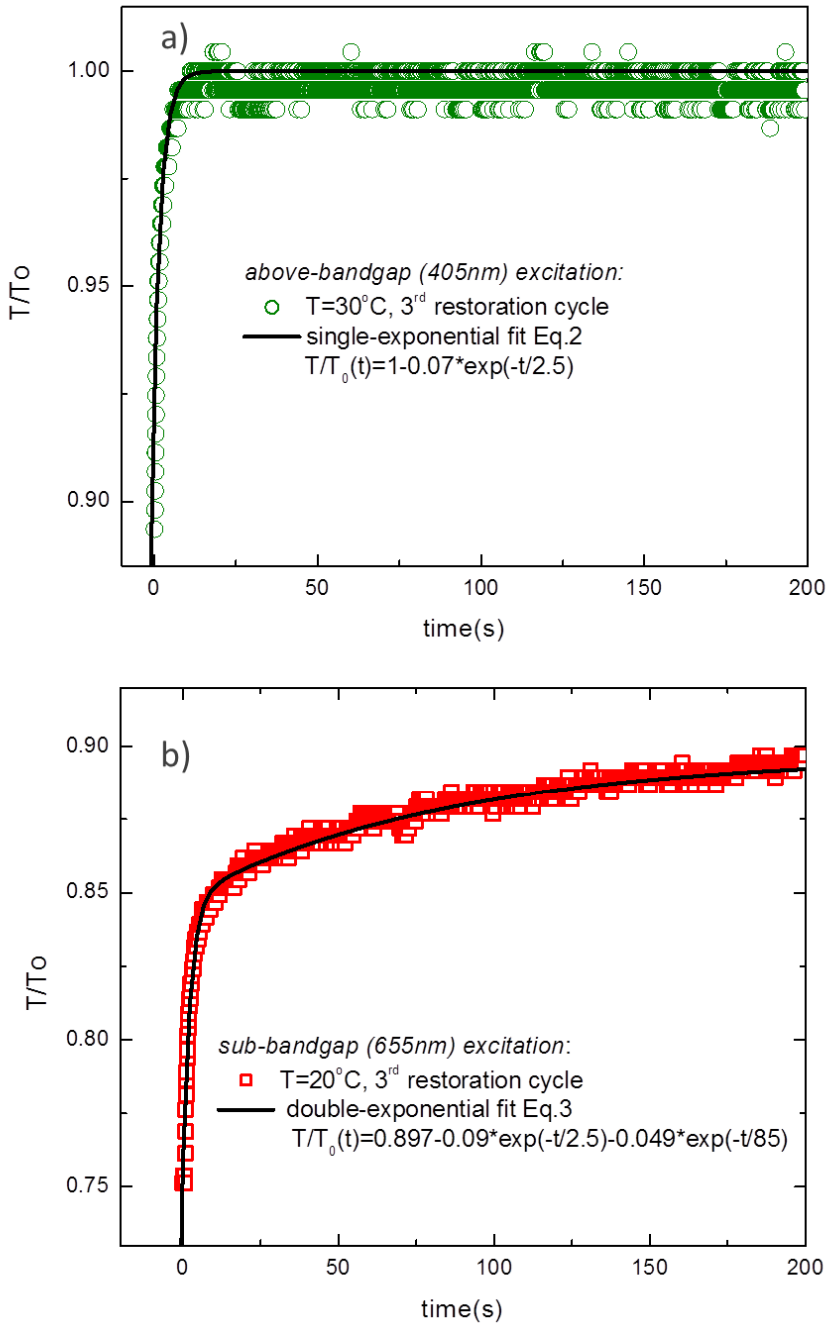

Figure 28. (a) Single-exponential fit of the 3rd restoration cycle in case of above-bandgap excitation. (b) Double-exponential fit of the 3rd restoration cycle in case of sub-bandgap excitation; equations of the respective fitting curves with characteristic times τ_1 and τ_2 are displayed.

In contrast, the single exponential decay fails for the longer wavelength (655nm) sub-bandgap excitation, and a double-exponential decay is needed to fit the experimental results shown in Figure 26:

$$\frac{T}{T_0}(t) = A_0 - A_1 \exp\left(-\frac{t}{\tau_1}\right) - A_2 \exp\left(-\frac{t}{\tau_2}\right) \qquad (3)$$

Here A_0 (<1) is an offset needed to compensate for incomplete restoration of the initial transparency within the duration of the experiment. Indeed, complete restoration at room temperature (RT) requires up to 3 days of rest, due to the formation of irreversible defects that need much longer time to relax. The lower the temperature, the longer the restoration time of the irreversible defects. Thus, for the study of short (a few seconds) and intermediate (tens of seconds) characteristic time constants, pump/rest periods are limited to 200s which allows for the accurate tracking of relaxation times of interest The double-exponential law (Eq. 3) indicates that two distinct relaxation processes are present.

Least-square-fitting of Eq.(3) to the data for 655nm excitation reveals that one process again can be described by a temperature independent relaxation time τ_1 equal to 2.5s (the same as for the case of above-bandgap pumping light). However the second process has a longer characteristic relaxation time τ_2 that is strongly temperature-dependent (example of fitting of one restoration cycle at 20^0C is shown in Figure 28 (b) with the respective double-exponential fitting equation displayed on the graph).

The measured dependence on temperature of τ_2 is shown in Figure 29. With decreasing temperature, τ_2 first increases sharply from 12s to 85s in the region of T_g, and then levels off at 85s for temperatures below 25^0C.

The temperature independence of the time constant τ_1 suggests that the corresponding relaxation process does not involve thermal activation over a large potential barrier. Our results show that τ_1 alone is needed to describe the relaxation of PD excited by the absorption of above-bandgap 405nm photons, whereas PD triggered by band-tail absorption exhibits, in addition to τ_1, a slower temperature-dependent relaxation

characterized by longer τ_2. We believe that the formation of self-trapped excitons in the latter case accounts for the difference between these observations.

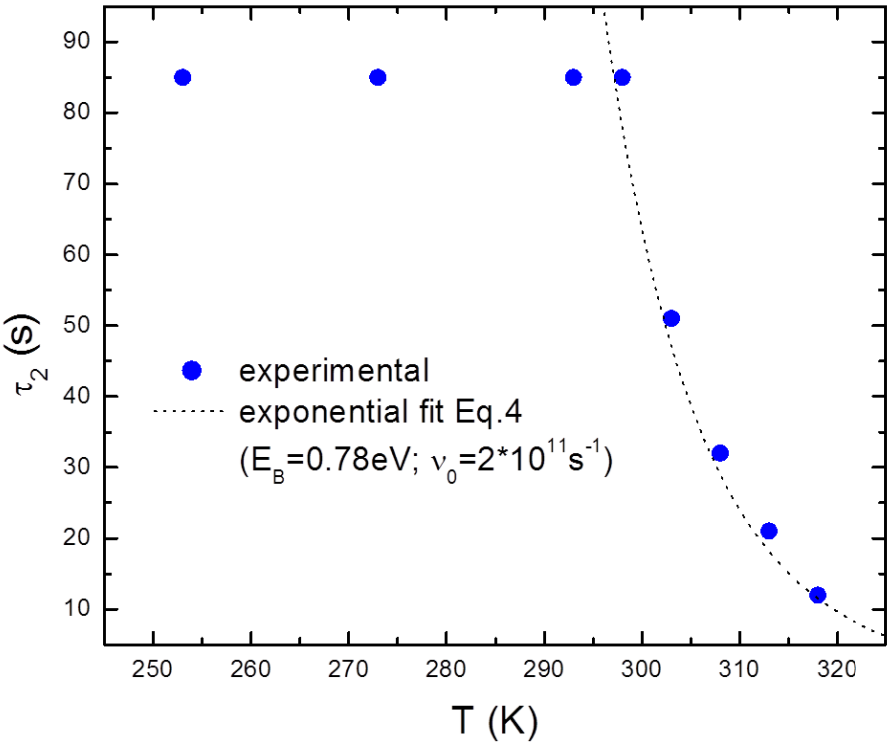

Figure 29. Characteristic relaxation time τ_2 vs. temperature. The dotted curve gives the best fit to Eq.4.

For 405nm excitation, the incident photon energy is high enough to excite electrons from lone-pair (LP) states at the top of the valence band into extended states. Thermalization to the mobility edge produces non-correlated electron-hole pairs (EHPs). Recombination then proceeds by relaxation of the carriers through band tail states, whose density is enhanced under pump excitation by the electronic and strain changes that induce the PD effect. This process involves small steps to progressively lower energies via multi-phonon emission. As a result, one does not expect to observe thermally activated behavior as long as the distortions produced by excitation of the LP-states do not give rise to bond rearrangements. As a result, the system relaxes back to its initial configuration without forming the metastable Y-state proposed in the model of Tanaka

(see Chapter 2). The proposed idea that the formation of non-correlated EHPs does not trigger metastable structural changes is consistent with the model of photo-induced anisotropy (PAN) in chalcogenide glasses presented in Ref.106. In the latter the authors suggest that nongeminate recombination as the result of above-bandgap illumination does not cause structural rearrangements and is not effective in producing photo-induced anisotropy.

In contrast, the co-existence of two characteristics time constants (temperature independent τ_1 and temperature dependent τ_2) for sub-bandgap (655nm) irradiation suggests that we are dealing with an interplay between two mechanisms: *i*) The restoration of the initial ground state by the preceding τ_1 - controlled process, and *ii*) the τ_2 - controlled relaxation of a metastable configuration due to self-trapping of geminate electron-hole pairs in localized band-tail states (e.g. valence alternation pairs (VAPs) and intimate valence-alternation pairs (IVAPs)). The probability of forming such self-trapped excitons is enhanced for band-tail excitation because the absorption transition creates localized geminate electron-hole pairs that are more likely to remain correlated by Coulomb attraction than carriers excited into extended states. Similar considerations have been useful in accounting for the fast-time dynamics of exciton recombination processes in a-Si:H and a-$As_2Se_{3-x}S_x$ [141,142].

The PD relaxation process governed by τ_2, has an intriguing temperature dependence that exhibits thermally activated behavior over a barrier E_B in the narrow temperature range between 25°C and 45°C. By fitting the data in Figure 29 we find that τ_2 obeys the temperature-dependence:

$$\tau_2(T) = \nu_0^{-1} \exp(E_B/k_B T), \qquad (4)$$

where k_B is Boltzmann's constant, and ν_0 is a characteristic attempt-to-escape frequency. The obtained best-fit values are E_B=0.78±0.02eV and ν_0=(3±2)x$10^{11}$$s^{-1}$. These values are quite reasonable. The attempt-to-escape frequency is typical of low-frequency intermolecular vibrations between Se chain fragments in the amorphous matrix, and E_B agrees well with independent estimates of the configuration barrier energy that separates

the ground state X and the metastable state Y in the Tanaka model. These values are also in good agreement with the activation energy found in a-Se for the photo-induced anisotropy effect in the same temperature range [101]. In particular, temperature dependent relaxation kinetics of PAN in a-Se was characterized by Arrhenius law with the activation energy of 0.7eV in the T-region from room temperature to just below the glass transition.

For sub-bandgap excitation, we find that the relaxation of the PD back to the ground-state configuration (i.e, Y to X) at elevated temperatures involves activation over a potential barrier. However, for temperatures below room temperature, this process becomes less efficient, and the observed relaxation of the PD component due to self-trapped excitons requires consideration of configurational tunneling through the Y-X barrier. We note that for $T << T_g$ the PAN in a-Se was proposed to relax by tunneling between mirror-image IVAP configurations whose density can be biased by polarized light [101]. In the latter case, threefold Se atom tunnels into its mirror configuration causing the flip of the IVAP pyramid $C_3^+C_1^-C_2^0C_2^0$ centered at C_3^+ and as such the low-temperature tunneling process takes place with no thermal activation energy required. In our case, for PD the Y-X relaxation is between the extra IVAPs or other defects (of any polarization bias) produced by photo-pumping (Y-state) and the 2-fold Se ground state (X-state). Within this picture, the release of strain for temperatures around the glass transition tends to anneal out the metastable Y configuration, decreasing the energy barrier to this state. As a result, with increasing temperature above T_g the PD relaxation approaches a situation where only its rapid transient τ_1 component is observed.

4.1.2. First-principle simulation of photo-excitation and subsequent relaxation

The first-principle simulation that models our PD experiments with the special attention given to the VAP and IVAP defects was published in Ref. 25. Below we extract the simulation conditions from the reference.

For the study, model compounds of amorphous Se consisting of 25 and 50 atoms are created. For the atomistic simulations, the WIEN2K package [143] with

implementation of the Perdew-Burke-Ernzerhof parametrization of the generalized gradient approximation [144] is used. The optimization procedure is carried out using a minimization of forces for which the product of atomic sphere radius (1.8 bohr centered at the nucleus of the individual atoms) and the plane-wave cutoff in k space is set to 7. The Brillouin zone of a supercell of 25 atoms is covered by the 4 × 4 × 4 Monkhorst-Pack mesh. The size of the Monkhorst-Pack mesh is adjusted to the supercell size; i.e., the mesh is appropriately reduced as the supercell is enlarged. The energy separating the core and valence electrons is set to −6.0 Ry (the cut-off energy is taken by default in WIEN2K package and is found to be satisfactory for the case of a-Se). The force tolerance 0.5 mRy/ bohr in combination with tight convergence limits (energy convergence 0.0001 Ry, force convergence 0.1 mRy/bohr,and charge convergence 0.001e) are applied. To study the fundamental properties of a-Se including the formation of the VAP defects and photo-induced structural transformations, the well-amorphized structure of a-Se placed in a cubic supercell (α =90°, β =90°, γ =90°) and the size of the cubic supercell containing 25 atoms is 8.7 Å×8.7 Å×9.9 Å. Periodic boundary conditions are applied to the supercell. For the simulation of the photo-induced crystallization, a system of increased crystalline order is created, and it is assigned to recognize the symmetry of trigonal Se (t-Se) through application of the hexagonal lattice parameters to the supercell (α =90°, β =90°, γ =120°). In order to ensure that the adjacent replicas of the supercell do not interact, the results achieved for a supercell of 25 atoms is reexamined with a bigger supercell of 50 atoms. The main focus is on the effect of the supercell size on the interaction between the VAP defects (it is known that charged centers are responsible for intercell interactions). It is found that due to the strong localization of the defect states, their intercell interactions are negligibly small. Indeed, the localization length of a photogenerated hole at the VAP defect does not exceed 10Å, as a hole is delocalized over four to five sites only. As such, a localized state at the VAP defect is confined within the boundaries of a supercell of 25 atoms, and supercell enlargement does not affect our simulations.

First, the photoexcitation process of an “ideal” a-Se system (consisting of two-fold coordination Se atoms only) and “real” a-Se system containing VAP defects was carried out [25]. The results demonstrated that sub-band-gap excitation occurs primarily

from the top of the valence band formed by the LP electrons: for an ideal system, an excitation involves the partially charged C_2^- sites, while for the VAP defects, the C_1^- sites are those who participate. Upon excitation, the LP occupancy is reduced by one electron ($LP^2 - e^- \rightarrow LP^1$), and the LP^1 state with an unpaired electron is shifted deeper into the band gap by approximately 0.2 eV due to an alteration in the exchange interaction upon removal of an electron. The LP^1 states are detected experimentally due to a presence of the unpaired electrons [145] and are known to induce the PD effect and are now confirmed by first-principle simulations.

The LP^1 state is delocalized over several sites: calculations show that it involves up to five sites for the two-chain VAP defect. The relaxation of the immediate neighbourhood around the LP^1 state, which is required for its stabilization, is accompanied by the bond shortening or elongation occurring with characteristic energy $\Delta U_{EB} \geq$-0.1eV that corresponds to the B* state (Figure 22). The bond shortening is observed for the IVAP defects (Figure 30(c)).

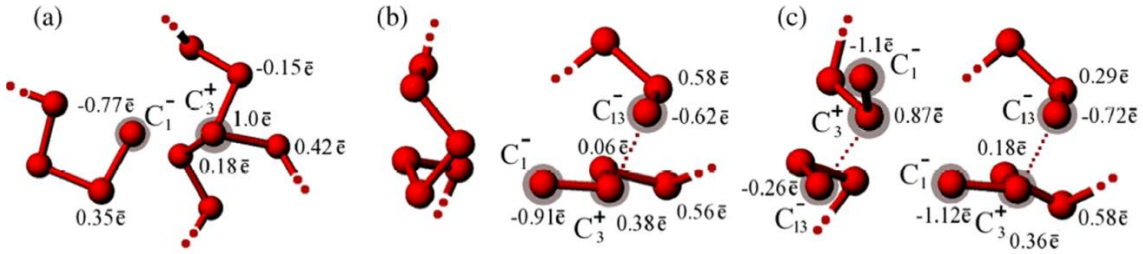

Figure 30. The VAP defects with a distribution of a net charge (a) two-chain VAP defect. (b) Single IVAP defect; the C_3^+ site corresponds to the threefold coordinated site for which the third bond between the C_{13}^- and C_3^+sites is elongated (denoted by the dashed line) due to the strong dipole moment. (c) Pair of IVAP defects; the bond between the C_{13}^- and C_3^+ sites is shortened as the defect dipoles are partially compensated due to defect pairing.

The d($C_{13}^- - C_3^+$) bond shortens by 0.1 Å, which agrees with the previous findings [41]. In contrast, the double-chain VAP defect (Figure 30 (b)) shows a significant increase in distance between the C_3^+ and C_1^- sites by 0.25 Å. Because the double-chain VAP defects should dominate over other defects, an increase in a separation between the C_3^+ and C_1^- sites will govern the volume expansion observed experimentally [146]. Since the bond elongation occurs with the characteristic energy ΔU_{EB}, it is not an immediate process.

Therefore, the volume expansion caused by the LP^1 states at the double-chain VAP defect (Figure 30 (a)) is expected to be delayed from the PD onset, which agrees with the experimental observations [146]. When the missing electron returns ($LP^1 + e^- \rightarrow LP^2$), we find that all systems come back to the original state A (Figure 22). The single-electron excitation described above does not produce any bond rearrangements (causing only either bond elongation or shortening). In order to induce formation of the robust dynamic bond known as the $C_3 - C_3$ defect [42], an excitation of two electrons in the vicinity of a single site is required. This is simulated as a $LP^2 + 2e^- \rightarrow LP^0$ process (LP^0 appears above the LP^1 position in the band gap). Because the excitation of two electrons is unlikely to occur simultaneously, two possible scenarios are considered. *i.* $LP^1 - e^- \rightarrow LP^0$: inequality in the charge distribution generated by LP^1 promotes the excitation of the second electron from the vicinity of the same site. *ii.* $LP^1 + LP^1 \rightarrow LP^0 + LP^2$: two interacting LP^1 states undergo charge exchange. The latter process is feasible when the energy lowering due to the stabilization of the LP^0 state is greater than $2\Delta U_{EB}$ needed to stabilize two interacting LP^1 states.

The double-electron excitation is simulated by the successive removal of two electrons from the system. For an ideal twofold coordinated system and the IVAP pair defect (Figure 30(c)), the significant lattice relaxation with the characteristic energy ΔU_{EC}= -0.9±0.3eV is followed by the bond rearrangements (the C^* state in Figure 22). In an ideal twofold coordinated system, the $C_3 - C_3$ dynamic bond occurs through cross-linking between two chains [42]. The defect state induced by the $C_3 - C_3$ dynamic bond appears close to the midgap. Following lattice relaxation, two unequally populated LP^1 sites formed upon excitation are converted into the LP^0 and LP^2 states; i.e., the charge transfer reaction $LP^1 + LP^1 \rightarrow LP^0 + LP^2$ is initiated since the system meets the requirement $|\Delta U_{EC}| > 2|\Delta U_{EB}|$. For the IVAP pair defect, the double excitation is found to induce bond rearrangements followed by the formation of the single C_3 defect with three equivalent bonds of 2.4–2.5 Å in length (the defect state appears closer to the conduction band). To reach the final configuration, the lattice relaxation requires overcoming the potential barrier ΔV_B ~ 0.8eV. It correlates well with the potential diagram presented in Figure 22 for the $A^* \rightarrow C^*$ transition as well as it perfectly matches

the experimental results for τ_2, demonstrated in 4.1.1 subsection of this Chapter. Interestingly, an amorphous network can be resistant to the double-electron excitation if destabilization induced by a hole localized in the valence band tails is not enough to overcome the potential barrier ΔV_B. This is exactly the case for the two-chain VAP and single IVAP defects for which the B^* states with characteristic relaxation energy $\Delta U_{EB} \geq$-0.1eV occur.

When the two missing electrons are returned into the system, the C^* state becomes unstable, and its stabilization requires breaking the dynamic or other bonds that depend on whether or not the dynamic bond is strongly stabilized at the excited state. The process of bond breaking and switching in the post-excitation regime occurs with the characteristic energy -0.9±0.3eV, which is similar to ΔU_{EC}. In this case, the final configuration is different from the original ground state A (Figure 22) and is not necessarily the lowest in energy. The ideal system is converted into a system that contains a Se_7 ring, and the decrease in the total energy compared with the initial configuration is found to be -0.49eV. The IVAP pair (Figure 30(c)) is converted into the double-chain VAP defect (Figure 30 (a)) accompanied by a lowering in energy by -0.28eV. The achieved decrease in energy in both cases is larger than what the ringlike to helixlike transformations can provide (approximately -0.025eV per atom [47]). This explains the predominant formation of the equilibrium centers such as the VAP defects upon excitation of the LP electrons.

In addition, the simulation results show that ring-like to chain-like transformations require a nucleation embryo, which is needed to recognize the symmetry of t-Se and, as such, facilitate chain straightening. To confirm this, double-electron excitation is simulated in a system with increased crystalline order (Figure 31). It is found to induce formation of the standard $C_3 - C_3$ defect followed by chain straightening (see the excited state in Figure 31), i.e. by ring-like to chain-like transformations. Because of the increased crystalline order of the initial system, the characteristic energies describing lattice relaxation during excitation ΔU_{EC}= -0.5±0.3eV are lower than that in the well-amorphized system.

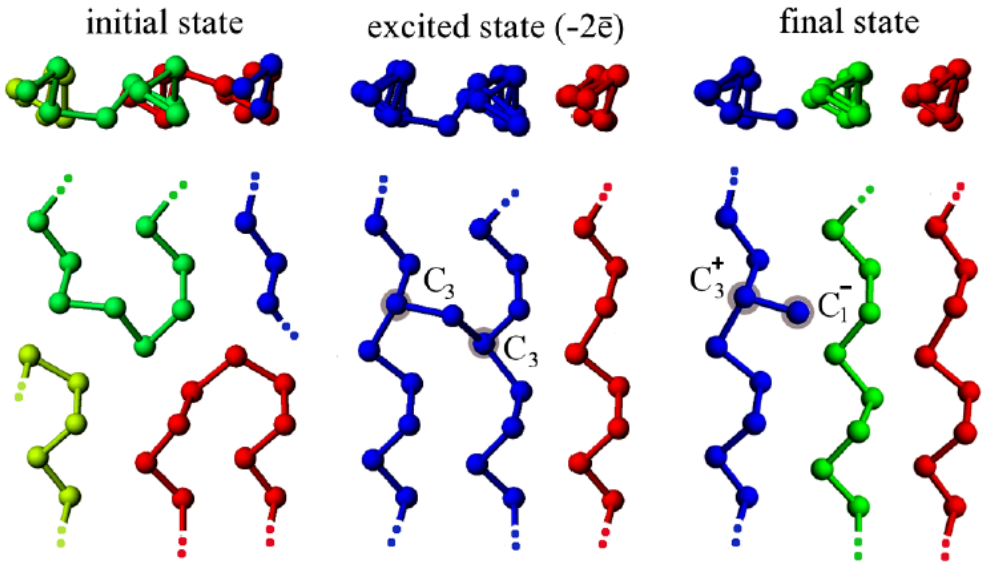

Figure 31. Photoinduced crystallization of the increased crystalline order system. The final state is t-Se containing the IVAP defect.

In the postexcitation regime, the system with increased crystalline order completely converts to trigonal Se. A decrease in the total energy due to photocrystallization is found to be -0.08eV, which agrees with the gain in energy provided by the ring-like to chain-like transformations involving up to five atoms (approximately -0.025eV per atom). Therefore, we suggest that experimentally observed crystallization of the a-Se samples under sub-bandgap illumination [22, 122] should be linked to the double-electron excitation process.

The PD kinetics in a wide T-range with the characteristic times of relaxation τ_1 and τ_2 (Figure 26) verifies both single- and double- electron excitations. The difference in the τ_1 and τ_2 behaviors indicates that the relaxation of PD involves two distinct processes: one that has the lattice relaxation in its origin and requires activation over a potential barrier with characteristic time τ_2, and another process which does not involve the lattice relaxation and occurs much faster with τ_1. The remarkable similarities between the magnitude of the activation energy E_B=0.78±0.02eV are found in the PD experiment and ΔU_{EC}= -0.9±0.3eV required for the bond rearrangements leads us to believe that the slow PD component (characterized by τ_2 at elevated temperatures) describes the process of structural relaxation with the bond rearrangements. Therefore, the feasibility of

double-electron excitation process accompanied by the formation of the LP^0 states is confirmed by the slow component of the PD relaxation.

In contrast, the temperature independence of the fast component (τ_1 is about 2.5s) is a direct evidence of the relaxation process that does not involve bond rearrangements. It is consistent with very weak lattice relaxation $\Delta U_{EB} \geq$ -0.1eV involved in the stabilization of the LP^1 states generated by the single-electron excitation.

4.1.3. Conclusion

In conclusion, our study demonstrates two essentially different mechanisms involved in the relaxation of PD in a-Se for the cases of above-bandgap and sub-bandgap illumination. We provide experimental evidence that for above-bandgap excitation only transient PD is observed: the relaxation time constant is short and found to be temperature independent in a wide temperature range. This suggests that above-bandgap excitation does not cause the formation of self-trapped excitons [98], and so does not lead to occupation of metastable Y-states [22, 99]. Consequently, relaxation to the initial ground state (X configuration) does not require substantial bond rearrangement, otherwise thermal activation would be involved. Instead, recombination can occur by relaxation of carriers through the band tails to lower energy states reached by multi-phonon emission, restoring the ground state configuration. As the result it does not trigger a transformation to the crystalline state. In contrast, sub-bandgap excitation causes both transient and metastable PD, the latter relaxing with a comparatively long characteristic time constant. The quantitative analysis of the temperature dependence of this time constant suggests that the reversible PD is controlled by the formation of self-trapped excitons whose relaxation requires overcoming an energy barrier of 0.78±0.02eV either by thermal activation (at elevated temperatures) or by configurational tunneling (for temperatures below RT). In addition, self-trapped excitons act as a precursor for either VAP or IVAP states that once agglomerate can cause a collapse to the crystalline phase.

Further, the first-principles simulation results suggest that on a microscopic level two distinct mechanisms of photoexcitation, namely single-electron and double-electron

excitation can cause transient and metastable PD respectively. The excitation of a single electron from LP^2 leaves behind an unpaired electron and shifts the nonbonding LP^1 state towards the midgap, thus, inducing the photodarkening effect. This process manifests itself in the fast component of the relaxation of the photodarkening which is characterized by a short and temperature independent characteristic time constant τ_1= 2.5s. The fact that τ_1 is temperature independent suggests that no bond rearrangement is involved in lattice relaxation. We find that to trigger structural transformation in an a-Se network, excitation of two electrons from the vicinity of the same LP site is required. The characteristic energy of the lattice relaxation following the formation of the $C_3 - C_3$ defect is calculated to be ΔU_{EC}= -0.9±0.3eV. This process is reflected in the slower component of the PD relaxation described by temperature-dependent time constant τ_2=85s yielding the activation energy E_B=0.78±0.02eV. The similarity between the characteristic energy ΔU_{EC}, which describes lattice transformation, and the activation energy E_B in the PD kinetics, suggests an identical origin. In addition, application of the double-electron excitation to a system of increased crystalline order is found to induce photocrystallization. This agrees well with previous findings of the respective barriers of the irreversible PD and PC [122].

4.2. Photocrystallization in a-Se layers

The following subsection is from our publication in the Journal of Applied Physics 116, 2014 (Ref. 124).

To study the strain and thermal effects on PC in great detail we employ co-localized Raman mapping and atomic-force microscopy (AFM), Raman spectroscopy, and optical microscopy to probe the spatial profile of *PC-spots* (crystallized spots created by laser exposure) and the temperature dependence of the PC onset time in a-Se films deposited on glass and Si substrates with or without intermediate coatings of indium-tin oxide (ITO) and/or polyimide (see Appendix A for samples details).

4.2.1. Spatial mapping of PC profiles

Figure 32 shows optical micrographs, taken in transmission and reflection, of PC-spots produced in two different samples, both having the film structure a-Se/ITO/glass. In Figure 32(a) the microscope is focused on the sample's top surface (i.e., the a-Se-air surface). The left-hand (LH) and right-hand (RH) spots are created by exposing the film to focused laser light directly through the glass substrate and through the film's top surface, respectively. Both exposures give the same spot morphology, an oval shape on the top surface and "wing" like lateral shadows that extend up from the a-Se film's bottom surface (i.e., the a-Se/ITO interface). This morphology is confirmed by the reflection micrographs in Figure 32(b) and Figure 32(c), recorded, respectively, for the RH spot in Figure 32(a) and for a PC-spot produced in another a-Se/ITO/glass sample.

Additional examination of the latter spot under transmitted light at low and high magnification (Figure 32(d) and Figure 32(e)) reveals individual t-Se domains. Previous work has shown that these domains are generally in the shape of pyramidal cylindrites [110,111,112,113,114,147], with the apex growing toward the top surface of the a-Se film and the base at the films bottom surface (*i.e.*, here, the a-Se/ITO interface). The driving mechanism for this geometry is thought to be substrate-induced strain transmitted to the Se layer, which causes the lateral growth of t-Se near the substrate to be faster than the growth normal to the substrate. The shapes of the crystallites in Figure 32(e) are consistent with this habit of growth.

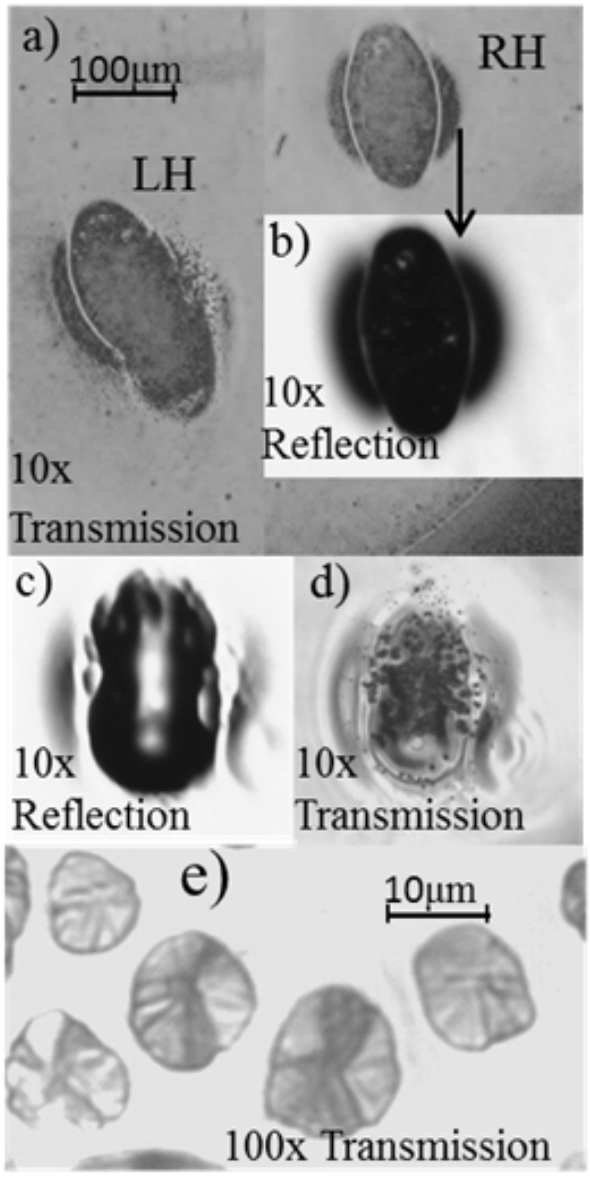

Figure 32. Microphotographs of PC-spots in two a-Se/ITO/Glass samples: a)spots created by laser-light incident on the glass (LH) and film (RH) sides; b) reflection image of RH spot; c) and d) analogous images of a PC-spot in another a-Se/ITO/Glass sample; and e) high-power view of t-Se cylindrites in latter spot.

In Figure 33 we show a Raman mapping profile of a PC-spot in a film of a-Se deposited on a device-grade silicon substrate. This profile charts the intensities of the a-Se and t-Se A1 Raman modes as a function of the surface position of the probing laser.

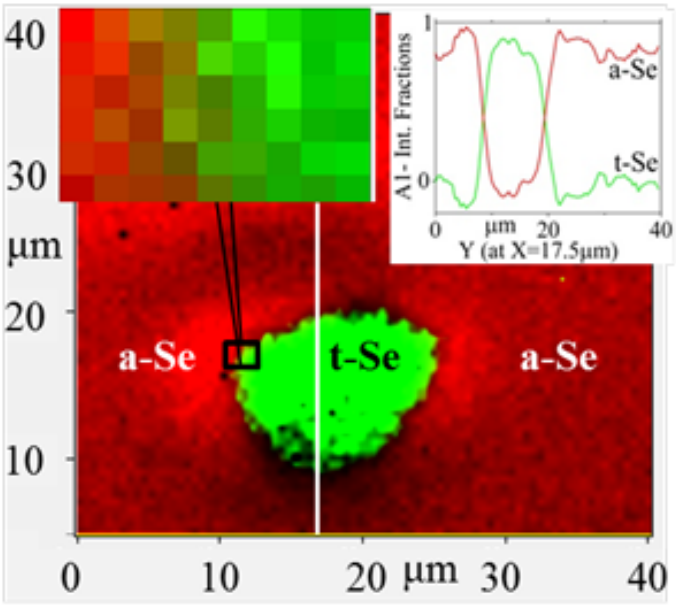

Figure 33. Raman map of PC-spot in an a-Se film on Si, profiling the intensities of the t-Se (green) and a-Se (red) Raman peaks. RH inset shows a y-axis scan at x=17.5µm (white line) giving the fraction of the total intensity contributed by each peak. LH inset is a blow-up of a-Se/t-Se boundary. Probing laser was focused at the film-air interface.

A typical scan across the center of the spot, showing the fractional contributions of each peak to the total intensity, is illustrated in the RH inset. The central region is strongly dominated by the t-Se peak (at 237 cm^{-1}), whereas around the spot the a-Se peak (at 256 cm^{-1}) becomes dominant. The boundary region of mixed a-Se and t-Se is ~2 µm wide (LH inset). The Raman intensities indicate that the central volume under the laser spot contains ≳ 90% t-Se. A co-localized AFM map of the same PC-spot (Figure 34) reveals the areal and depth topologies in greater detail. Figure 34(a) and (b) show three dimensional views of the spot from two different angles. Figure 34(c) is a cut away showing the height difference across the center of the spot. There are two depressions surrounding the oval shaped raised center. Comparing to the Raman map in Figure 33, we establish that the raised region consists mainly of t-Se (≳ 90% within the dashed circles), and the fraction of a-Se in the depressions increases rapidly as one moves outward. The total change in height is ~3 µm. The PC results in this a-Se/Si sample suggest that a focused laser beam incident through the film tends to draw the growth of t-Se domains

toward the film surface. Shear stress due to laser-tweezing, and local heating, are two factors that may promote this behavior in the presence of a tightly focused pump beam. The depth profile most likely reflects the reaction of the film to the 12% density increase in the central t-Se component compared to the density of the surrounding a-Se. As PC initiates and crystallites grow and agglomerate to saturation under the focused laser beam, this density increase causes an anisotropic growth-induced material flow that acts to pull Se in from the surrounding matrix. The radial asymmetry in the spot is probably due to light polarization effects [116,148].

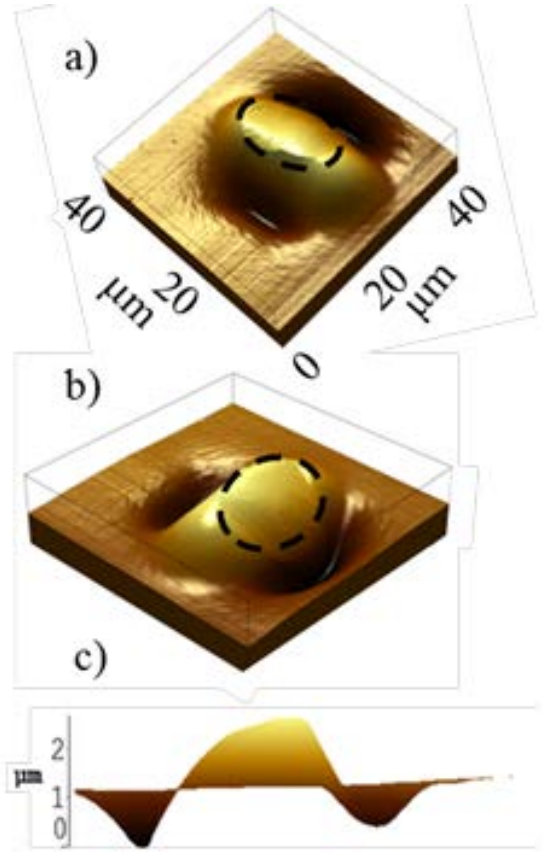

Figure 34. AFM maps of same PC-spot shown in Figure 33(a) and (b) 3d-views from two angles; dashed black circles outline t-Se high-content region in Figure 33(c) Depth profile across spot center.

Figure 35 is a schematic representation of the change in film morphology observed in the Raman and AFM maps of Figure 33 and Figure 34.

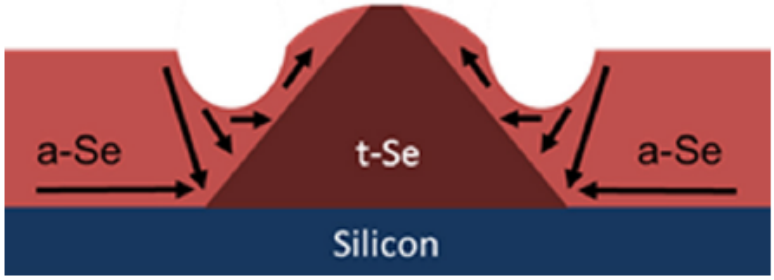

Figure 35. Model of change in morphology under the focused laser spot for saturated growth of PC in an a-Se film on a rigid Si substrate. A boundary through forms due to the density increase in t-Se.

Figure 36 documents an attempt to create PC in an early a-Se/ITO/glass film that was shelf-aged for two years under room light conditions. This film showed signs of appreciable changes including flaking, areas that had crystalized, as well as regions that were still amorphous, as confirmed by low-power Raman mapping. We found it difficult to induce PC in the a-Se regions of this sample without also producing physical damage, in contrast to our results on the other samples (which were not older than 4 months). The AFM profile in Figure 36(a) shows a raised spot created by a 0.5μW/μm^2 flux of 671nm light. A Raman map of the 10μm^2 area centered on the swelling detects only a-Se in the entire square (Figure 36(b) map and insert). Subsequently another AFM scan of this square (Figure 36(c)) reveals that wherever the probing laser has been incident, the a-Se film becomes raised by ~0.5 μm without being crystallized and without forming sunken regions. The most likely explanation is that film-substrate adhesion has degraded in this film during its two year storage. This might happen through changes in the a-Se network that favor photo-expansion instead of PC, as is sometimes found [149,150]. If the film-substrate adhesion degrades, the substrate strain which tends to promote PC is weakened, consistent with the observed difficulty in crystallizing this film.

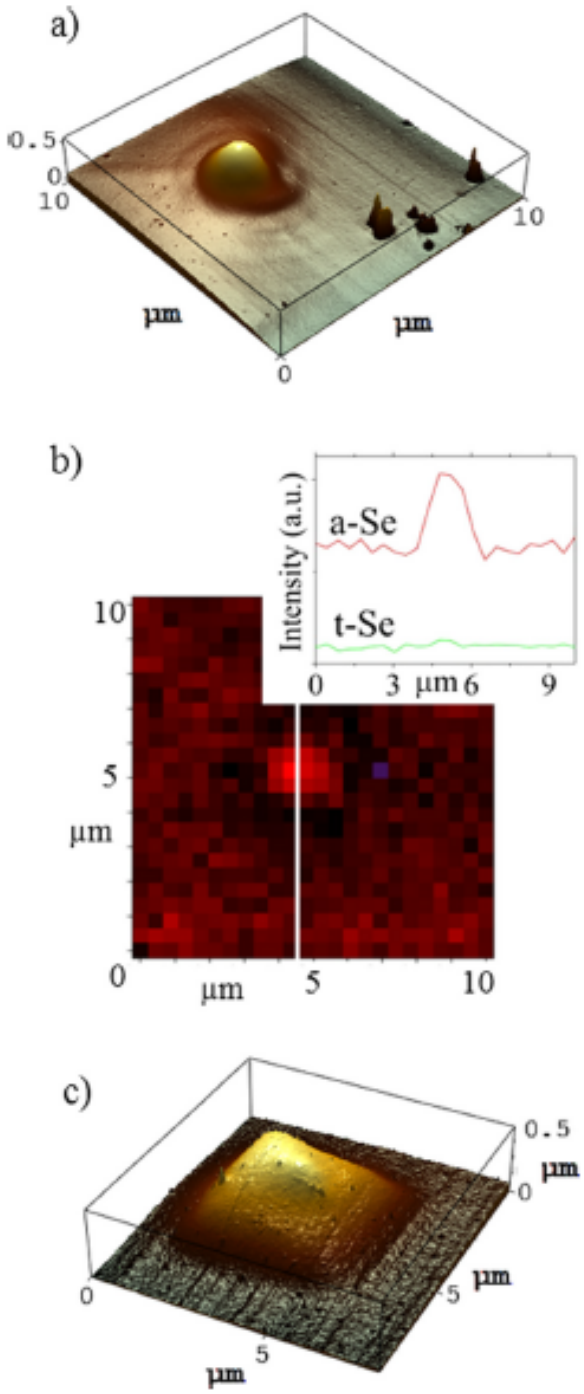

Figure 36. Results of attempt to produce PC in an aged a-Se/ITO/Glass sample. (a) 3d-AFM profile of a laser-induced spot; (b) Raman map of 10µm^2 area around spot. Only a-Se (in red) is found. Inset is y-axis scan at x=4.2µm of a-Se and t-Se A1 intensities; (c) 3d-AFM map of subsequent swelling in a-Se phase caused by Raman probe.

Besides the aged a-Se/ITO/glass film just discussed, we find that freshly grown structures containing a polyimide layer between the a-Se and the substrate exhibit greatly enhanced stability against PC. In fact, our Raman spectroscopy results on a-Se/polyimide/glass and the a-Se/polyimide/ITO/glass samples observe no onset of PC whatsoever in the temperature range investigated, 280K - 345K. Weak adhesion is again a possibility. We however, discount this since these samples exhibited good electronic response in feasibility tests for photo-sensor applications [151]. Rather we attribute the observed stabilization against PC to the mechanical softness of the polyimide layer, which is able to buffer the a-Se from the effects of substrate strain.

4.2.2. Temperature dependence of PC onset

The onset-time of PC in the a-Se films is determined by monitoring changes in the Raman spectrum. A reference Raman line-shape is established for a given location on the film by fitting the Raman spectrum recorded on initial ($\leq$ 5min.) laser exposure at that spot. We assume this line-shape reflects the zero-time state of the film, and has no (or minimal) t-Se component. This reference is subtracted from each subsequent spectrum after scaling to match the observed height of the a-Se A1 peak. As the PC progresses, this difference of spectra gives a peak at 237cm^{-1}, whose intensity reflects the amount of t-Se that is present under the laser spot. The onset of PC is taken as the minimum laser-exposure time for this intensity to exceed twice the RMS noise in the measured spectra.

Figure 37 compares the observed onset time for PC as a function of temperature in three films. The error bars reflect the uncertainty that result from a ±25% variation of the RMS spectral noise. In Figure 37 (a) and (b) the film structures are 16 μm a-Se on ITO/glass, and in Figure 37(c) the structure is 16 μm a-Se on uncoated glass. The onset times for the latter film do not exceed 30 min., which is short compared to those found for the films grown on ITO/glass (up to 400min.) This indicates that films deposited on plain glass substrates are more prone to PC than those deposited on ITO-coated glass substrates.

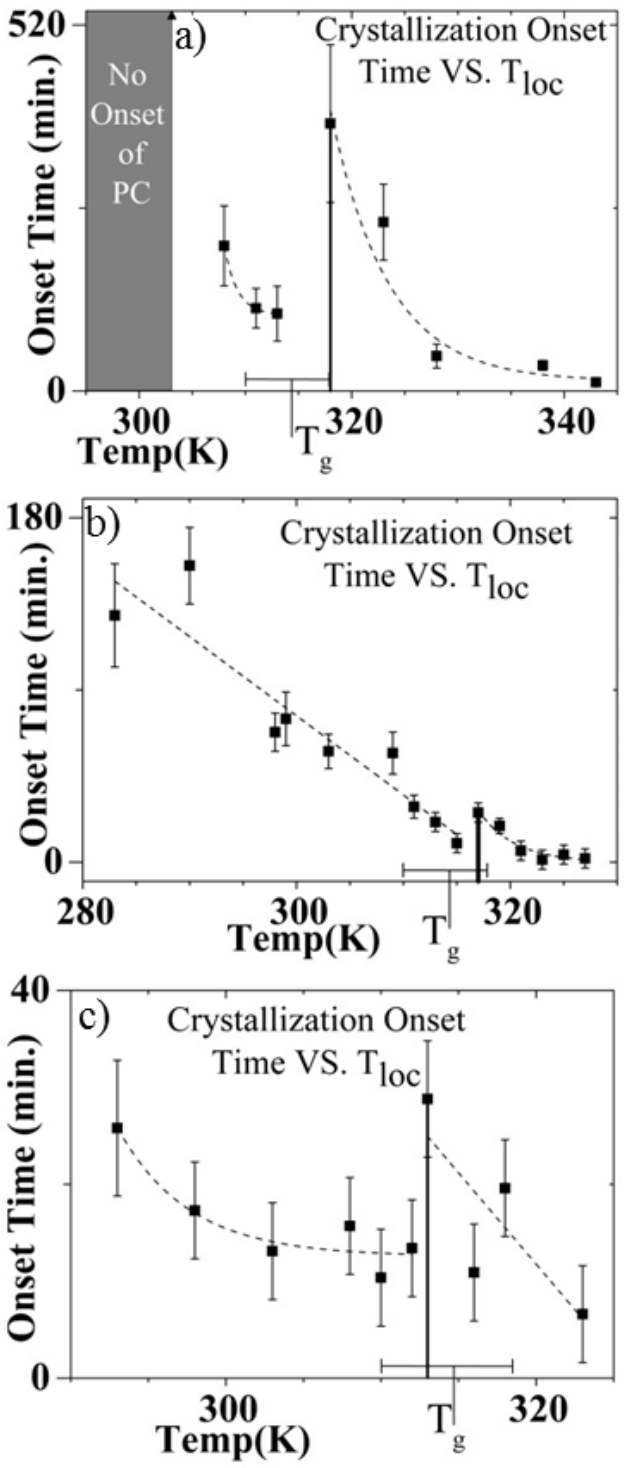

Figure 37. Comparison of the effect of T on the Raman-observed PC onset times in (a) an a-Se/ITO/Glass sample, (b) a similar sample fabricated in a different laboratory, and (c) an a-Se/Glass sample. Note jump in the onset time on heating through T_g in each sample. Data in (a) and (c) are taken from prior experiments after revised analysis by the more accurate method described in the text.

The results in Figure 37 reveal that a discontinuous increase in the PC onset-time occurs with increasing temperature near the a-Se glass transition (T_g ~313K). At other temperatures the expected behavior is seen – shorter onset-times at higher temperatures. The discontinuities, which are ~300min. in Figure 37(a) and ~15min. in Figure 37(b) and (c), exceed the uncertainty in each case, although the Figure 37(c) result is perhaps borderline. This variation of the jump in PC onset-time near T_g for different glass-deposited a-Se film structures is consistent with the preliminary results in Ref 121.

The discontinuities in the PC onset-time as a function of temperature strongly indicate that the PC growth kinetics are mediated by competing mechanisms near to the a-Se glass transition. This was suggested in Ref. 46 to explain the HARP target results, and the present findings provide further confirmation for a more diverse range of a-Se film samples. The competing mechanisms can be understood in terms of a model proposed by Stephens [114], which will be discussed further in the next section. We point out that some of the observed differences in the PC behavior of our a-Se films may be due to their preparation in different laboratories with different surface cleaning procedures prior to a-Se deposition. However, our results for both the mapping and onset-time experiments provide convincing evidence that the rigidity of the interface between an a-Se film and its substrate can mediate the onset of PC.

4.2.3. Discussion and summary

Our experiments on PC in a-Se films reveal a number of interesting substrate-related effects that operate via complex mechanisms. The underlying physics however, is straightforward, and it is instructive to present a brief summary.

At the atomic scale, PC in a-Se proceeds by bonding-defect reactions, in which the chain fragments and rings of the a-Se matrix linkup to form the ordered t-Se structure – triad spiral c-axis-chains set on a hexagonal basal array [105, 109]. The defect configurations of the Se lone-pair electrons are generally thought to mediate these reactions. The bond changes enable the nucleation of t-Se embryos large enough (~few

nm) to sustain further growth [113], and also act at the t-Se/a-Se interface to drive the secondary growth to μm-size t-Se domains.

The Stephens model [114] addresses the secondary growth process. It treats a-Se as a disordered array of polymer chain segments and 8-fold rings (~4%) [152], in which the mean number $\bar{P}$ of Se_8 units in the chain segments depends on temperature and internal stress. A thermodynamic approach [153] is used that does not require knowledge of the specific defect reactions. The internal stress arises from the 12% density increase in t-Se relative to a-Se. The stress is tensile in the a-Se matrix around a t-Se domain, and for good adhesion the stress is enhanced near a rigid substrate by the latter's stiffness. Additional chain segments link to the t-Se domains by a processes that involves viscous flow or chain-end rotation (vector connecting the chain end can rotate), and a smaller $\bar{P}$ increases the probability for segments to find geometries that favor t-Se. The kinetic energy needed to drive these bonding changes can be supplied by temperature and/or photons. The tensile stress around a t-Se domain acts to decrease $\bar{P}$ in the nearby a-Se matrix, and so provides another driving potential for t-Se growth according to [114],

$$\bar{P} \sim \left[\frac{M_o K' - 1}{K} \right]^{1/2} \exp\left(\frac{-\sigma_e \Delta V}{2kT} \right) \qquad (5)$$

The effective hydrostatic portion of the stress is σ_e, ΔV is the local volume increase on creating two chain ends, K and K' are T-dependent rate constants, and M_o is the density of Se_8 units. Similar thermodynamic considerations could be applied to calculate $\bar{P}$ for more recent structural models, in which, *e.g.,* a-Se is viewed as a collection of chain fragments with a balance of t-Se-like and ring-Se-like second nearest neighbor configurations [154]. The Raman detection limit is such that the onset time observed here should correspond to ~1-2% t-Se in the film-volume under the laser beam. For temperatures $T < T_g$ the film is rigid and can support σ_e. At the t-Se/a-Se boundary of a domain that lies near the substrate, $\bar{P}$ is decreased by σ_e, thereby promoting t-Se growth. As T is raised, thermal energy drives the growth faster. We observe shorter onset times, providing the a-Se matrix continues to support σ_e. This drastically changes at the glass

transition with softening of the a-Se matrix. The resulting decrease in σ_e *competes* with increasing T for the overall effect on $\bar{P}$. One expects a sudden increase in the onset time as T is raised from below to above T_g, in agreement with our findings. At still higher temperatures the effect of σ_e vanishes. Crystallization becomes primarily a thermally driven process that is only assisted by light. The onset time for crystallization should again fall, as is observed.

Our results for the two a-Se film structures that contain a soft intermediate layer of polyimide, and for the film with degraded adhesion, support the validity of this model, since the rigidity of the film-substrate interface is greatly reduced in these samples. In particular, the former samples show that it is possible to exploit the use of intermediate polymer layers to control the transmission of strain from a substrate into an a-Se film device. There are many applications where this is desirable. Here it is employed to stabilize the a-Se against PC while preserving the electrical contact characteristics needed for a device to operate as a sensitive photodetector [155].

To summarize this subsection, Raman scattering, AFM, and optical microscopy were used to investigate PC in a-Se film structures deposited on glass and Si substrates with or without intermediate ITO and/or polyimide coatings, in geometries of technological interest. We study the occurrence, growth morphology, and onset time of the PC in a-Se for different film-substrate interfaces, and for temperatures that span the glass transition. Our AFM profiles show a distinct trough around PC-spots, reflecting the action of tensile strain arising from the 12% densification in t-Se regions. The temperature dependence of the PC onset time near T_g ($\pm$3K) exhibits discontinuity in which a small rise in temperature causes a slower onset of PC. Thus, there is a temperature regime in which supplying more thermal energy has the counter-intuitive effect of enhancing stability against PC. Our results demonstrate the generality of this effect for films subject to strain from a rigid film-substrate interface. In contrast, we find that no PC occurs in three samples where either weak adhesion, or a soft polyimide intermediate layer, relieves this interface-strain. Our results are in accord with the theory of Ref. [114] for PC in a-Se films, a polymerization model that has been successful in explaining the ability of tensile strain to promote PC. Competition between the effects of

strain and temperature as the a-Se softens on heating above T_g causes the discontinuity in the PC onset time. The problematic occurrence of PC in a-Se film devices might be avoided by engineering structures without a rigid film-substrate interface – as is found here by introducing a soft polyimide layer at the interface region. Further investigations along these lines should be undertaken.

CHAPTER 5

Photodarkening and Photobleaching in a-Ge_xSe_{100-x}

The microscopic nature of the light-induced effects in a-Ge_xSe_{100-x}, i.e. photodarkening and photobleaching, is revealed across the glass-forming region, with a special emphasis on high-rigidity transition (x≈30%). The study is carried out by combining optical and structural analysis and first-principles simulations. Transient and metastable photodarkening and photobleaching kinetics are first recorded on the time-scale of seconds by means of a two-laser beam technique for various Ge-content films (x=29.2%, 32.1% and 39.5%). Then direct confirmation of structural transformations is performed by Raman analysis. First principle simulations are employed to provide fundamental insights into the changes associated with photo-excitation and subsequent relaxation processes .

This study has been published in Optical Materials Express 5(2), 2015 (Ref.82), and the sections below are extracted from it.

5.1. Experimental results on two-laser beam technique combined with Raman analysis

For the experimental study, amorphous Ge_xSe_{100-x} films with various compositions, x=29.2%, 32.1% and 39.5% deposited onto ITO-coated glass substrates from a previously synthesized ChGs are used (for sample preparation details refer to Appendix A). Experimental data on optical transmission changes is acquired using apparatus described in section 3.1. Figure 38 presents the results obtained with the two-laser beam technique. Distinctly different photo-induced effects are observed for a-Ge_xSe_{100-x} glasses depending on the compositional variation.

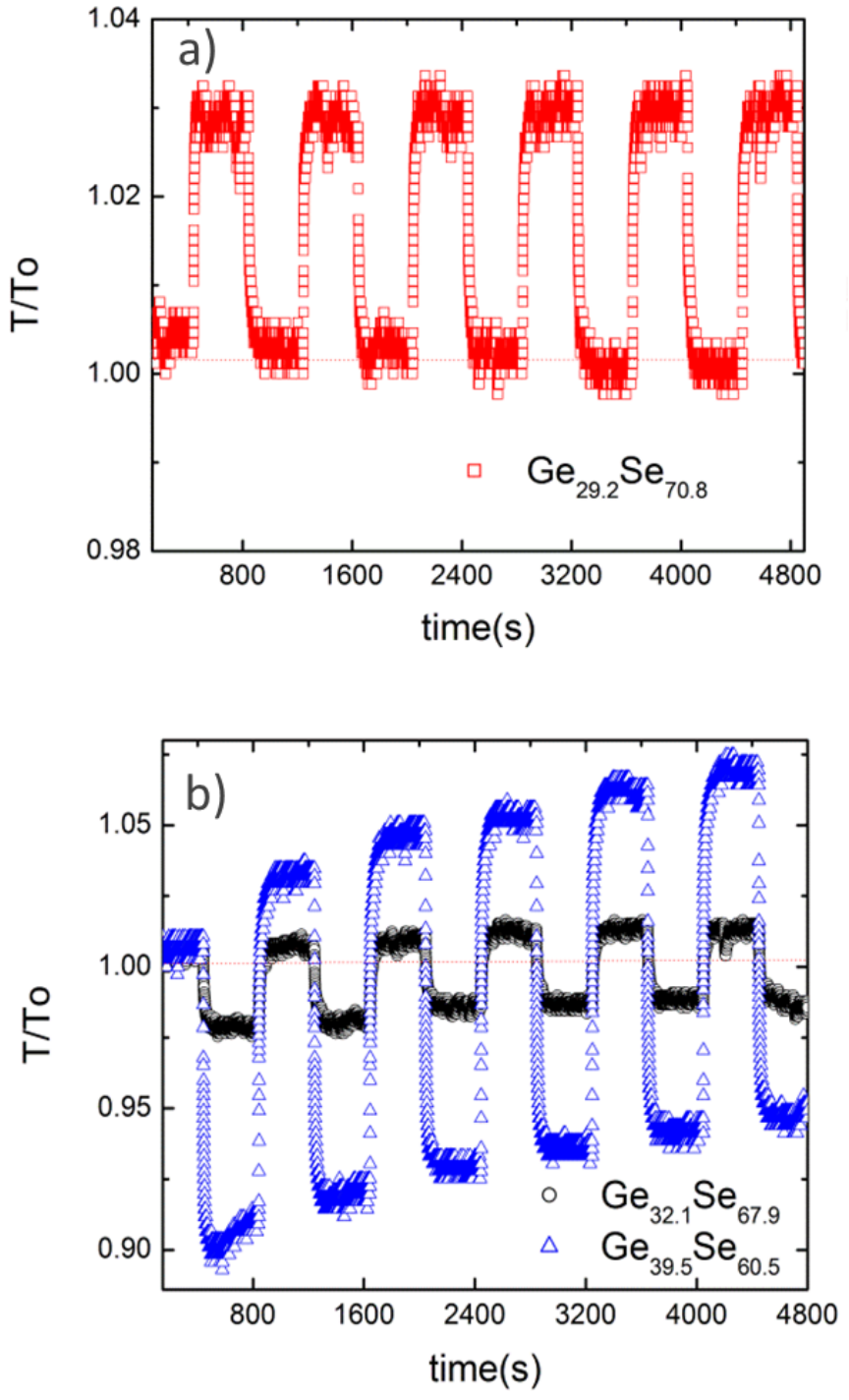

Figure 38. Time evolution of (a) $Ge_{29.2}Se_{70.8}$ film transparency shows transient PB; (b) $Ge_{32.1}Se_{67.9}$ and $Ge_{39.5}Se_{60.5}$ demonstrate mixture of: transient PD (during pump cycle) and metastable PB (during rest period).

A concentration of Ge $x \approx 30\%$ is found to be critical. Below this content, i.e. for $x=29.2\%$, only a transient effect is present. Above this content, i.e. for $x=32.1\%$ and $x=39.5\%$, metastable effects emerge. Thereby, when $Ge_{29.2}Se_{70.8}$ is illuminated with a pump beam for 400s, its relative transmittance rapidly increases by 3% and saturates (Figure 38 (a)). During the follow up 400s rest period, the effect disappears completely. Even on repeating on/off cycles, this tendency remains unchanged and exceptionally transient PB is seen.

When the critical concentration of Ge is exceeded, both transient photodarkening (during the pump period) and metastable photobleaching (during the rest period) are observed (Figure 38(b)). Moreover, the higher the Ge content, the more pronounced the magnitude of both the transient and metastable changes. In case of $Ge_{32.1}Se_{67.9}$, a decrease in transmittance of 2.5% is observed upon light irradiation (Figure 38(b), black circles). Once the film is allowed to rest, the quick rise of the film transparency that continues to increase gradually leads to a metastable PB effect. In subsequent "on/off" series, transient photodarkening is followed by build-up of metastable photobleaching, with enhanced amplitude of the PB during each next resting cycle. Consequently, at the end of the experiment, an overall bleached film is produced with transparency of 1.5% above its initial level. Furthermore, an identical trend of crossover from transient PD to metastable PB is seen for $Ge_{39.5}Se_{60.5}$ composition, with a much more pronounced effect (Figure 38(b), blue triangles). Overall metastable PB reaches ~7% over the initial level of transmittance for the $x=39.5\%$ Ge-Se compound.

Subsequent comparative Raman analysis of as-deposited with light-exposed films reveals the following: (1) for $Ge_{29.2}Se_{70.8}$, no changes within an error in the ES:CS ratio are observed and (2) the amount of the Se-Se and ETH-type bonding remains constant with illumination time (Figure 39 (a)). No change between the Raman spectra of virgin and light-illuminated spectra for the composition of $Ge_{29.2}Se_{70.8}$, showing no bond rearrangement (for which only transient PB has been seen on the optical transmission spectra as a function of time (Figure 38(a)). The Raman results for the films with composition $Ge_{32.1}Se_{67.9}$ suggest marginal changes in the structural organization of this film as a result of the light interaction; this is in good agreement with the optically recorded data, implying weakly mixed PD and PB effects (Figure 38(b)).

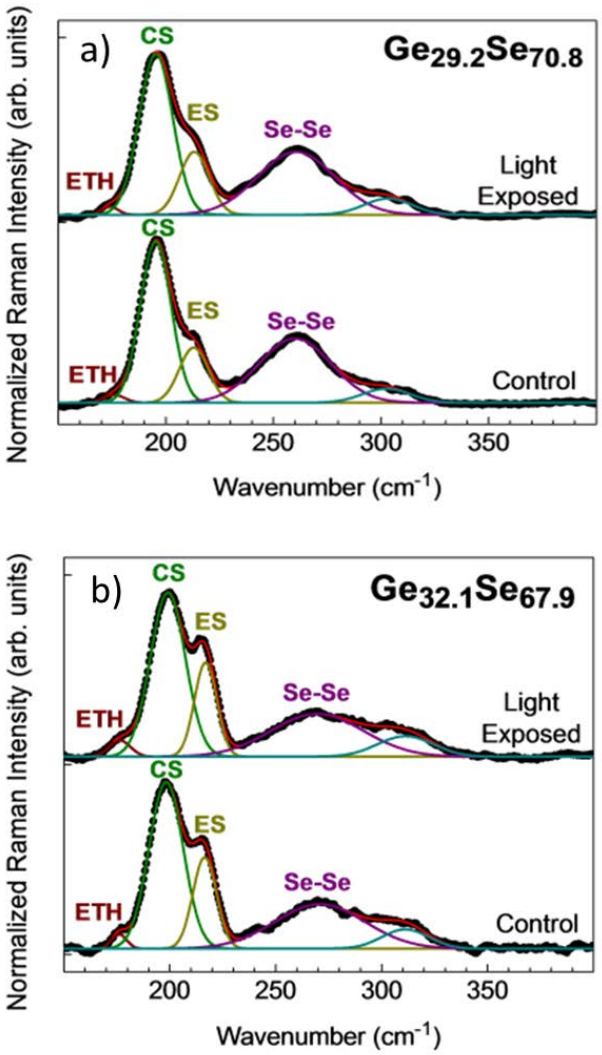

Figure 39. Raman spectra of the virgin and post-illuminated films with the following compositions: (a) $Ge_{29.2}Se_{70.8}$ and (b) $Ge_{32.1}Se_{67.9}$.

In contrast, significant changes in Raman spectra are observed in Figure 40 between post-exposed and pre-exposed, $Ge_{39.5}Se_{60.5}$ film. This can be related to the occurrence of a metastable PB that has been observed experimentally (Figure 38(b)). According to Raman analysis, the ES:CS ratio increases from 0.42 to 0.91. The concentration of ETH and Se-Se structures decreases from 9.8 to 7.9 and from 14.6 to 10.2, respectively (Figure 40 and Figure 41).

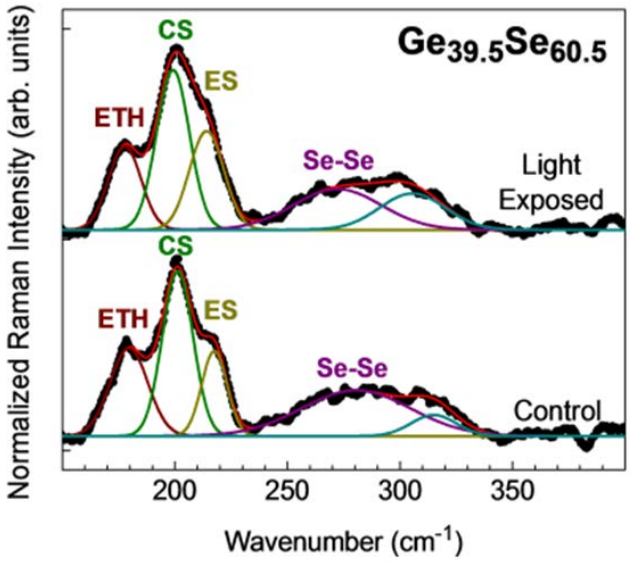

Figure 40. Raman spectra of the virgin and post-illuminated $Ge_{39.5}Se_{60.5}$.

The increase in ES:CS ratio, together with simultaneous decrease in ETH and Se-Se structures, suggest that a large quantity of Ge-Ge bonds and Se-Se bonds are broken and converted (predominantly to ES tetrahedral units) as a result of relaxation in the post-light-exposed period. The reversibility of the PB effect also supports the hypothesis that its nature is mainly a function of structural reorganization and not of oxidation. Figure 41 presents the extracted data from the Raman spectra of the studied films, related to the quantitative evolution of the areal intensity of the structural units represented in the studied films.

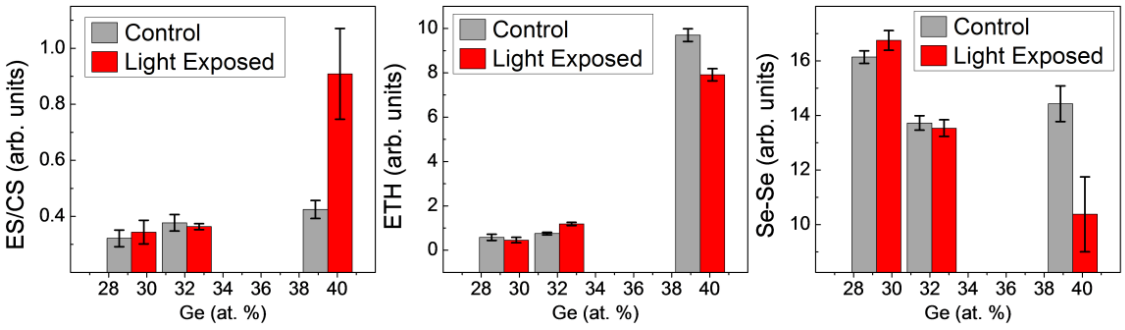

Figure 41. Observed structural changes in $Ge_{29.2}Se_{70.8}$, $Ge_{32.1}Se_{67.9}$ and $Ge_{39.5}Se_{60.5}$ films before and after light exposure, as determined through integration of deconvoluted bands in Raman spectra with curve-fitting error: (a) ES/CS ratio; (b) ETH bonds; (c) Se-Se.

5.2.First-principles simulation results and Discussion

The following section deals with the structural interpretation of the physical properties of the a-Ge_xSe_{100-x} class of glasses, with a focus on the implications of the compositional variation over the studied effects. We attempt to connect the experimentally observed light-induced transmittance changes (Figure 38) with the structural transformations evident from Raman analysis and the first-principal simulations. Based on the appearance of a metastable photo-induced effect in a-Ge_xSe_{100-x} films, this section is divided into two parts: films containing Ge below x=30% and films containing Ge above x=30%. Following the classification suggested in Boolchand et al. [66], there is a threshold in the Raman signatures of the CS and ES units at around 31.5% of Ge, above which nanoseparation or formation of a layered structure occurs. The latter releases stress arising from the high coordination of Ge in this concentration region.

To understand the nature of the photo-induced structural development in the a-Ge_xSe_{100-x} network, first-principles simulations are applied. A model system of a-Se composed of 25 atoms is first generated. The required Ge content is achieved through replacement of some Se atoms with Ge, obeying the fourfold coordination of Ge. We used the WIEN2k package [143], with implementation of the Perdew-Burke-Ernzerhof parametrization of the generalized gradient approximation [144]. The periodic boundary conditions (infinite system) were applied to the model systems and the optimization procedure with finest optimization parameters were performed for each a-Ge_xSe_{100-x} composition. The optimization was carried out based on minimization of forces: the force tolerance of 0.5mRyd/Bohr in combination with tight convergence limits on the energy 0.0001Ryd, force 0.1mRyd/Bohr and charge 0.001e. The product of atomic-sphere radius and plane-wave cutoff in k-space was set to 7, while the Brillouin zone of a supercell was covered by the 4 × 4 × 4 Monkhorst-Pack mesh. The energy-separating core and valence electrons were set to -6.0Ryd. The photo-excitation was simulated through removal of an electron from the valence band. The delocalized nature of the hole left in the valence band tails was set to induce lattice relaxation of the immediate neighborhood. This allowed tracking of the photo-induced structural changes and revealed their effect on

electronic properties. By returning the missing electron, the post-excitation regime was reestablished.

5.2.1. a-Ge_xSe_{100-x} structural evolution up to 30% of Ge content and respective light-induced effects

The photo-induced effects in a-Ge_xSe_{100-x} with Ge content x<30% range from photodarkening to photobleaching (Figure 38(a)), [138,156]. The variety of these effects come from the high flexibility of the glassy matrix due to the low (twofold) Se coordination, which becomes more and more restricted with an increase in Ge content. Boolchand et. al. demonstrated that 19.5% concentration of Ge represents the limit of the floppy phase in the Ge-Se system [66]. The flexibility of high-Se-content glasses suggests that the photoexcitation follows the pathway well-known in a-Se - namely, it involves the lone pair electrons of Se atoms [25]. Because of the flexibility of this compositional region, one can expect photo-induced structural changes, e.g., flipping of the Se chains or intermolecular reactions, changes in the van der Waals distances due to Coulomb interactions of photogenerated defects, and even crystallization of the Se content [21,138]. These effects can be superimposed and their experimental identification is difficult, but not impossible. In order to interpret our experimental results and reveal a mechanism of the photo-induced transformations, the photo-excitation in the floppy part of the Ge-Se system with composition $Ge_{19}Se_{81}$ is modeled first. Because photocrystallization should be suppressed at x=19% [138], we expect to observe only transient effects.

We present the structure of the modeled $Ge_{19}Se_{81}$ compound in Figure 42(a). Apparent excess of Se atoms arranges into short elemental chains. With respect to Ge-containing bond types, the CS and ES tetrahedral units are found in the bonding pattern, with preference given to CS. The obtained bonding configurations are consistent with the Raman analysis [78]. At this high Se concentration, Ge atoms usually undergo *sp*3 hybridization and bond to four Se neighboring atoms using two of the Se p-electrons (the other two p-electrons in Se are LP). In this manner, Ge is fourfold coordinated and Se is twofold coordinated in their most natural state. Except for stretching of one of the bonds

at the fourfold Ge site to 2.8Å (see details in Ref. 25), the average length of the Se-Ge bonds is 2.55Å. The Se-Se bond length varies from 2.37 to 2.45Å, which correlates well with the average bond length in a-Se.

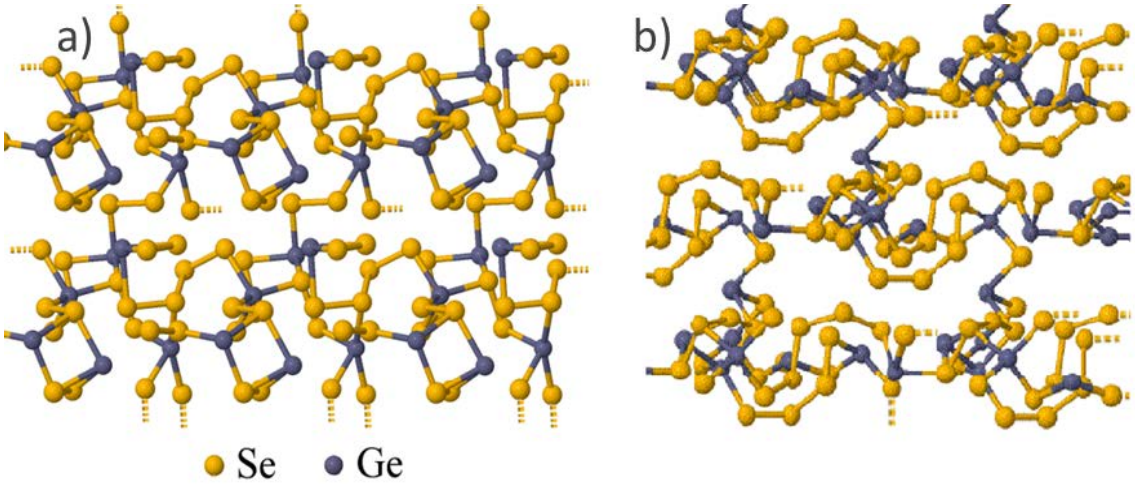

Figure 42. (a) The $Ge_{19}Se_{81}$ structure possesses high amorphicity with almost uniform distribution of the atoms. (b) The $Ge_{28}Se_{72}$ system is distinguished by the well-defined layered structure and appearance of the Ge-Ge bond.

The simulation reveals that photoexcitation in low-Ge content films is governed by the LP states of the Se atoms. Removal of an electron from the valence band occurs from the LP state, which enables a formation of the dynamic Se-Se bond (likewise in a-Se). The lone-pair-state missing electron is shifted deeper into the gap. It induces band gap shrinkage by around 0.05eV, which manifests itself in the transient PD component. With respect to the post-excitation regime, reappearance of the missing electron activates breakage of the light-induced bond and, therefore, the size of the band gap restores to its original value. Alternatively to the dynamic bond, any other Se-Se bond can be broken, which introduces an effect of bond switching. Because the quantity of bonds before and after photo-excitation remains unchanged, the total energy of the $Ge_{19}Se_{81}$ compound is unaffected. The above suggests that the observed structural stability of the $Ge_{19}Se_{81}$ compound against photoexcitation may be linked to the well-known weak-aging property of the intermediate phase (IP) in a-Ge_xSe_{100-x} glasses [66], because this composition is just at the compositional edge of the IP.

For the $Ge_{29.2}Se_{70.8}$ films referred to the stressed rigid phase, transient PB, instead of PD, has been found (see Figure 38(a)). The transient character of the light-induced effects suggests that this thin film still possesses properties typical for the IP. Because the Raman analysis cannot recognize the difference between pre- and post-exposed samples (see Section III), we modeled the photoexcitation in the $Ge_{28}Se_{72}$ system (Figure 42 (b)) to investigate the nature of the transient changes.

The $Ge_{28}Se_{72}$ system is characterized by a well-defined, three-dimensional structure due to an overall increase in cross-linking tendency. In addition to the CS and the increased amount of ES structural units, we observed formation of Ge-Ge ethylenelike bonding configurations. The $Ge_{28}Se_{72}$ structural model suggests that Ge atoms create a skeleton of the layers surrounded by the Se atoms. The former gather into Se chains and form the outrigger raft structure, as proposed by Bridenbaugh and co-workers [157]. The length of the Ge-Ge bond is 2.63Å, and the accompanying Se-Se bond is stretched to 2.80 Å, whereas the rest of the Se-Se bonds range in length from 2.35 to 2.55Å. The length of the Ge-Se bonds randomly varies from 2.32 to 2.60Å. This inhomogeneity is reflected in electronic properties by an ~0.02eV increase in the size of the band gap (in comparison with the $Ge_{19}Se_{81}$ structure). The same trend is observed in data published by Micoulaut et. al. [79].

The structural development in the $Ge_{28}Se_{72}$ system alters the excitation pathway. Instead of LP involvement, excitation causes breakage of the covalent Ge-Se bonds, preferably in the ES configuration. As a result, a dangling bond defect is formed at the Ge atom, whereas the Se atom reestablishes its normal valence to two. Remarkably, the defect state appears at the top of the valence band due to the partial saturation of the dangling bonds through charge exchange with the available LP states. Therefore, the dangling bond is accommodated through the bond elongation in the immediate neighborhood—i.e., without much lattice perturbation. The size of the band gap remains almost unchanged, except that it increases slightly when the Ge-Se bond breaks next to the ETH configuration. In the post-excitation regime, the dangling bond attaches to any two-fold Se atoms. The induced bond switching does not alter the homopolar/heteropolar bond ratio and therefore it has no effect on the total energy of the system or the size of

the band gap. For this reason, no perceptible changes are seen in post-exposed samples on the Raman spectra for $Ge_{29.2}Se_{70.8}$ and $Ge_{32.1}Se_{67.9}$ in Figure 39 and Figure 41.

5.2.2. a-GexSe100-x network peculiarities for x≥30%. Insights into the mechanism of the metastable changes

When the Ge content is x≥30%, the experimental data (see Figure 38(b)) demonstrate a mixture of the transient PD and metastable PB effects. The Raman analysis provides some insight into the metastable changes: the homopolar bonds—i.e., ETH and Se-Se—are converted into the tetrahedral Ge-Se bonding units. However, the Raman results are not sufficient to gain an understanding about the origin of the transient PD and changes in the topology. To establish a complete picture of the photo-induced effects in the stressed-rigid networks, the $Ge_{36}Se_{64}$ system is modeled. Taking into account that the amplitudes of the transient PD and metastable PB grow with increasing Ge content (Figure 38(b)), at a chosen concentration x=36%, we expect metastable changes to be well pronounced.

In the $Ge_{36}Se_{64}$ system, the tendency of Ge atoms to gather into the ETH bonds becomes more apparent (Figure 43(a)). It has a quite different molecular origin because in this structure, the valence saturation is achieved through simple sigma-type bonding on the Ge site with the two p electrons of Se. In this manner, the LP electrons of Se are involved in formation of a dative bond by which they orbit around both atoms, creating a negative charge around the Se atom. In such instances, both Ge and Se atoms appear as threefold coordinated because the length of the dative bond is the same (within a decimal) to the covalent bonds formation. Subsequently, in this composition, Se sites give up lone pairs; i.e., $Ge_{36}Se_{64}$ possesses a deficiency of LP states.

The photoexcitation applied to the model $Ge_{36}Se_{64}$ system is found to induce breakage of Ge-Ge chains and as a result, many dangling bonds at Ge atoms are generated. Because of the deficiency of LP states at the Se atoms, the dangling bonds cannot be saturated. Therefore, the defect states appear in the band gap causing a band-gap shrinkage of ~0.2eV that manifests itself in the transient PD during light exposure (see Figure 38(b)). The increase in PD amplitude with growing Ge content is related to further suppression of the concentration of Se lone pair states. With respect to the

positions of atoms, the unsaturated dangling bonds induce significant lattice perturbation due to displacement of the Ge atoms carrying the dangling bonds towards the Se atoms, which might be in a position to share their electrons.

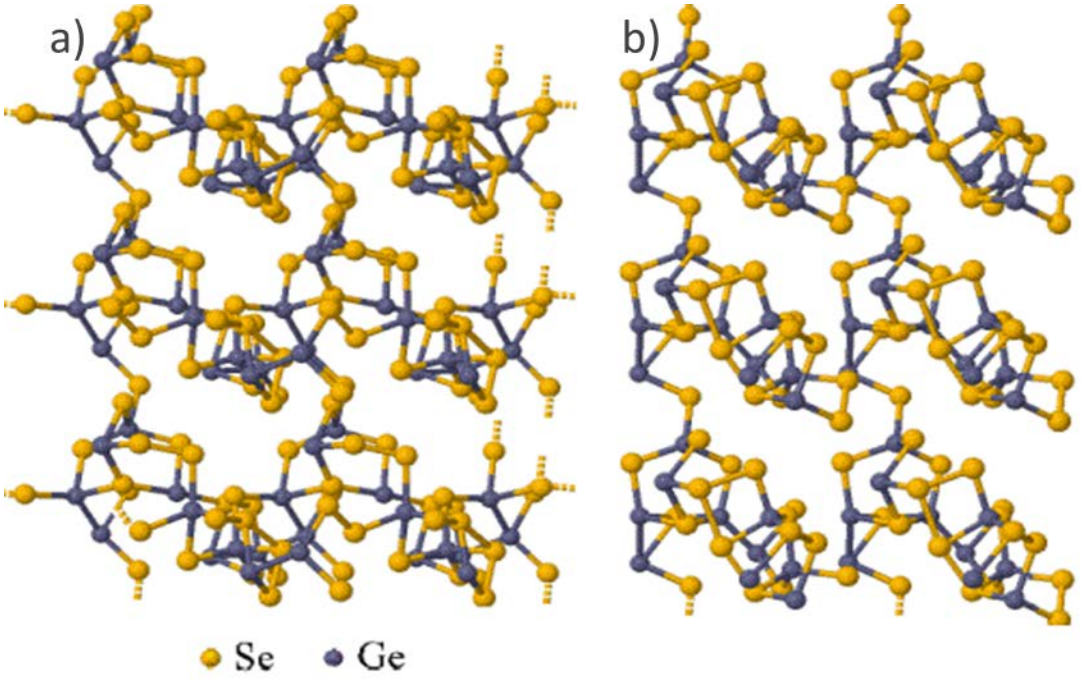

Figure 43. The photo-induced transition of the $Ge_{36}Se_{64}$ system to a more ordered state. (a) Pre- excitation regime: the layered structure with weakly defined molecular cages. (b) Post- excitation regime: clustering of the molecular cages into 3D nanostructures.

In the post-excitation regime, we observed an appearance of the newly formed heteropolar CS and ES bonds and subsequently, a reduction in the homopolar ETH and Se-Se bonds. The heteropolar bonds are assumed to be *more energetically favored* compared to the homopolar ones [154]. The bond conversion induces ordering in structure defined by the development of the dative bonds, with a pronounced effect of clustering into 3D nanostructures. Due to clustering, the length of the Ge-Se bond deviates over a shorter range; it is 2.4–2.6Å after excitation compared to 2.36–2.76Å in the pre-exposed regime, while the Se-Se bonds are stretched by approximately 10%. The photo-induced segregation of clusters is reflected in the electronic properties by an increase in the band-gap size of 0.22eV. It is plausible to assume that experimentally observed metastable PB effect (Figure 38 (b)) reflects the increase in the bandgap size.

The increase of the PB amplitude with Ge content is related to the increase in concentration of the ETH bonds and the subsequent growth of the conversion rate. The total energy of the pre-excited and post-excited structures was found to be in the same range. Therefore, stability of the systems with respect to each other suggests the existence of a potential barrier between them. Additionally, recent studies by neutron scattering of $GeSe_2$ reported the existence of two forms of ordering on a nanoscale [158] and were later confirmed by wider study of Ge-Se compositions by fluctuation transmission electron microscopy [159]. The simulations could not distinguish the forms of ordering as depicted by these methods; however, the confirmation of ordering on a short scale verifies the accuracy of our simulation.

The findings in the simulation of the photo-induced conversion of bonds completely agree with our Raman analysis. To the best of our knowledge, this is the first direct evidence of the conversion of homopolar to heteropolar bonds being responsible for the metastable PB in a-Ge_xSe_{100-x} films. The only other previously reported direct evidence of the light-induced bond conversion was observed on ternary Ge-based glasses such as a-$Ge_xAs_{35-x}Se_{65}$ [160].

5.3. Conclusion

By means of the two-beam transmission technique, a critical concentration of Ge $x \approx 30\%$ was found, which corresponds to the crossover from transient PB to the mixture of transient PD and metastable PB and that can be linked to the transition from the close-to-intermediate phase to the stress-rigid phase. As the result of photoexcitation and relaxation mechanisms modeled with first-principles simulations the correlation with local order and topology became evident. The topology analysis of a-Ge_xSe_{100-x} demonstrated an evolution from homogeneous flexible phase to a layered structure inherent to the stress-rigid phase. A successive study of the excitation mechanism and subsequent light-induced alteration in topology suggests that Ge:Se ratio, rather than network rigidity, plays a decisive role in the manifestation of photo-induced effects. According to the results, alteration in the observed effects is governed by availability of the lone pair states at the Se atoms that are sensitive to the Ge:Se ratio. However, it does

not correlate strictly with the boundaries of the phase transition (x=19.5%, 26%, 31.5% [66]). The secondary role of network rigidity has also been found in a recent study of PIEs in the ternary Ge-containing glasses [160] which supports our findings.

At low Ge content (x<20%), the photo-excitation mechanism follows that of a-Se and involves the lone pair electrons and induces defect states in the band gap, giving rise to the PD [25]. As Ge concentration grows, the number of LP decreases, reaching the critical limit at x≈30%. At this point, the excitation starts to cause Ge-Se bond breakage, thus forming the dangling bonds. These dangling bonds tend to saturate available LP states, resulting in the transient PB (Figure 38(a)). At the same time, the bond switching does not cause changes in the homopolar/heteropolar bond ratio. This is also confirmed by Raman analysis performed on pre- and post- exposed $Ge_{29.2}Se_{70.8}$ samples, where no detectable changes are observed (Figure 39, Figure 41). As Ge content exceeds 30%, nucleation of the Ge atoms into ETH-like structures along with the lone pair deficiency starts to favor the breakage of the Ge-Ge bonds during photoexcitation. The simulations indicate that the unsaturated dangling bonds generate defect states in the band gap, which are responsible for the transient PD in both $Ge_{32.1}Se_{67.9}$ and $Ge_{39.5}Se_{60.5}$ (Figure 38(b)), and which also induces significant lattice perturbation. In the post-excitation period, the latter is found to trigger a conversion of the homo- to hetero-polar bonds that are directly verified by the Raman analysis (Figure 41), i.e., an increase in the edge-sharing to corner-sharing ratio with a simultaneous decrease in ETH. Ultimately, the bond conversion activates transition to the more ordered structure, whose main feature is a clustering effect into 3D nanostructures. It increases the band gap, which can be linked to the experimentally observed metastable PB effect, which becomes more and more pronounced in a post-excitation period with each successive light exposure. However, to validate the changes in the band-gap as the result of formation of light-induced 3D nanostructures, further investigation is required and can be done by absorption spectroscopy methods. The established light-induced clustering is anticipated to be the underlying mechanism responsible for the phase-change memory phenomena in the $Ge_{50}Se_{50}$ films [161].

CHAPTER 6

Application of a-Se in a novel gamma camera for low-energy imaging

This chapter is focused on the application of amorphous selenium in a novel gamma camera for low-energy nuclear medicine imaging. Namely, we propose a first prototype amorphous selenium direct conversion X-ray detector outfitted with a specially designed lead collimator. This device represents a novel fluence integrating gamma camera, which can be used to provide real-time image guidance for interventional breast procedures, e.g. Radioactive Seed Localization (RSL) and Permanent Breast Seed Implantation (PBSI). Its imaging performance is assessed experimentally in realistic breast phantom studies. Promising results are demonstrated.

6.1. a-Se FPXI for digital mammography

X-ray medical images are formed as projections of the body parts onto photographic plate or digital recorder when electromagnetic radiation passes through it. The energy of radiation ranges from 10 to 150keV depending on the clinical task. The very first x-ray images were taken on a film. Then, in the beginning of 20^{th} century, a scintillator screen was introduced in between X-rays and film, substantially boosting the sensitivity [162]. The traditional procedure with this kind of technology, i.e. loading the film/screen cassette, inserting it into x-ray station, carrying it back and developing the film following the exposure, etc. [163], was far from perfect. The technology has continued to evolve utilizing the coupling of X-ray image intensifiers and TV cameras for the real-time fluoroscopy application; digital X-ray imaging, when the irradiated storage phosphor was read out by a laser scanner, etc. [162]. A major advancement in digital X-ray imaging happened with the application of flat panel displays, so-called active matrix arrays (AMAs), originally utilized in laptop computers, as large area integrated circuits. This has led to the development of flat panel X-ray imagers (FPXI) in state-of-the-art X-ray

detector technology used today [164]. The basis of FPXI is the coupling of X-ray sensing material to an AMA which allows generation, storage and readout of an X-ray signal in a real-time. Practical advantages of such systems are in patient management, image handling, viewing and storing, the capability for computer-aided diagnosis, but even more importantly, improved image quality and a possible decrease in radiation exposure. The FPXI can be of two types: *direct* or *indirect* depending on the X-ray-to-signal conversion mechanism. Indirect type includes two steps: first, X-rays are absorbed in a scintillator material (e.g. Thallium doped Cesium Iodide) and converted into visible light. Second, the emitted light is converted into electrical charges in a-Si photodiodes integrated into each pixel of the imaging matrix. In contrast, direct type is a single step approach, where the key component is the X-ray photoconductor (e.g. amorphous Selenium). The photoconductor acts as X-ray-to-charge transducer, converting X-rays directly to the electric charge in a single step. In both approaches the resulting electric signal is proportional to X-ray beam intensity. As such, the magnitude of the signal read out from each pixel contains imaging information brought by the intensity variation of incident X-rays through the imaging object. The choice of the detector is application-driven and depends on the specifics of the organ details to be imaged. The indirect technology will be ignored in the scope of this work and we will focus on direct conversion imaging in the low energy range.

The X-ray photoconductive material is the key component for a successful direct conversion detector and must exhibit several characteristics, such as the ability to be readily deposited over large area, high X-ray sensitivity and charge collection efficiency, relatively low dark current and suitable resolution and detective quantum efficiency (DQE). In addition, the photoconductor of choice must be relatively low cost and show good reliability to endure numerous cycles of charging and discharging. Although there are number of polycrystalline materials that have shown potential to be utilized in FPXI (e.g. PbO [165,166], CdZnTe [167,168], HgI_2 [169,170]), they still suffer from large dark currents or low charge collection efficiency [171]. The only commercially viable photoconductor in direct conversion X-ray detectors to date is stabilized amorphous selenium.

Stabilization of a-Se structure for FPXI application requires special attention. This is due to the inherent metastability of a-Se, as discussed in great detail in Chapters 2 and 4. If not controlled, this can cause a-Se crystallization, and degradation of its imaging performance. The recipe which was found to be effective in preventing crystallization for FPXI is alloying of pure a-Se with 0.2-0.5% of arsenic (As) and doping it with chlorine (Cl) in the ppm range [23]. Addition of As atoms to a-Se matrix links some of the selenium chains and as such increases viscosity. Although it helps to release strain and prevent crystallization, it also introduces traps for holes (main charge carrier type in a-Se). To restore hole lifetime, Cl in added, and completes the stabilization recipe [34]. Stabilized a-Se has proven to exhibit good reliability [5].

Several other reasons make a-Se the best-known photoconductor for FPXI, especially for mammography, where low energies are used for imaging (≈20keV). The X-ray sensitivity is outstanding, i.e. an 150-200μm photoconductive layer absorbs almost 100% of ≈20keV X-rays [171] with the reasonably high electron-hole pair creation efficiency [172]. Amorphous selenium can be readily deposited over large area electronics preserving good uniformity by conventional vacuum deposition techniques at reasonable substrate temperatures with no harm to the sensitive electronic components (such as AMAs). In terms of transport properties, because both electrons and holes are mobile in a-Se, both charge carriers can drift and contribute to the photoconductivity. By design, holes are usually collected on the pixel since its mobility is much higher, 0.13-0.14 $cm^2V^{-1}s^{-1}$ versus 5-7 x 10^{-3} $cm^2V^{-1}s^{-1}$ for electrons [5]. The latter is very important because X-rays are absorbed throughout the bulk of the material and if only one carrier type is mobile, the other is trapped which can result in significant loss of device sensitivity and potential lag and ghosting problems. In addition, the dark current (a leakage of current after the material is charged and kept in the dark) levels at room temperature are relatively small in a-Se (less than $1pAmm^{-1}$) compared with many other photoconductors [5,173]. This is due to the invention of so-called blocking layers which have enabled switching from metal-a-Se-metal structures to a special multilayered *n-i-p* structure to prevent high dark current at high electric fields and therefore ensure high X-ray sensitivity [171].

In the state-of-the-art a-Se mammography imagers, the a-Se layer is combined with an active matrix array. Figure 44 schematically shows an AMA in combination with other system components (on the left) and an individual pixel diagram (on the right). AMA is a two-dimensional array of pixels each of which incorporates thin film transistors (TFT). TFTs are usually large-area deposited hydrogenated amorphous silicon based, which can be externally addressed through gate lines enabling pixel read out through data lines [171]. An a-Se layer with respective blocking layers forming the *n-i-p* structure are deposited over the pixel electrode (bottom electrode). On top of the blocking layer surface continuous electrode (top electrode) is applied. This structure allows application of high electric field to sustain an internal field in the photoconductive layer of ~10V/μm with reasonably low dark current, and provides efficient X-rays-to-charge conversion and subsequent collection. Generated electric charges in the a-Se layer are collected by the sensing element, a storage capacitor electrically connected to the photoconductive layer through the pixel electrode.

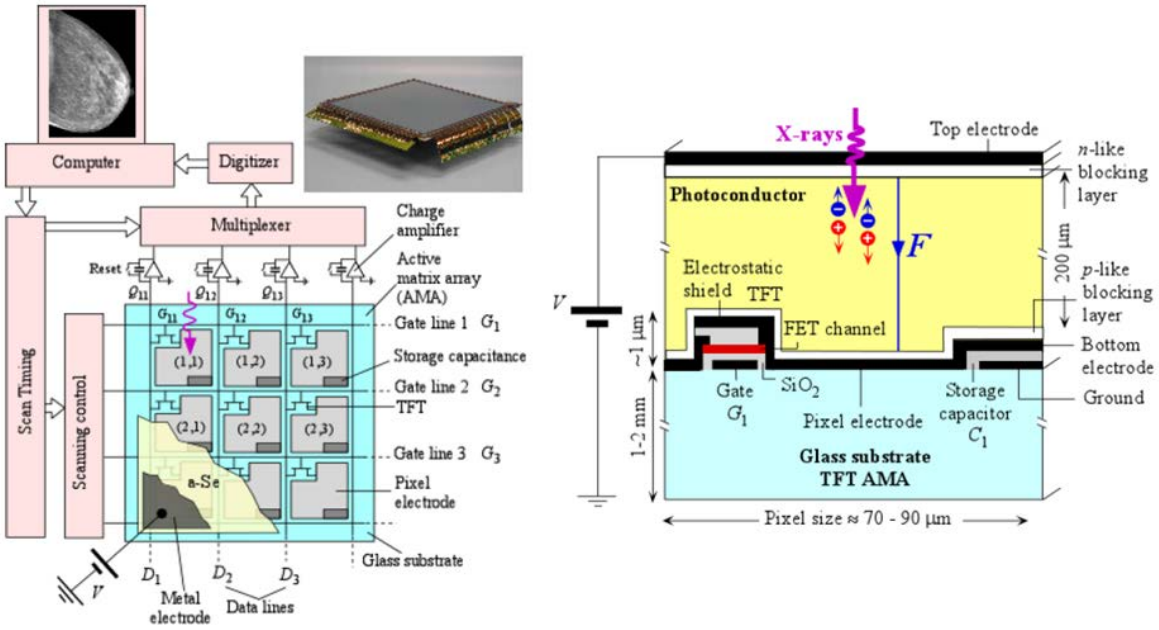

Figure 44. Left: schematics of AMA in combination with a-Se layer, peripheral electronics and computer enabling sensor operation. Right: individual pixel schematics, including: top and bottom electrodes and *n-i-p* a-Se structure, TFT, storage capacitor and glass substrate.

As generated charge carriers are drifting through the photoconductive layer, a current is induced which is integrated on the storage capacitor depositing an amount of charge corresponding to amount of X-ray generated carriers. Next, signal readout is enabled through the TFT. The TFT is incorporated in each pixel and acts as a switch controlled by the voltage applied to the gate. When the TFT is in its "off" state the resistance between source and drain contacts is infinitely high and generated charge is collected on the storage capacitor. When the TFT is in its "on" state the resistance between source and drain is significantly lowered allowing for the stored charge to be transferred to the feedback capacitor of the amplifier through the data lines. The feedback capacitor determines the gain of the signal, but the output analog signal is always proportional to the amount of integrated charge and therefore intensity of incident X-rays. Then analog-to-digital conversion takes place and usually requires a resolution of 12-16 bit for mammography. After the digitization, sophisticated image correction algorithms are applied to deliver perfect looking images. An example of two typical images of breast and a hand obtained by a-Se flat panel imagers developed and marketed by Analogic Canada Corporation (former name Anrad) are presented on Figure 45.

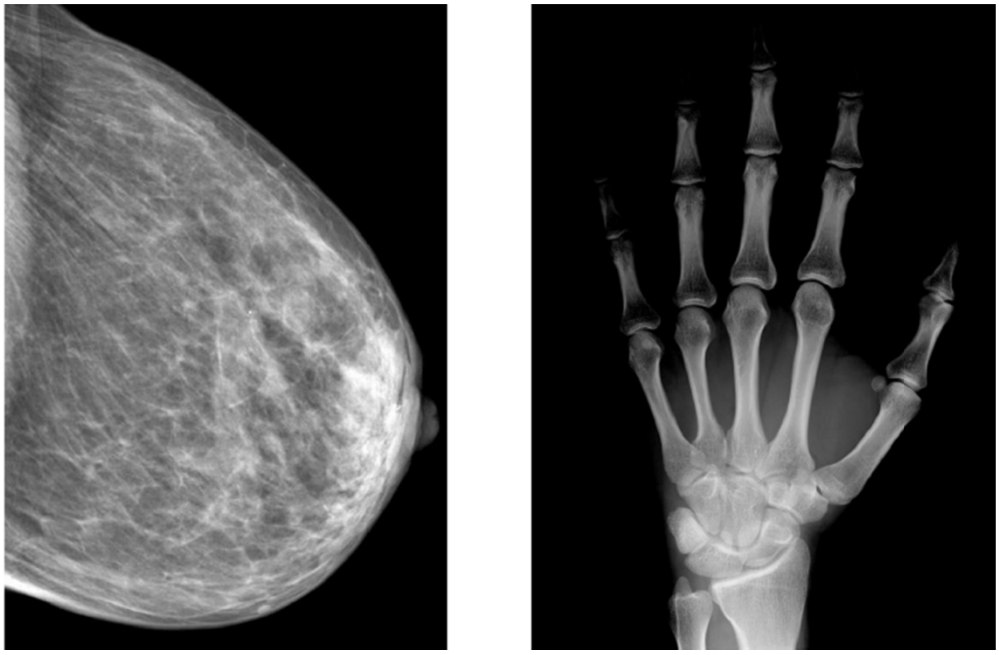

Figure 45. X-ray images of the breast and hand acquired by Analogic a-Se flat panel X-ray imagers [171].

The big advantage of this type of technology is the relatively short times for image formation and processing or the high frame rate which allows for digital breast tomosynthesis, a novel technology when several X-ray images taken at different angles enable three-dimensional image visualization [174].

The basics of Analogic a-Se FPXI was described in detail, as an understanding is needed to introduce the concept of a novel gamma camera. Nevertheless it has to be noted that other companies i.e. Hologic, and Fuji are producing commercial a-Se based X-ray detectors incorporating different pixel designs and/or readout techniques [175].

This section has demonstrated successful application of amorphous selenium in diagnostic imaging. We believe that its application can be extended further to guide therapeutic procedures. In particular, breast cancer treatment with Radio Seed Localization and Low Energy Breast Brachytherapy procedures.

6.2. Radioactive seeds procedures in breast cancer management

At present, the primary treatment option for breast cancer patients diagnosed at the early stage of the disease is breast conserving therapy (BCT). Conventional BCT includes two major steps. First is lumpectomy - surgery for tumor and safety margin removal; and second is post-operative whole-breast irradiation (WBI) by means of external beam radiotherapy to prevent local recurrence.

Currently, the standard method to localize and remove a non-palpable breast lesion is wire-guided surgical biopsy (WGSB). WGSB involves the insertion of a hooked wire into center of the lesion on the day of surgery, followed by excision of the tissue surrounding the wire. Although, WGSB is utilized in about 75% of treatments of non-palpable breast cancers [176], it has several disadvantages and in particular high rates for positive margins, where the cancerous cells are found at the cut edge of the excised volume after evaluation following excision. Other issues associated with WGSB can be found in Refs. [177, 178,179, 180,181,182,183]. As the result of WGSB a re-operation or even surgical removal of breast is often required [184]. These incidents could potentially be reduced with a novel Radioactive Seed Localization procedure focused on complete

excision of all disease, while minimizing the amount of unnecessarily excised normal breast tissue.

6.2.1. Radioactive Seed Localization, requirements for image guidance.

Radioactive seed localization (RSL) was introduced in 1999 as an alternative to WGSB [185]. The RSL procedure involves implantation of a titanium seed containing low-activity iodine-125 (^{125}I) in the center of the tumor under radiographic or ultrasound guidance allowing for intraoperative lesion localization using a hand-held gamma probe. This is usually done up to 5 days prior to surgery which notably improves patient convenience and surgical scheduling. The other major benefit is lower incidence of positive margins and therefore fewer reoperations [186]. During the surgery, continuous measurement of ^{125}I gamma emission is carried out to locate the seed, the maximum counts are marked on the skin followed by removal of the lesion and seed from the patient. The gamma probe is further used to examine the signal from the removed specimen and from the wound to confirm successful tumor removal. As a result the RSL technique is currently gaining popularity worldwide and it is already used as standard clinical care in a number of hospitals [187].

The current systems used for detecting the radioactive seeds for RSL are non-imaging gamma probes (e.g. Neoprobe or RMD Navigator GPS); however, the spatial resolution of the probe is poor (~15–26 mm). As a result of poor spatial resolution, optimal tumor bracketing is not always possible. In addition, the use of non-imaging probes limits RSL to a single seed that may be insufficient to ensure a reliable and guaranteed resection of the tumor leaving clear surgical margins. It is reasonable to assume that cancer removal with more precision and "comfort" for a surgeon can be performed using multiple seeds. Ideally, at the time of surgery, the entire tumor extent would be bracketed by a number of radioactive seeds with an imaging system available to identify their positions. Given that multiple radioactive seeds will be used to mark the perimeter of a 1 cm diameter lesion and that they could be as close as ~ 5 mm apart, the required imaging system to guide RSL must have a spatial resolution of at least 5 mm.

Additionally, since the system would be used for intraoperative guidance, image acquisition must be on the order of ~ 5 minutes.

A novel gamma-camera proposed under the scope of this thesis can be used for real-time guidance for the RSL procedure as will be shown.

6.2.2. Permanent Breast Seed Implantation, requirements for image guidance.

The current treatment paradigm of breast cancer involves post-operative irradiation of the entire breast (WBI). However, over the past decade new radio therapeutic options such as Accelerated Partial Breast Irradiation (APBI) have emerged to offer alternative post-lumpectomy treatment. APBI offers *i)* decreased overall treatment time (5 days compared to 3.5 to 7 weeks with WBI) and *ii)* a possible decease in the dose delivered to uninvolved portions of breast as well as to the adjacent organs (e.g. heart, lung, rib tissues). This results in a potential to provide patients with more suitable post-operative therapy option. APBI includes multiple techniques in different stages of development and acceptance [188,189].

Among the different ways to deliver APBI, Permanent Breast Seed Implantation (PBSI), a novel technique that has been recently pioneered in Sunnybrook Health Science Centre (Toronto, Canada) [190] and is currently being adopted by more cancer centers (e.g. British Columbia Cancer Agency, Tom Baker Cancer Centre in Alberta and others). Using the same principle as low-energy prostate brachytherapy, PBSI involves permanent implantation of low-energy radioactive Palladium- 103 (^{103}Pd), stranded seeds under ultrasound guidance into the lumpectomy cavity to deliver precisely calculated dose to the target volume within the safety margins. The distinct advantage of the procedure is that it lasts only about one hour with same day patient discharge. This dramatically improves the patient's quality of life compared to conventional WBI and even other APBI approaches with 5-day daily treatment. Reduction of the acute skin reactions compared with WBI is also reported [191]. PBSI has already shown a strong potential in clinical trials, however, the current limitation is the inability to visualize brachytherapy seeds as they are being implanted.

To understand this problem, let's look at the PBSI procedure more in details. The treatment planning is done prior to the procedure to define the target volume and plan actual seed implantation (Figure 46). Once the patient is anaesthetised, a fiducial needle is inserted under ultrasound guidance to hook the surgical cavity, after, it is attached to a specially designed template which guides the insertion of needles loaded with seeds according to the treatment plan (Figure 46).

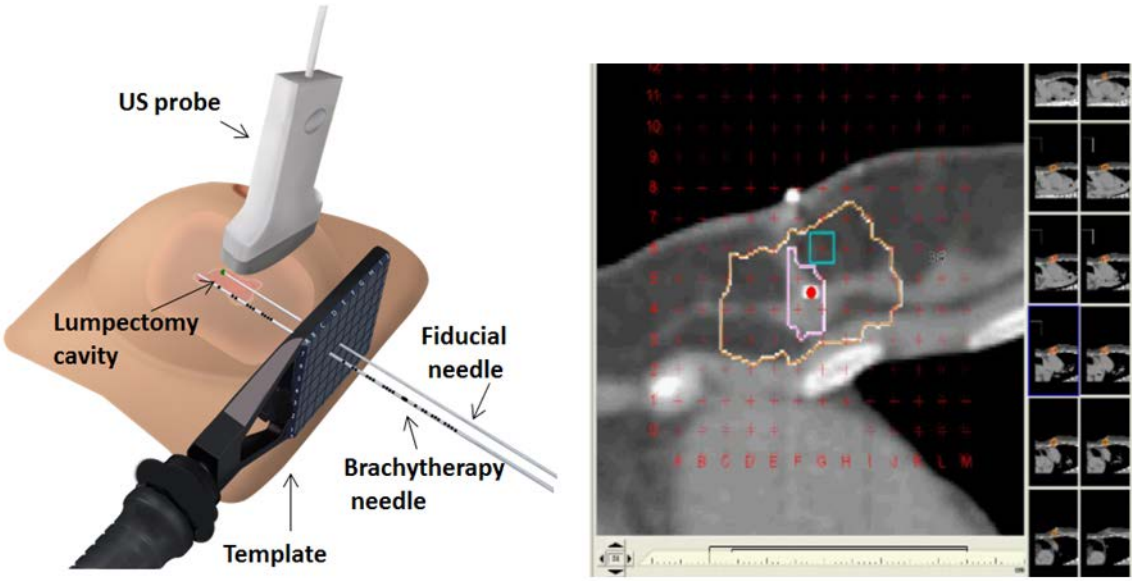

Figure 46. PBSI procedure, showing treatment planning on the right and illustration of the actual procedure on the left.

Presently, the only on-line imaging device that helps guide the procedure is ultrasound, which successfully guides the needle insertion, but once seeds are released they are no longer distinguishable due to the speckle in the ultrasound images. The air bubbles present in ultrasound images, as well as presence of seroma and fibrotic tissue make is difficult to distinguish seeds, so real-time correction cannot be performed. Furthermore, if the mismatch in seed position (from treatment plan) is greater than 5 mm the creation of undesirable "hot" or "cold" spots may occur in the target volume. For this reason the implementation of PBSI into routine clinical practice requires a specialized on-line imaging device which will enable intraoperative guidance. The main requirements for such a device are: high sensitivity for low-energy imaging, since the principle energies of Pd-103 seeds are 20keV (65.6%), 23keV (12.5%) [192]; image acquisition no

longer than 2 minutes per image, so that correction can be performed while patient is still anesthetized; spatial resolution at least 5mm, so that misplaced seeds can be detected and corrected if necessary; and the dedicated camera must be readily available to guide and evaluate dose distribution during and at the end of the implantation without interfering with the surgical procedure.

6.3. Novel a-Se based gamma-camera

An amorphous selenium (a-Se) direct conversion X-ray detector outfitted with a specially designed hexagonal lead collimator, that can provide image guidance for PBSI and RSL procedures, is proposed. The following reasoning has led us to this idea.

A dedicated gamma camera provides the most straightforward approach to guide both RSL and PBSI procedures because the radioactivity of the implanted seeds can be detected and as such the radioactive sources localized. Requirements for the dedicated imager were previously identified by Ravi et al. [193]. These are:

1. Capability to image low energy sources with the primary photon energies of the ^{125}I and ^{103}Pd seeds being 20, 23, 27, 31 and 35keV.
2. Time available to image the seed distribution must be kept between 1 to 2 minutes per image.
3. The required spatial resolution must be at least 5 mm.
4. Imaging must be carried out with no interference with the surgical procedure.

Although gamma cameras are widely used for various applications in nuclear medicine, none that are currently available fit the requirements for both PBSI and RSL. The majority of commercially available gamma cameras use sodium iodide (NaI) scintillation crystals in conjunction with photomultiplier tubes. The problem with these designs is that the aluminum casing, which is needed to seal the hygroscopic NaI crystal, absorb most of the low energy (21–35keV) photons emitted by the seeds, preventing them from being imaged. An alternative approach is a direct-conversion gamma camera based on a Cadmium Zinc Telluride (CZT) photoconductor, which does not require an aluminum seal [194]. However, the read-out electronics (including an Application

Specific Integration Circuit) for all available CZT gamma cameras are designed for imaging at the Thallium-201 (^{201}Tl) and Technetium-99m (^{99m}Tc) energy range—i.e., at energies much higher than required for PBSI and RSL. Therefore, commercially available gamma cameras and imaging probes cannot image either ^{125}I or ^{103}Pd seeds, since their signals are outside of the supported energy range.

It is important to emphasize that all conventional gamma cameras for nuclear medicine use energy-discrimination and photon-counting technologies to discard scattered photons and to acquire "true" images using non-scattered primary photons emitted from the source of radioactivity. Energy discrimination is needed for "high energy" (>60keV) applications to reject photons that undergo Compton scattering in the patient's body. In contrast, for low-energy applications (<35keV), energy discrimination is not efficient because the probability of scattering events is significantly reduced and photon-energy changes due to Compton scattering are too small to discriminate. To demonstrate this statement, consider that the average photon energy of ^{103}Pd seeds is ~21keV, the energy of photons reduced due to the Compton scattering E_{SC}, can be calculated by the Eq.6 [195]

$$E_{SC} = \frac{E_\gamma}{1 + {E_\gamma(1-\cos\theta)}/{0.5111}}, \qquad (6)$$

where θ is the scattered angle and E_γ is the energy of incident gamma photon in eV. Thus, for the ^{103}Pd seeds, maximum reduction of the energy due to the Compton scattering is due to the backscattered photons ($\theta = 180^0$) and is around 19.4keV, which means that in principle energy discrimination for low energy imaging is useless.

Since no energy discrimination is required for low-energy imaging this leads us to the idea that a charge integrating readout mode can be utilized, in the same way it is currently realized in mammography detectors based on AMAs technology (Figure 44). Furthermore, understanding the perfect suitability of a-Se as a photoconductor in the low-energy range makes it the logical material of choice for gamma-ray-to-charge conversion for imaging of ^{125}I or ^{103}Pd radioactive sources. In addition, since the radioactive seeds emit radiation in all directions it is obvious that a dedicated collimator must be used to

maximize spatial resolution of the proposed gamma camera. For the latter, sensitivity must be also taken into account (e.g. improving resolution by increasing the hole length of the collimator results in decrease of sensitivity or increase in imaging time, which must not exceed 2min).

To demonstrate the feasibility of an a-Se direct conversion gamma camera for radioactive seeds localization we built a prototype and tested it in realistic breast phantoms mimicking dense breast tissue and fatty breast tissue. A first laboratory prototype of an a-Se gamma camera is based on the Large Field of View Analogic AXS-2430 flat panel mammography detector [196] outfitted with a lead collimator specially designed for low energy applications.

6.4. Proof of concept studies

6.4.1. Experimental setup

The experimental setup simulating interventional radioactive seed procedures is shown in Figure 47. Experiments were performed using two separate phantoms made of paraffin wax and Lucite layers, mimicking fatty breast tissue and dense breast tissue respectively.

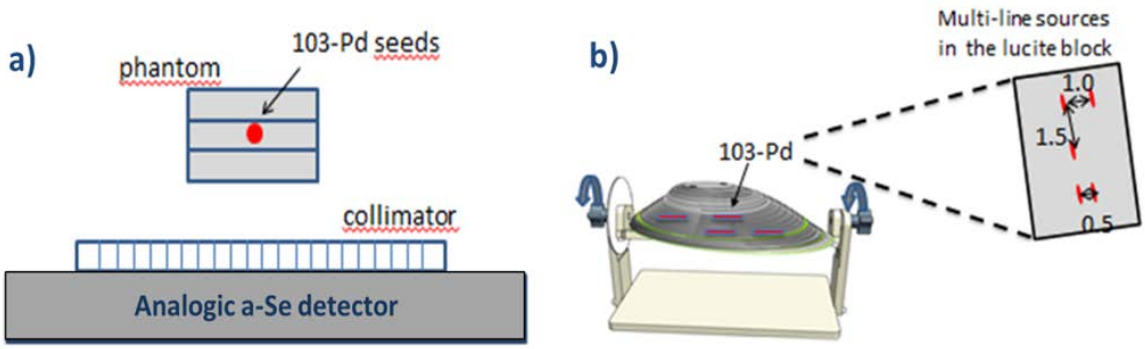

Figure 47. Experimental setup: (a) schematic representation of all setup components; (b) example of the phantom mimicking dense breast tissue with the implanted radioactive Palladium-103 seeds at different depth and separation distance.

The breast phantom thickness varied from 3 to 6 cm. From 1 to 5 brachytherapy Palladium-103 radioactive sources were implanted at the separation distance 0.5, 1 and

1.5 cm (see example with Lucite phantom in Figure 47(b)). A laboratory prototype of a gamma camera dedicated to imaging in 20-35keV energy range was constructed of an Analogic Large Field of View a-Se direct conversion x-ray mammography plat panel detector outfitted with a specially designed hexagonal lead collimator (Figure 48). The collimator parameters were determined based on a Monte Carlo simulation, optimizing spatial resolution and acquisition times against clinical requirements and taking into account current manufacturing limitations. The collimator shown in Figure 48 utilized over the course of experiments is a custom-made lead collimator manufactured by Nuclear Fields [197] with 10 × 10 cm field-of-view, hole diameter of 1.5mm, hole length of 25.3mm and septa size of 0.23mm. To quantify the camera response, the breast phantom with implanted 103-Pd seeds was placed in front of the collimator face and the seed radioactivity was imaged. Phantom-to-detector distances varied from 3 to 20cm by bringing phantoms closer to the camera. Image acquisition time was tuned to 1 minute and the radioactive sources were imaged over a time of up to two minutes for each set of parameters.

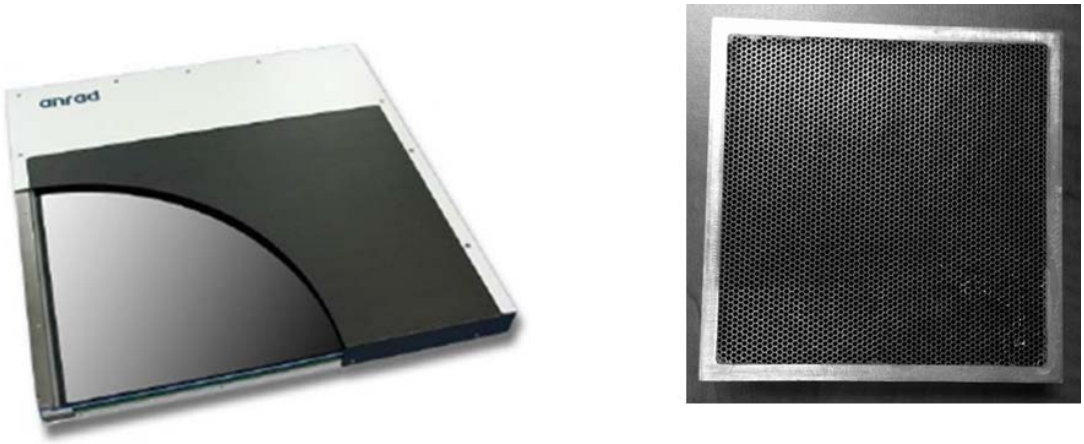

Figure 48. Left: Analogic Large Field of View AXS-2430 a-Se digital X-ray sensor [198]. Right: specially designed lead collimator enclosed in aluminum ring for safety considerations.

6.4.2. Results and discussion

In Figure 49 we present an example of images obtained with the fluence integrating gamma camera prototype. Four ^{103}Pd radioactive seeds at separation distances 5, 10 and

15mm embedded in a wax phantom were imaged in a less than 2 minutes with a phantom-to-detector distance of 7cm. Different amounts of wax layers, 4, 2, 1 and 0cm were mimicked different thicknesses of fatty breast tissue. It is evident from Figure 49 that the four seeds are clearly distinguishable visually, although the signal is fading out as the thickness of wax layers increases. This is not unexpected due to the higher attenuation in the thicker material. One may suggest that the quality of the images in cases of in excess of 2cm of wax are poor. However, we would like to emphasize that in order to locate seeds and provide sufficient image guidance for PBSI and RSL, the detection of seeds position rather than high resolution images of the radioactive sources themselves is required. In other words, to fulfill the clinical requirements for radioactive seed procedures, seed location in the target volume is the main interest, not an actual image of the seed.

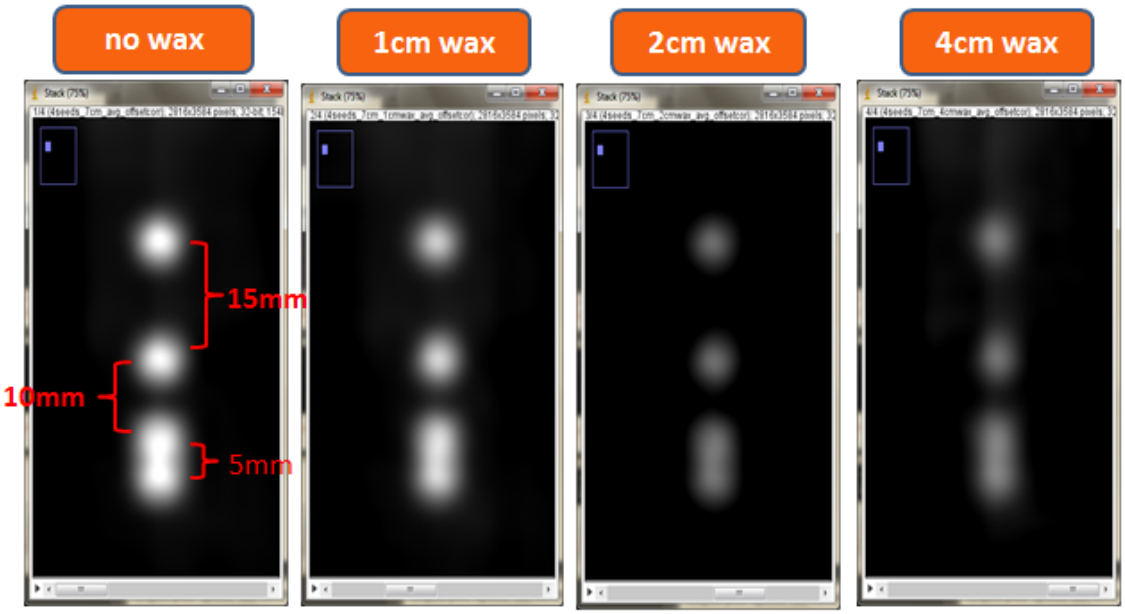

Figure 49. Images of 4 seeds separated by 5, 10, 15mm in a phantom mimicking 1cm, 2cm and 4cm of fatty breast tissue, phantom-to-detector distance is 7cm.

The presented images are satisfactory as long as the coordinates of the seeds can be resolved from image profiles, e.g. with Gaussian fitting (Figure 50). Figure 50 demonstrates that with simplest Gaussian fit, positions of seeds from the experiment depicted in Figure 49 can be derived. It is clear from Figure 50 that even in the extreme

case of 4cm of wax and 5mm seed separation, seeds positions can be easily resolved with 2 minutes of imaging time. Once the seed coordinates are obtained, using a priori knowledge of the approximate position of the seeds based on the treatment planning, a 3D reconstruction of seed distribution with respect to the imager reference frame can be carried out.

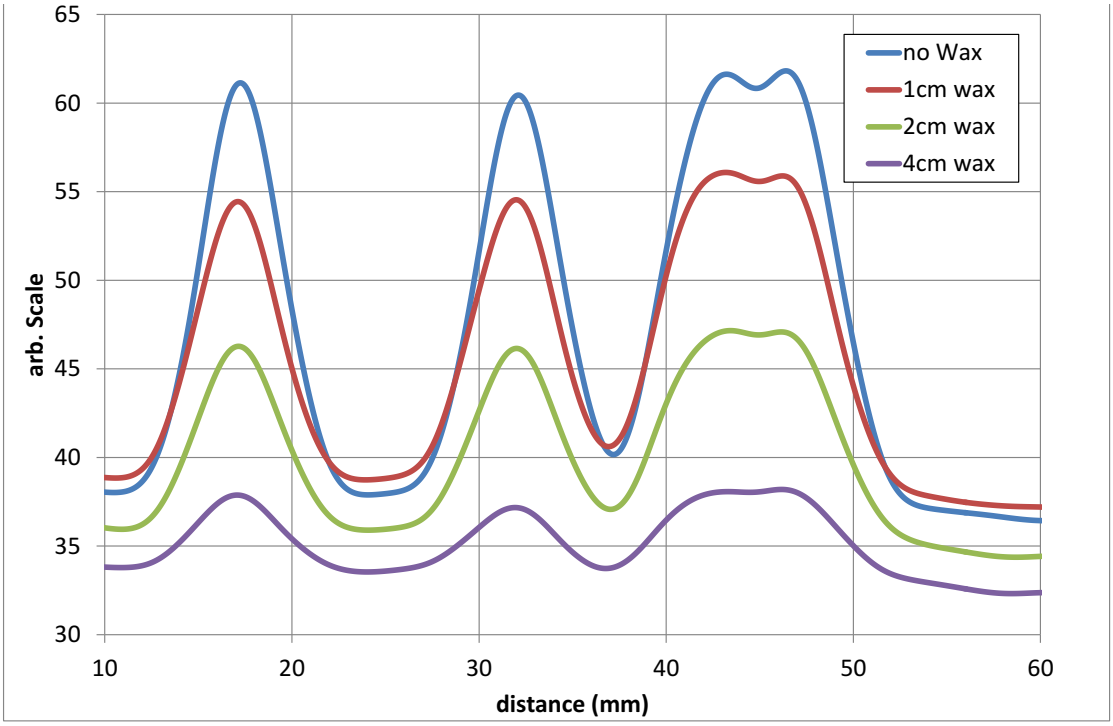

Figure 50. An example of Gaussian fit of the imaging profiles from Figure 49: four seeds separated by 5, 10 and 15mm in a phantom mimicking 0, 1, 2 and 4cm of fatty breast tissue with phantom-to-camera distance of 7cm. Imaging time is less than 2 min.

6.5. Conclusion and future work

To the best of our knowledge the proposed fluence integrating gamma camera is the first of its kind to enable low-energy gamma imaging and which fulfills all clinical requirements for radioactive seed procedures. It is a novel (although very practical) imaging device capable of imaging radioactive ^{125}I and ^{103}Pd seeds with adequate spatial resolution and short acquisition time, thus meeting the requirements for Radioactive Seeds Localization and Permanent Breast Seed Implantation which both significantly improve breast cancer treatment. The approach to use a flat panel mammographic

detector with charge integration readout as a gamma camera eliminates the expensive components inherent in existing gamma cameras designed for high-energy applications (i.e., photon counting readout electronics and energy discriminator), and it enables fast image acquisition of low-energy radioisotopes used in PBSI and RSL. Despite the unusual design of the gamma camera, experimental results prove that the concept of a fluence integrating gamma camera without an energy discriminator can work for low energy applications and confirms the validity of the proposed approach. Indeed, such a system is able to resolve radioactive seed positions with accuracy adequate for RSL and PBSI (<5mm) within the specified imaging time of 2min. Further optimization of the camera may include modification of the system form factor, e.g. the combination of two detector heads which would allow acquisition of two views simultaneously, so that the imaging time would be decreased by a factor of two and the degree of seed overlap in each projection would be also minimized.

Although the proposed gamma camera proved its capability to locate the seeds and as such predict dose distribution, it does not provide anatomical information of the target volume. In the future, we propose to merge a fluence integrating gamma camera with a 3D ultrasound system to address this issue. Thus, emission images from the seeds acquired by the gamma camera can be co-registered with anatomical landmarks to ultimately provide dose distribution with respect to anatomy. To achieve this for RSL, optical images of the breast surface can be imaged in real-time and simultaneously an infrared camera can be used to track infrared markers placed on the outer edge of the surgical field and placed on the gamma camera system. In this fashion we can relate the position of the radioactive seeds to a real time image of the breast surface. This approach can be also adapted to PBSI, instead of optical imaging, the position of the radioactive sources can be related to real-time superficial ultrasound images of the surgical cavity.

CONCLUDING REMARKS

This thesis contributes to the both: (1) fundamental understanding of the nature of light-induced effects, namely photodarkening (PD), photobleaching (PB) and photo-induced crystallization (PC) in amorphous selenium (a-Se) and in germanium selenide (a-Ge_xSe_{100-x}) ChGs; and (2) applications of a-Se in medical imaging, as it introduces the idea of a-Se based fluence integrating gamma camera for low-energy applications to facilitate image guidance for emerging breast cancer treatment procedures.

Our findings on photo-induced effects in a-Se can be summarized as follows: distinctly different photodarkening effects were shown to be caused by above-bandgap and sub-bandgap optical excitations. This was studied by monitoring the kinetics of PD build-up and relaxation. For the above-bandgap illumination, only transient PD was observed and its relaxation kinetics was characterized by one time constant of 2.5s, which is essentially temperature independent. This time is required to restore a-Se to the ground state configuration, which involves relaxation of the photoexcited electron through multi-phonon emission, with no bond rearrangements involved. For the sub-bandgap illumination, both transient and metastable PD were observed, with two characteristic time constants: a temperature independent 2.5s and temperature dependent longer time constant (85s at room temperature (RT)). Whereas transient PD is concluded to be of the same nature as in the above-bandgap excitation case, the metastable PD requires longer relaxation to overcome an energy barrier of around 0.8eV, either by thermal activation above RT or by configurational tunneling below RT. Furthermore, if the formation of metastable structural configuration is left unrestored this can lead to irreversible structural transformation (crystallization). To summarize, if a-Se photodetectors are designed to work in the blue light or UV range, their lifetime would be prolonged since above-bandgap excitation is not an efficient trigger of phase transition.

Our detailed investigation of the effect of substrate rigidity on photo-induced crystallization in a-Se allows us to conclude that a softer film-substrate interface can suppress the photo-induced crystallization effect. The same occurs by operation near the glass transition, T_g. Thus, flexible substrates, soft intermediate layers and operation at

temperatures close to T_g can enhance resistivity of a-Se structures against the undesirable PC effect.

Our investigation of light-induced effects, i.e. photodarkening and photobleaching, across the glass forming region of $a\text{-}Ge_xSe_{100-x}$ systems by a combination of experimental study and theoretical modeling has allowed us to reveal the microscopic nature of the observed effects. We found that Ge:Se ratio plays a decisive role in the pathway for photoexcitation as well as in subsequent relaxation. Indeed, the availability of lone pair electrons at Se atoms, whose concentration strictly depends on the Ge:Se ratio, governs different photo-induced effects for different glass compositions. At low-Ge content (x<20%) the photoexcitation follows the same path as for a-Se, causing a PD effect. As the Ge content reaches 30%, the Ge-Se bond breakage becomes a dominant process during photoexcitation, which results in dangling bonds generation which saturates available LP states and thereby causes the transient PB effect. Concentration x=30% was found to be critical, as lone pair deficiency along with the formation of ethylenelike (ETH) Ge-Ge bonds results in ETH bond breakage during photoexcitation. On the macroscopic level this results in transient photodarkening due to unsaturated dangling bonds in the band gap (during photoexcitation) and subsequent homopolar to heteropolar bonds conversion in the post-excitation period causing metastable photobleaching effect. The amplitude of metastable PB becomes more pronounced as the Ge content further increases. Interestingly enough, the homo- to hetero- polar bond conversion in the post-excitation period triggers a transition to the more ordered state characterized by the formation of 3D nanostructures (clustering effect), which in turn increase the bandgap. This was observed experimentally as the metastable PB effect. In the future, validation of the light-induced 3D nanostructures can be done using absorption spectroscopy methods.

Finally, the results of a-Se gamma camera project can be outlined as follows: we proposed a novel, but very practical solution to use a flat panel a-Se mammographic detector outfitted with the specially designed collimator as a gamma camera for low-energy imaging. Such a fluence integrating gamma camera eliminates the expensive components inherent to conventional gamma cameras designed for high-energy

applications, namely, photon counting readout electronics and an energy discriminator. This in turn provides a low-cost solution that can enable real-time image guidance for emerging breast cancer treatment procedures that involve radioactive seeds implantations. We demonstrated the potential of the proposed device to fulfill the clinical requirements for localizing radioactive seeds in realistic breast phantom studies. Although our lab prototype was not fully optimized, it was able to resolve radioactive seed positions with an accuracy less than 5mm within a specified imaging time of 2min. The next steps in this project may include: *i.* optimizing the camera form factor (e.g. the combination of two detector heads which would allow acquisition of two views simultaneously), *ii.* the development of an automated algorithm for the precise localization of the radioactive sources from the gamma camera images; and *iii.* co-registration of this information with 3D ultrasound images to ultimately provide surgeons with dose distribution with respect to anatomical target.

APPENDIX

APPENDIX A. Samples preparation

Amorphous materials are usually produced in two forms: bulk glassy samples and thin films. Bulk samples are commonly prepared through melt-quenching process, when the material molten is rapidly cooled down and pressed; or sometimes from solution, i.e. chemical precipitation process. Thin films can be made by various evaporation methods, e.g. thermal or chemical evaporation, radio-frequency discharge, cathode sputtering or glow discharge [199]. The most common method to prepare thin films, however, is the vacuum thermal evaporation, as the result of which vapor containing atoms and/or molecules of the material are condensed onto a suitable substrate forming the film.

A.1. a-Se deposition

Amorphous Se films are normally vapor-grown. Selenium has a relatively low melting temperature, around 220^{o}C [26] and can be relatively quickly prepared exhibiting good uniformity. It is important to note that parameters such as substrate temperature, purity of the substrate surface and boat temperature are of critical importance for the optical and electrical properties of the material. Boat temperature affects the rate of deposition as well as the material structure, since evaporation may result in film formation by individual atoms, molecules or from clusters of different size. Another important property for a-Se films is aging, reported for the samples deposited on the cold substrates [200]. It occurs at room temperature and is attributed to structural relaxation which results in an atomic concentration increase and a thickness decrease [201]. This also affects electronic transport properties [202]. Aging has not been found to affect the optical properties of the samples deposited on heated substrates and annealed close to glass transition after the deposition.

Substrate surface impurities as well as insufficient temperature can cause a crystallization process in the amorphous film, e.g. crystallization which starts from nucleation centers on

the surface can spread through the entire film depending on the temperature and the nature of the contaminated centers.

We have deposited high quality pure and stabilized amorphous selenium layers (stabilized refers to alloying with 0.5% of arsenic to prevent crystallization together with added chlorine doping in the ppm range to compensate for hole traps introduced through the addition of As [23]) onto glass coated with indium tin oxide (ITO) substrates in the Thunder Bay Regional Research Institute clean room facilities (Figure 51). Standard ITO coated corning glass of 0.7mm thickness was chosen, since some samples are used for electrical measurements, which are not discussed within the scope of this thesis.

Figure 51. Vacuum deposition system utilized for a-Se deposition in Thunder Bay Regional Research Institute clean rooms facilities.

For one typical deposition run 7.5g of Se pellets of 99.9999% purity were loaded in molybdenum crucible. The chamber was then closed and the system pumped down to around 10^{-6}Torr. Next, the crucible was heated to 250-280^{o}C so that Se pellets start to evaporate. The substrate temperature was set to 55-60^{o}C and once the deposition rate stabilized at about 1μm per minute the shutter was opened and a 15μm-think a-Se layer was produced in about 15-20min. The a-Se samples were then left at substrate temperature until the chamber was cooled down and the films were removed. Sample

thickness was measured directly using a Dektak-150 on one of the samples form a given deposition run. The thickness of the samples used for PD and PC studies was 15.5μm. The structure of deposited a-Se was examined by means of Raman Spectroscopy to make sure that crystallization did not occur and that indeed a typical amorphous network was formed.

A.2. a-Ge_xSe_{100-x} deposition

Amorphous Ge_xSe_{100-x} films for the PD/PB study were deposited in Boise State University onto ITO-coated glass substrates from a previously synthesized ChGs. Various compositions of bulk Ge_xSe_{100-x} glasses were synthesized by first combining raw Ge and Se martials in chosen amounts. The raw materials were sealed inside a fused silica ampoule under vacuum. The sealed ampoule was loaded into a furnace and the temperature was slowly increased to the melting temperature of the raw materials. While the furnace was heating up, the ampoule was agitated frequently to ensure good uniformity. After the material had been melted it was quenched in water to preserve the amorphous state of the ChG. Later, a-Ge_xSe_{100-x} films were deposited using a Cressington 308R thermal evaporation system at a pressure of 10^{-6}Torr with a semi-Knudsen cell crucible to increase the homogeneity across the film. Previous studies have shown compositional and structural homogeneity throughout the films' depth [203]. The composition of the films was determined at five locations of each sample by Energy Dispersion X-ray Spectroscopy using a Hitachi S-3400N-II scanning electron microscope equipped with an Oxford Instruments Energy + X-ray detector. It has been established that the pure Ge-Se films contain 29.2, 32.1, 39.5 atomic percent of Ge, with Se adding to 100 atomic percent for each particular composition. Film thickness ranged from 1.0 to 1.5μm.

APPENDIX B. List of Publications and Presentations from Thesis Research

B.1. Journal publications

- A. Mishchenko, J. Berashevich, K. Wolf, A. Reznik, D. A. Tenne and M. Mitkova, "Dynamic variations of the light-induced effects in a-Ge_xSe_{100-x} films: Experiment and Simulation", *Optical Materials Express* 5(2), 295-306 (2015).
- A. Mishchenko, G. P. Lindberg, B. A. Weinstein, and A. Reznik, "Comparative study of the photodarkening relaxation-kinetics in amorphous selenium for above-bandgap and sub-bandgap illumination", *Appl. Phys. Lett*. 105, 051912 (2014).
- J. Berashevich, A. Mishchenko, and A. Reznik, "Two-Step Photoexcitation Mechanism in Amorphous Se", *Phys. Rev. Appl.* 1, 034008 (2014).
- G. P. Lindberg, T. O'Loughlin, N. Gross, A. Mishchenko, A. Reznik, S. Abbaszadeh, K. S. Karim, G. Belev, and B. A. Weinstein, "Photo-crystallization in a-Se layer structures: Effects of film-substrate interface-rigidity", *J. of Appl. Phys.* 116, 193511 (2014).

B.2. Conference presentations

- A. Mishchenko, O. Tousignant, A. Teymurazyan, A. Ravi, A. Reznik, "Gamma-Camera for Image-guided Low-energy Breast Brachytherapy", 100th Annual Meeting of Radiological Society of North America, Oral Presentation, Presenting Author (USA, Chicago 2014).
- A. Mishchenko, O. Tousignant, A. Teymurazyan, A. Ravi, J-P. Pignol, J. A. Rowlands, A. Reznik "Gamma-camera for Image-guided Low-energy Breast Brachytherapy", the 12th International Workshop on Breast Imaging, Poster presentation, Presenting author (Gifu, Japan 2014).
- A. Mishchenko "Photodarkening kinetics in amorphous selenium", Graduate Student Conference, Lakehead University, Oral Presentation, Presenting author (Thunder Bay, Canada 2014).
- A. Mishchenko, J. Berashevich, A. Reznik, "Temperature dependence of photodarkening in stabilized a-Se", the 25th International Conference on Amorphous and Nano-crystalline Semiconductors, Oral Presentation, Presenting Author (Toronto, Canada 2013).
- A. Mishchenko, K. Wolf, M. Mitkova, A. Reznik, "Photodarkening vs. photobleaching in amorphous Ge_xSe_{1-x} films", the 25th International Conference on Amorphous and Nano-crystalline Semiconductors, Poster presentation, Presenting author (Toronto, Canada 2013).

REFERENCES

[1] B. T. Kolomiets, "Vitreous Semiconductors (II)†," Phys. Stat. Solidi (b) 7(3), 713-731 (1964).

[2] J. Singh and K. Shimakawa, *Advances in Amorphous Semiconductors, Vol.5* (Taylor & Francis, 2003).

[3] A. Zakery, S. R. Elliott, "Optical properties and applications of chalcogenide glasses: a review," J. Non-Cryst. Solids 330(1-3), 1-12 (2003).

[4] M. Wuttig, N. Yamada, "Phase-change materials for rewriteable data storage," Nature Materials 6(11), 824-832 (2007).

[5] S. Kasap, J. B. Frey, G. Belev, O. Tousignant, H. Mani, L. Laperriere, A. Reznik, J.A. Rowlands, "Amorphous selenium and its alloys from early xeroradiography to high resolution X-ray image detectors and ultrasensitive imaging tubes," Phys. Status Solidi B 246 (8), 1794-1805 (2009).

[6] N. F. Mott and E. A. Davis, *Electronic Processes in Non-Crystalline Materials,* edited by W. Marshall, D. H. Wilkinson (Oxford University Press, 1979).

[7] S. R. Ovshinsky, "Reversible Electrical Switching Phenomena in Disordered Structures," Phys. Rev. Lett., 21, 1450 (1968).

[8] M. Wuttig, N. Yamada,"Phase-change materials for rewriteable data storage," Nature Materials 6(11), pp. 824-832 (2007).

[9] B. J. Benjamin J. Eggleton, B. Luther-Davies, K. Richardson, "Chalcogenide photonics," Nat. Photonics 5, 141-148 (2011).

[10] *Xerox 914*. Available (Sept 2016): http://www.xerox.com/about-xerox/history-timeline/1950-decade/enus.html

[11] J. Mort, *The Anatomy of Xerography: Its Invention and Evolution* (McFarland & Company, 1989).

[12] J. W. Boag, "Xeroradiography," Phys. Med. Biol. 18(1), 3-37 (1973).

[13] U. Neitzel, I. Maack, S. Gunther-Kohfahl, “Image quality of a digital chest radiography system based on a selenium detector,” Med. Phys. 12(4), 509-516 (1994).

[14] A. R. Cowen, S. M. Kengyelics, A. G. Davies, “Solid-state, flat-panel, digital radiography detectors and their physical imaging characteristics,” Clin. Radiol. 63(5), 487-498 (2008).

[15] M. J. Powell, I. D. French, J. R. Hughes et al. “Amorphous silicon image sensor arrays,” Mater. Res. Soc. Symp. Proc. 258, 1127-1137 (1992).

[16] *XLV Company profile*. Available (Sept 2016): http://xlvdiagnostics.com/

[17] J. A. Rowlands, C. A. Webster, I. Koprinarov, P. Oakham, K. C. Schad, T. Szeto, S. Germann, “Low cost digital radiographic imaging systems: The x-ray light valve,” *Medical Imaging 2006: Physics of Medical Imaging*, edited by M. J. Flynn, J. Hsieh (Proceedings of SPIE Vol. 6142, 2006).

[18] S. Marcovici, V. Sukhovatkin, P. Oakham, “X-ray light valve (XLV): a novel detectors’ technology for digital mammography,” *Medical Imaging 2014: Physics of Medical Imaging*, edited by B.R. Whiting, C. Hoeschen (Proceedings of SPIE Vol. 9033, 2014).

[19] G. Juska and K. Arlauskas, "Impact ionization and mobilities of charge carriers at high electric fields in amorphous selenium,” Phys. Satatus Solidi A 59(1), 389-393 (1980).

[20] J. R. Scheuermann, A. H. Goldan, O. Tousignant, S. Léveillé, and W. Zhao, “Development of solid-state avalanche amorphous selenium for medical imaging,” Med. Phys. 42(3), 1223 (2015).

[21] A. V. Kolobov, J. Tominaga, *Chalcogenides Metastability and Phase Change Phenomena*, *Vol 164* (Springer Series in Materials Science, 2012).

[22] A. Reznik, B. J. M. Lui, J. A. Rowlands, S. D. Baranovskii, O. Rubel, V. Lyubin, M. Klebanov, S. O. Kasap, Y. Ohkawa, T. Matsubara, K. Miyakawa, M. Kubota, K.

Tanioka, T. Kawai, "Kinetics of photostructural changes in a-Se films," J. Appl. Phys. 100, 113506 (2006).

[23] J. Rowlands, S. Kasap, "Amorphous Semiconductors Usher in Digital X-Ray Imaging," Physics Today 50(11), 24-30 (1997).

[24] W. Zhao, G. DeCrescenzo, S. O. Kasap, J. A. Rowlands, "Ghosting caused by bulk charge trapping in direct conversion flat-panel detectors using amorphous selenium," Med. Phys. 32(2), 488-500 (2005).

[25] J. Berashevich, A. Mishchenko, A. Reznik, "Two-Step Photoexcitation Mechanism in Amorphous Se", Phys. Rev. Appl. 1, 034008 (2014).

[26] V. S. Minaev , S. P. Timoshenkov, V. V. Kalugin, "Structural and phase transformations in condensed selenium" J. Optoelectron. Adv. M. 7(4), 1717–1741 (2005).

[27] W. Freyland, A. Goltzene**,** et al. *Physics of Non-Tetrahedrally Bonded Elements and Binary Compounds I* , edited by C. Madelung (Springer-Verlag, 1983).

[28] R. Zallen, *Physics of Amorphous Solids*, (Wiley-VCH Verlag GmbH, 1988).

[29] *Hexagonal selenium*. Available (Sept 2016): https://en.wikipedia.org/wiki/Selenium#/media/File:Selenium_trigonal.jpg

[30] *Monoclinic α selenium*. Available (Sept 2016): https://commons.wikimedia.org/wiki/File:Selenium-alpha-monoclinic-unit-cell-3D-balls.png

[31] Proceedings of the International Symposium, Montreal, Canada, Oct 12-13, 1967, *The physics of selenium and tellurium*, edited by W.C. Cooper, (Pergamon Press, 1969).

[32] S. N. Yannopoulos, K. S. Andrikopoulos, "Raman scattering study on structural and dynamic features of noncrystalline selenium," J. Chem. Phys. 121, 4747 (2004).

[33] M. A. Popescu, *Non-Crystalline Chalcogenides* (Kluwer Academic Publishers, 2000), Ch. 1.

[34] S. O. Kasap, in *Handbook of Medical Imaging Materials*, edited by. A.S. Diamond and D.S. Weiss, 2nd ed. (Marcel Dekker, 2002).

[35] A. V. Tobolsky, A. Eisenberg, "Equilibrium polymerization of Sulphur," J. Am. Chern. Soc. 81(4), 780-782 (1959).

[36] A. Eisenberg, A. V. Tobolsky, "Equilibrium polymerization of Selenium," J. Polymer Sci. 46 (147), 19-28 (1960).

[37] A. T. Ward, "Raman spectroscopy of sulphur, sulphur-selenium, and sulphur-arsenic mixtures," J. Phys. Chem.72 (12), 4133-4139 (1968).

[38] G. Lucovsky, A. Mooradian, W. Taylor, G. B. Wright, R. C. Keezer, "Identification of the fundamental vibrational modes of trigonal, α-monoclinic and amorphous selenium," Solid State Commun. 5(2), 113-117 (1967).

[39] G. Lucovsky, in *Proceedings of the International Conference on the Physics of Selenium and Tellurium*, edited by E. Gerlach and P. Grosse (Springer-Verlag, 1979).

[40] P. Andonov, "Studies of non-crystalline forms of selenium," J. Non-Cryst. Solids 47(3), 297-339 (1982).

[41] J. Hegedus, K. Kohary, D. G. Pettifor, K. Shimakawa, and S. Kugler,"Photoinduced volume changes in amorphous selenium," Phys. Rev. Lett. 95, 206803 (2005).

[42] A. V. Kolobov, H. Oyanagi, K. Tanaka and K. Tanaka, "Structural study of amorphous selenium by in situ EXAFS: Observation of photoinduced bond alteration," Phys. Rev. B 55(2), 726-734 (1997).

[43] T. Scopigno, W. Steurer, S. N. Yannopoulos, A. Chrissanthopoulos, M. Krisch, G. Ruocco, and T. Wagner, "Vibrational dynamics and surface structure of amorphous selenium," Nat. Commun. 2, 195 (2011).

[44] D. Hohl and R. O. Jones, "First-principles molecular dynamics simulation of liquid and amorphous selenium," Phys. Rev. B 43, 3856 (1991).

[45] R. Zallen, G. Lucovsky, in: *Selenium*, edited by R. A. Zingaro, W. C. Cooper (Van Nostrand Reinhold, 1976), Ch. 4.

[46] R. E. Tallman, B. A. Weinstein, A. Reznik, M. Kubota, K.Tanioka, J. A. Rowlands, "Photo-crystallization in a-Se imaging targets: Raman studies of competing effects," J. Non-Cryst. Solids 354, 4577-4581 (2008).

[47] K. Nakamura and A. Ikawa, "Medium-range order in amorphous selenium: Molecular dynamics simulations," Phys. Rev. B 67, 104203 (2003).

[48] W. E. Spear, "Drift mobility techniques for the study of electrical transport properties in insulating solids," J. Non-Cryst. Solids 1(3), 197-214 (1969) and ref. therein.

[49] G. Juska, S. Vengris, "The hole mobility at the verification temperature in amorphous selenium," Phys. Stat. Solidi A 16(1), 27-29 (1973).

[50] M. Abkowitz, S. S Badesha, F. E. Knier, "Reversible chemical modification of the electrical behaviour of a-Se," Solid State Commun. 57(8), 579-582 (1986).

[51] M. Abkowitz, "Density of states in a-Se from combined analysis of xerographic potentials and transient transport data," Phil. Mag. Lett. 1 (58), 53-57 (1988).

[52] S. O. Kasap and C. Juhasz, "Time-of-flight drift mobility measurements on chlorine-doped amorphous selenium films," J. Phys. D 18(4), 703 (1985).

[53] T. J. Orlowski and M. Abkowitz, "Microstripline transient photocurrents in a-Se: Structure resolved in shallow band-tail states," Solid St. Commun. 59(10), 665-668 (1986).

[54] H.-Z. Song, G. J. Adriaenssens, E. V. Emelianova, V. I. Arkhipov, "Distribution of gap states in amorphous selenium thin films," Phys. Rev. B 59, 10607 (1999).

[55] S. Kasap, J. A. Rowlands, K. Tanioka, A. Nathan, in *Charge Transport in Disordered Solids with Applications in Electronics*, edited by S. Baranovski (Wiley & Sons, 2006), Ch4.

[56] S. Kasap et al. "Charge transport in pure and stabilized amorphous selenium: re-examination of the density of states distribution in the mobility gap and the role of defects," J Mater Sci: Mater Electron 26, 4644-4658 (2015).

[57] A. V. Kolobov, *Photo-induced Metastability in Amorphous Semiconductors*, (WILEY-VCH Weinheim, 2003), Ch.1.

[58] A. Street, *Hydrogenated Amorphous Silicon*, edited by R.W.Cahn, E.A. Davis, I. M. Ward (Cambridge University Press, 1991).

[59] M. Abkowitz, "On the Question of Chain-End ESR in Amorphous Selenium," J. Chem. Phys. 46, 4537 (1967).

[60] S. C. Agarwal, "Nature of Localized States in Amorphous Semiconductors - A Study by Electron Spin Resonance," Phys. Rev. B. 7, 685 (1973).

[61] P. W. Anderson, "Absence of Diffusion in Certain Random Lattices," Phys. Rev. 109, 1492 (1958).

[62] N. F. Mott "The increase in the conductivity of chalcogenide glasses by the addition of certain impurities," Phil. Mag. 34 1011 (1976).

[63] R. A. Street, N. F. Mott, "States in the Gap in Glassy Semiconductors," Phys. Rev. Lett. 35, 1293 (1975).

[64] M. Kastner, D. Adler, H. Fritzsche, "Valence-Alternation Model for Localized Gap States in Lone-Pair Semiconductors," Phys. Rev. Lett. 37, 1504 (1976).

[65] P. W. Anderson, "Model for the Electronic Structure of Amorphous Semiconductors," Phys. Rev. Lett. 34, 953 (1975).

[66] P. Boolchand, K. Gunasekera, S. Blosle, "Midgap states, Raman scattering, glass homogeneity, percolative rigidity and stress transitions in chalcogenides," Phys. Status Solidi B, 1-6 (2012).

[67] L. Lyubin, M. Klebanov, A. Bruner, N. Shitrit, B. Sfez, "Transient photodarkening and photobleaching in glassy $GeSe_2$ films," Optical Materials 33(6), 949-952 (2011).

[68] Q. Yan, H. Jain, J. Ren, D. Zhao, G. Chen, "Effect of Photo-Oxidation on Photobleaching of $GeSe_2$ and Ge_2Se_3 Films," J. Phys. Chem. 115, 21390-21395 (2011).

[69] A. R. Barik, M. Bapna, D. A. Drabold, K. V. Adarsh, "Ultrafast light induced unusually broad transient absorption in the sub-bandgap region of $GeSe_2$ thin films," Scientific Reports 4, 3686 (2014).

[70] K. Shimakawa, A. Kolobov, and S. R. Elliot, "Photoinduced effects and metastability in amorphous semiconductors and insulators," Adv. Phys. 44(6), 475-588 (1995).

[71] M. N. Kozicki, M. Mitkova, J. Zhu, and M. Park, "Nanoscale phase separation in Ag-Ge-Se glasses," Microelectron. Eng. 63, 155-159 (2002).

[72] T. Kohoutek, T. Wagner, J. Orava, M. Krabal, J. Ilavsky, M. Vlcek, and M. Fumar, "Multilayer planar structures prepared from chalcogenide thin films of As-Se and Ge-Se systems and polymer thin films using thermal evaporation and spin-coating techniques," J. Non-Cryst. Solids 354, 529-532 (2008).

[73] E. Bychkov, C. J. Benmore, D. L. Price, "Compositional changes of the first sharp diffraction peak in binary selenide glasses," Phys. Rev. B 72, 172107 (2005).

[74] I. Petri, P. S. Salmon, H. E. Fischer, "Defects in a Disordered World: The Structure of Glassy $GeSe_2$,"Phys. Rev. Lett. 84, 2413 (2000).

[75] K. Jackson, A. Briley, S. Grossman, D. V. Porezag; M. R. Pederson, "Raman –active modes of a-$GeSe_2$ and a-GeS_2: A First-Principles Study," Phys. Rev. B 60(22), 14985 (1999).

[76] S. Sugai, "Stochatic random network model in Ge and Si chalcogenide glasses," Phys. Rev. B 35, 1345 (1987).

[77] P. Boolchand, W. J. Bresser, "Structural Origin of Broken Chemical Order in $GeSe_2$ Glass," Philos. Mag. B 80, 1757 (2000).

[78] P. Boolchand, X. Feng, W. J. Bresser "Rigidity transitions in binary Ge-Se glasses and the intermediate phase," J. Non- Cryst. Solids 293-295, 348-356 (2001).

[79] M. Micoulaut, A. Kachmar, M. Bauchy, S. Le Roux, C. Massobrio, and M. Boero, "Structure, topology, rings, and vibrational and electronic properties of Ge_xSe_{1-x}

glasses across the rigidity transition: A numerical study," Phys. Rev. B. 88, 054203 (2013).

[80] S. Bhosle, K. Gunasekera, P. Chen, P. Boolchand, M. Micoulaut, and C. Massobrio, "Meeting experimental challenges to physics of network glasses: Assessing the role of sample homogeneity," Solid State Commun. 151(24), 1851-1855 (2011).

[81] T. G. Edwards, S. Sen, "Structure and Relaxation in Germanium Selenide Glasses and Supercooled Liquids: A Raman Spectroscopic Study," J. Phys. Chem. B 115, 4307-4313 (2011).

[82] A. Mishchenko, J. Berashevich, K. Wolf, A. Reznik, D.A. Tenne, M. Mitkova, "Dynamic variations of the light-induced effects in a-Ge_xSe_{100-x} films: experiment and simulation," Optical Materials Express 5(2), 295-306 (2015).

[83] E. Bergignat, G. Hollinger, H. Chermette, P. Pertosa, D. Lohez, M. Lannoo, and M. Bensoussan, "Electronic-structure and local-order study of Ge_xSe_{1-x} glasses," Phys. Rev. B 37, 4506 (1988).

[84] K. Inoue, T. Katayama, K. Kawamoto, and K. Murase, "Electronic structure of $GeSe_2$ in crystalline, amorphous, and Ag-photodoped amorphous phases studied by photoemission and optical spectra," Phys. Rev. B 35, 7496 (1987).

[85] R. Golovchak, O. Shpotyuk, S. Kozyukhin, A. Kovalskiy, A. C. Miller, and H. Jain, "Structural paradigm of Se-rich Ge-Se glasses by high-resolution X-ray photoelectron spectroscopy," J. Appl. Phys. 105, 103704 (2009).

[86] K. E. Asatryan, S. Frederick, T. Galstian, and R. Vallee, "Recording of polarization holograms in photodarkened amorphous chalcogenide films," Appl. Phys. Lett. 84(10), 1626-1628 (2004).

[87] M. L. Trunov, P. M. Lytvyn, S. N. Yannopoulos, I. A. Szabo, and S. Kokenyesi, "Photoinduced mass-transport based holographic recording of surface relief gratings in amorphous selenium films," Appl. Phys. Lett. 99 (5), 051906 (2011).

[88] M. Hughes, W. Yang, and D. Hewak, "Fabrication and characterization of femptosecond laser written waveguides in chalcogenide glass," Appl. Phys. Lett. 90(13), 131113 (2007).

[89] R. Chang, "Changes in the electronic states of vitreous selenium upon light radiation and plastic deformation,"Mater. Res. Bull. 2, 145-153 (1967).

[90] H. Hamanaka, K. Tanaka, S. Iizima, "Reversible photostructural change in melt-quench As_2S_3 glass," Solid State Commun. 23, 63-65 (1977).

[91] A. Ganjoo, K. Shimakawa, K. Kitano, E. A. Davis, "Transient photodarkening in amorphous chalcogenides," J. Non-Cryst. Sol. 299-302, 917-923 (2002).

[92] A. Reznik, S. Baranovskii, M. Klebanov, V. Lyubin, O. Rubel, J. A. Rowlands, "Reversible vs. Irreversible photodarkening in a-Se: the kinetics study," J Mater Sci: Mater. Electron 20, 111-115 (2009).

[93] Z. U. Borisova, *Glassy Semiconductors* (Plenum, New York, 1981).

[94] S. O. Kasap, C. Juhansz, "Kinematical transformations in amorphous selenium alloys used in xerography," J. Mater. Sci. 21(4),1329-1340 (1986).

[95] A. V. Kolobov, K. Tanaka, "Nanoscale mechanism of photo-induced metastability and reversible photodarkening in chalcogenide vitreous semiconductors," Sov. Phys. – Semiconductors 32(8), 899-904 (1998).

[96] M. Fumar, A. P. Firth, and A. E. Owen, "Reversible photodarkening and structural changes in As_2S_3 thin films," Philos. Mag. B 50(4), 463 (1984).

[97] L. F. Gladden, S. R. Elliott, and G. N. Greaves, "Photostructural changes in bulk chalcogenide glasses: An EXAFS study," J. Non-Cryst. Solids 106, 189-192 (1988).

[98] R. A. Street, "Non-radiative recombination in chalcogenide glasses," Solid State Communications, 24, 363-365 (1977).

[99] K. Tanaka, "Mechanisms of photodarkening in amorphous chalcogenides", J. Non-Cryst. Solids 59&60, 925–928 (1983).

[100] K. Tanaka, "Transient-grating study of amorphous As_2S_3 films," J. Appl. Phys. 65, 2042 (1989).

[101] V. K. Tikhomirov, G. J. Adriaenssens, S. R. Elliott, "Temperature dependence of the photoinduced anisotropy in chalcogenide glasses: Activation energies and their interpretation," Phys. Rev. B55, R660-R663 (1997).

[102] V. L. Averianov, A. V. Kolobov, B. T. Kolomiets, and V. M. Lyubin,"Thermal and optical bleaching in darkened films of chalcogenide vitreous semiconductors," Phys. Stat. Sol. A 57(1), 81-88 (1980).

[103] K. Tanaka and A. Odajima, "Photodarkening in amorphous selenium," Solid State Communications, 43 (12), 961-964 (1982).

[104] K. Shimakawa., S. Inami, S. R. Elliott, "Reversible photoinduced change of photoconductivity in amorphous chalcogenide films," Phys. Rev. B 42, 11857 (1990).

[105] H. Fritzsche, "The origin of reversible and irreversible photostructural changes in chalcogenide glasses," Philos. Mag. B. 68(4), 561-572 (1993).

[106] V. K.Tikhomirov , S. R. Elliot, "Model for photoinduced anisotropy and its dark relaxation in chalcogenide glasses", Rapid Communications 51(8), 5538-5541 (1995).

[107] D. K. Biegelsen, R. A. Street, "Photoinduced Defects in Chalcogenide glasses," Phys. Rev. Lett. 44(12), 803-806 (1980).

[108] A. Gonjoo, K. Shimakawa, "Dynamics of photodarkening in amorphous chalcogenides," J. Optoelectron, Adv. Mater. 4(3), 595-604 (2002).

[109] K. Tanaka and K. Shimakawa, *Amorphous Chalcogenide Semiconductors and Related Materials* (Springer, 2011).

[110] K. S. Kim and D. Turnbull, "Crystallization of amorphous selenium films. I. Morphology and kinetics," J. Appl. Phys. 44(12), 5237–5244 (1973).

[111] K. S. Kim and D. Turnbull, "Crystallization of amorphous selenium films. II. Photo and impurity effects," J. Appl. Phys. 45(8), 3447–3452 (1974).

[112] R. Clement, J. C. Carballes, and B. de Cremoux, "The photo-crystallization of amorphous selenium thin films," J. Non-Cryst. Solids 15(3), 505–516 (1974).

[113] G. Gross, R. B. Stephens, and D. Turnbull, “On the crystallization of amorphous selenium films: Thermal effects and photoeffects,” J. Appl. Phys. 48(3), 1139–1148 (1977).

[114] R. B. Stephens, “Stress-enhanced crystallization in amorphous selenium films,” J. Appl. Phys. 51(12), 6197 (1980).

[115] A. A. Baganich, V. I. Mikla, D. G. Semak, A. P. Sokolov, and A. P.Shebanin, “Raman Scattering in Amorphous Selenium Molecular Structure and Photoinduced Crystallization,” Phys. Status Solidi B 166(1), 297–302 (1991).

[116] V. V. Poborchii, A. V. Kolobov, and K. Tanaka, “An *in situ* Raman study of polarization-dependent photocrystallization in amorphous selenium films,” Appl. Phys. Lett. 72(10), 1167 (1998).

[117] A. Roy, A.V. Kolobov, and K. Tanaka, “Laser-induced suppression of photocrystallization rate in amorphous selenium films,” J. Appl. Phys. 83(9), 4951–4956 (1998).

[118] V. K. Tikhomirov, P. Hertogen, G. J. Adriaenssens, C. Glorieux, and R. Ottenburgs, “Anisotropic laser crystallization of a-Se,” J. Non-Cryst. Solids 227–230, 732–738 (1998).

[119] T. Innami and S. Adachi, “Structural and optical properties of photocrystallized Se films,” Phys. Rev. B 60(11), 8284–8289 (1999).

[120] H. Fritzsche, “The origin of reversible and irreversible photostructural changes in chalcogenide glasses,” Philos. Mag. B 68(4), 561–572 (1993).

[121] G. P. Lindberg, T. O’Loughlin, N. Gross, A. Reznik, S. Abbaszadeh, K. S. Karim, G. Belev, D. M. Hunter, and B. A. Weinstein, “Raman mapping studies of photo-induced crystallization in a-Se films: substrate strain and thermal effects,” Can. J. Phys. 92(7/8), 728–731 (2014).

[122] R. E. Tallman, A. Reznik, B. A. Weinstein, S. D. Baranovskii, and J. A. Rowlands, “Similarities in kinetics of photocrystallization and photodarkening in a-Se,” Appl. Phys. Lett. 93, 212103 (2008).

[123] A. Mishchenko, G. P. Lindberg, B. A. Weinstein, and A. Reznik, “Comparative study of the photodarkening relaxation-kinetics in amorphous selenium for above-bandgap and sub-bandgap illumination,” Appl. Phys. Lett. 105, 051912 (2014).

[124] G. P. Lindberg, T. O'Loughlin, N. Gross, A. Mishchenko, A. Reznik, S. Abbaszadeh, K. S. Karim, G. Belev, and B. A. Weinstein, "Photo-crystallization in a-Se layer structures: Effects of film-substrate interface-rigidity," J. of Appl. Phys. 116, 193511 (2014).

[125] H. Fritzsche, “Light Induced Structural Changes in Glasses,” in *Insulating and Semiconducting Glasses*, ed. by P.Boolchand, (World Scientific, 2000).

[126] G. Chen, H. Jain, S. Khalid, J. Li, D. A. Drabold, and S. R. Elliott, “Study of structural changes in amorphous As_2Se_3 by EXAFS under in situ laser irradiation,” Solid State Commun. 120(4), 149–153 (2001).

[127] S. R. Elliott, “A unified Model of Reversible Photostructural Effects in Chalcogenide Glasses,” J. Non-Cryst. Solids 81(1-2), 71–98 (1986).

[128] Q. Liu and F. Gan, “Photobleaching in Amorphous GeS_2 Thin Films,” Mater. Lett. 53(6), 411–414 (2002).

[129] P. Nemec, J. Jedelsky, M. Frumar, M. Stabl, Z. Cernosek, and M. Vlcek, “Amorphous Ge-Se thin films prepared by pulsed-laser deposition,” Philos. Mag. 84(9), 877–885 (2004).

[130] R. A. Street, R. J. Nemanich and G. A. N. Connell, “Thermally induced effects in evaporated chalcogenide films. II. Optical absorption,” Phys. Rev. B, Vol. 18, N.12 (1978).

[131] C. A. Spence and S. R. Elliott, “Light-induced oxidation and band-edge shifts in thermally evaporated films of germanium chalcogenide glasses,” Phys. Rev. B Condens. Matter 39(8), 5452–5463 (1989).

[132] L. Tichy, A. Triska, H. Ticha, and N. Frumar, “On the nature of bleaching of Ge30Se70 films,” Philos. Mag. B 54, 219–230 (1986).

[133] L. Tichý, H. Ticha, and K. Handlir, “Photoinduced changes of optical properties of amorphous chalcogenide films at ambient air pressure,” J. Non-Cryst. Solids 97-98, 1227–1230 (1987).

[134] S. Rajagopalan, K. S. Harshavardhan, L. K. Malhotra, and K. L. Chopra, “Photo-Optical Changes In Ge- Chalcogenide Films,” J. Non-Cryst. Solids 50(1), 29–38 (1982).

[135] K. S. Harshavardhan and M. S. Hegde, “Origin of Anomalous Photoinduced Transformations in Amorphous Ge-Based Chalcogenide Thin Films,” Phys. Rev. Lett. 58(6), 567–570 (1987).

[136] T. Kawagichi, S. Maruno, and Ke. Tanaka, “Compositional dependence of photoinduced and thermally induced bleaching of amorphous Ge-S and Ge-S-Ag films,” J. Appl. Phys. 73(9), 4560–4566 (1993).

[137] E. Flaxer, M. Klebanov, D. Abrahamoff, S. Noah, V. Lyubin, “Photodarkening of AsSe glassy films under μs light pulses,” Optical Materials 31, 688-690 (2009).

[138] R. Kumar, A. Barik, E. Vinod, M. Bapna, K. Sangunni, and K. Adarsh, "Crossover from photodarkening to photobleaching in a-Ge_xSe_{100-x} thin films," Opt. Lett. 38, 1682-1684 (2013).

[139] D. Arsova, E. Vateva, “Dual action of light in photodarkened Ge-As-S films,” Phys. Stat. Sol. (B) 249, 153–157 (2012).

[140] R. M. Martin, G. Lucovsky, and K. Helliwell, “Intermolecular bonding and lattice dynamics of selenium and tellurium,” Phys. Rev. B 13(4), 1383-1395 (1976).

[141] D. E. Ackley, J. Tauc, W. Paul, “Picosecond relaxation of optically induced absorption in amorphous semiconductors,” Phys. Rev. Lett. 43, 715-718 (1979).

[142] C. Tsang, R. A. Street, “Recombination in plasma-deposited amorphous Si:H. Luminescence decay,” Phys. Rev. B 19, 3027-3040 (1979).

[143] P. Blaha, K. Schwarz, G. K. H. Madsen, D. Kvasnicka, and J. Luitz, Wien2k: An Augmented Plane Wave+Local Orbitals Program for Calculating Crystal Properties: Karlheinz Schwarz (Technische Universität, Wien, Austria, 2001).

[144] J. P. Perdew, K. Burke, and M. Ernzernof, "Generalized Gradient Approximation Made Simple," Phys. Rev. Lett. 77(18), 3865-3868 (1996).

[145] A.V. Kolobov, M. Kondo, H. Oyanagi, A. Matsuda, and K. Tanaka, "Negative correlation energy and valence alternation in amorphous selenium: An in situ optically induced ESR study," Phys. Rev. B 58, 12004 (1998).

[146] K. Tanaka, "Photoexcitation in As_2S_3 glass," Phys. Rev. B 57, 5163 (1998).

[147] J. Dresner and G.B. Stringfellow, "Electronic process in the photo-crystallization of vitreous selenium," J. Phys. Chem. Solids 29(2), 303–311 (1968).

[148] M. L. Trunov, P. M. Lytvyn, S. N. Yannopoulos, I. A. Szabo, and S. Kokenyesi, "Photoinduced mass-transport based holographic recording of surface relief gratings in amorphous selenium films," Appl. Phys. Lett. 99(5), 051906 (2011).

[149] J. Hegedus, K. Kohary, D. G. Pettifor, K. Shimakawa, and S. Kugler, "Photoinduced Volume Changes in Amorphous Selenium," Phys. Rev. Lett. 95(20), 206803 (2005).

[150] R. Lukacs, M. Veres, K. Shimakawa, and S. Kugler, "On photoinduced volume change in amorphous selenium: Quantum chemical calculation and Raman spectroscopy," J. Appl. Phys. 107(7), 073517 (2010).

[151] S. Abbaszadeh, C. C. Scott, O. Bubon, A. Reznik, and K. S. Karim, "Enhanced detection efficiency of direct conversion X-ray detector using polyimide as hole-blocking layer," Sci. Rep. 3, 3360 (2013).

[152] P. J. Carroll and J. S. Lannin, "Raman Scattering of amorphous selenium films," Solid State Commun. 40(1), 81–84 (1981).

[153] A. Eisenberg and A. V. Tobolsky, "Equilibrium polymerization of selenium," J. Polymer Sci. 46(147), 19–28 (1960).

[154] J. C. Mauro and A. K. Varshneya, "Model interaction potentials for selenium from *ab initio* molecular simulations," Phys. Rev. B 71(21), 214105 (2005).

[155] S. Abbaszadeh, N. Allec, W. Kai, and K. S. Karim, "Low Dark-Current Amorphous-Selenium Metal-Semiconductor-Metal Photodetector," IEEE Electron Device Lett. 32(9), 1263–1265 (2011).

[156] C. R. Schardt, J. H. Simmons, P. Lucas, L. Le Neindre, and J. Lucas, "Photodarkening in Ge_3Se_{17} glass," J. Non-Cryst. Solids 274 (1-3), 23–29 (2000).

[157] P. M. Bridenbaugh, G. P. Espinosa, J. E. Griffiths, J. C. Phillips, and J. P. Remeika, "Microscopic origin of the companion A1 Raman line in glassy $Ge(S,Se)_2$," Phys. Rev. B 20(10), 4140–4144 (1979).

[158] P. S. Salmon, R. A. Martin, P. E. Mason, and G. J. Cuello, "Topological versus chemical ordering in network glasses at intermediate and extended length scales," Nature 435(7038), 75–78 (2005).

[159] K. Darmawikarta, T. Li, S. G. Bishop, and J. R. Abelson, "Two forms of nanoscale order in amorphous Ge_xSe_{1-x} alloys," Appl. Phys. Lett. 103(13), 131908 (2013).

[160] P. Khan, H. Jain, and K. V. Adarsh, "Role of Ge: As ratio in controlling the light-induced response of a-$Ge_xAs_{35-x}Se_{65}$ thin films," Sci Rep 4, 4029 (2014).

[161] J. L. Bosse, I. Grishin, Y. G. Choi, C. Byung-ki, S. Lee, O. V. Kolosov, and B. D. Huey, "Nanosecond switching in GeSe phase change memory films by atomic force microscopy," Appl. Phys. Lett. 104(5), 053109 (2014).

[162] M. Hoheisel, "Review of medical imaging with emphasis on X-ray detectors," Nuclear Instruments and Methods in Physics Research A 563, 215-224 (2006).

[163] J. A. Rowlands and J. Yorkston in *Handbook of Medical Imaging* Vol.1 Physics and Psychophysics, ed. by Jacob Beutel, Harold L. Kundel, Richard L. Van Metter, (SPIE Press, 2000) Ch. 4, p. 225.

[164] A. Oppelt (Ed.), *Imaging Systems for Medical Diagnosis* (Publicis Corporate Publishing, 2005).

[165] M. J. Powell, D. U. Wiechert, "PbO as direct conversion x-ray detector material," Proc. SPIE 5368, 188-199 (2004).

[166] M. Simon, R. A. Ford, A. R. Franklin, S.P. Grabowski, B. Mensor, G. Much, A. Nascetti, M. Overdick, M. J. Powell, D.U. Wiechert, "Analysis of lead oxide (PbO) layers for direct conversion X-ray detection," IEEE Trans. Nucl. Sci. 52, 2035-2040 (2005).

[167] S. Tokuda, H. Kishihara, S. Adachi, T. Sato, "Improvement of temporal response and output uniformity of polycrystalline CdZnTe films for high-sensitivity x-ray imaging," Proc. SPIE, 5030, 861-870 (2003).

[168] S. Tokuda, H. Kishihara, S. Adachi, T. Sato, "Preparation and characterization of polycrystalline CdZnTe films for large-area, high-sensitivity X-ray detectors," J. Mater. Sci. Mater. Electron. 5, 1-8 (2004).

[169] Q. Zhao, L. E. Antonuk, Y. El-Mohri, Y. Wang, H. Du, A. Sawant, Z. Sul, J. Yamamoto, "Performance evaluation of polycrystalline HgI_2 photoconductors for radiation therapy imaging," Med. Phys. 37, 2738-2748 (2010).

[170] H. Du, L. E. Antonuk, Y. El-Mohri, Q. Zhao, Z Sul, J. Yamamoto, Y. Wang, "Investigation of the signal behaviour at diagnostic energies of prototype, direct detection, active matrix, flat-panel imagers incorporating polycrystalline HgI_2," Phys. Med. Biol. 53, 1325-1351 (2010).

[171] S. Kasap, J. B. Frey, G. Belev, O. Tousignant, H. Mani, J. Greenspan, L. Laperriere, O. Bubon, A. Reznik, G. DeCrescenzo, K. S. Karim, J. A. Rowlands, "Amorphous and Polycrystalline Photoconductors for Direct Conversion Flat Panel X-ray Image Sensors," Sensors 11, 5112-5157 (2011).

[172] C. Haugen, S. O. Kasap, J. A. Rowlands, "Charge transport and electron-hole creation energy in stabilized a-Se x-ray photoconductors," J. Phys. D Appl. Phys. 32, 200-207 (1999).

[173] S. O. Kasap, J. A. Rowlands, "Direct-conversion flat-panel x-ray image detectors," IEEE Proc. Circ. Dev. Syst. 149, 85-96 (2002).

[174] B. Zhao, W. Zhao, "Imaging performance of an amorphous selenium digital mammography detector in a breast tomosynthesis system," Med. Phys. 35, 1978-1987 (2008).

[175] M. J. Yaffe, "Detectors for Digital Mammography" in *Digital Mammography* ed. by U. Bick, F. Diekmann (Springer, 2010), Ch.2.

[176] M .S. Sajid, U. Parampalli, Z. Haider, et al. "Comparison of radioguided occult lesion localization (ROLL) and wire localization for non-palpable breast cancers: A meta-analysis," J Surg Oncol 105, 852-858 (2012).

[177] P. Kelly, E. H. Winslow, "Needle wire localization for nonpalpable breast lesions: Sensations, anxiety levels, and informational needs," Oncl. Nurs. Forum 23, 639-645 (1996).

[178] P. Davis, R. Wechesler, "Migration of breast biopsy localization wire," Am. J. Roentgenol. 150(4), 787-788 (1988).

[179] A. Seili et al., "Migration of guidewire after surgical breast biopsy: An unusual case report," Cardiovasc. Intervent. Radiol. 32, 1087-1090 (2009).

[180] M. J. Homer "Transection of the localization hooked wire during breast biopsy," Am. J. Roengenol. 141(5), 929-30 (1983).

[181] J. S. Monterey, J. A. Levy, R. J. Brenner, "Wire fragments after needle localization," Am. J. Roengenol. 167(5),1267-9 (1996).

[182] L. Jacobs, "Positive margins: the challenge continues for breast surgeons," Ann. Surg. Oncol. 15,1271-2 (2008).

[183] J. W. Jakub, R. J. Gray, A. C. Degnim, J. C. Boughey, M. Gardner, C.E. Cox, "Current status of radioactive seed for localization of nonpalpable breast lesions," Am. J. Surg. 199(4), 522-28 (2010).

[184] D. B. Taylor et al. "Radioguided occult lesion localization using iodine-125 seeds ('ROLLIS') for removal of impalpable breast lesions: First Australian experience," Journal of Medical Imaging and Radiation Oncology 59(4), 411-20 (2015).

[185] R. J. Gray, C. Salud, K. Nguyen, et al., "Randomized prospective evaluation of a novel technique for biopsy or lumpectomy of nonpalpable breast lesions: Radioactive seed versus wire localization," Ann. Surg. Oncol. 8, 711-715 (2001).

[186] M. Ahmed, M. Douek, "Radioactive seed localization (RSL) in the treatment of non-palpable breast cancers: systematic review and meta-analysis," Breast, 22, 383-8 (2013).

[187] B. Pouw et al., "Heading Toward Radioactive Seed Localization in Non-Palpable Breast Cancer Surgery? A Meta-Analysis," J. Surg. Oncol. 111, 185-191 (2015).

[188] D. W. Arthur and F. A. Vicini, "Accelerated Partial Breast Irradiation As a Part of Breast Conservation Therapy," J. Clin. Oncol. 23 (8), 1726-1735 (2005).

[189] B. D. Smith et al., "Accelerated partial breast irradiation consensus statement from the American society for radiation oncology (ASTRO)," Int. J. Radiation Oncology Biol. Phys. 74(4), 987-1001 (2009).

[190] J-P. Pignol, B. Keller, E. Rakovitch, R. Sankreacha, H. Easton, W. Que, "First report of a permanent breast ^{103}Pd seed implant as adjuvant radiation treatment for early-stage breast cancer," Int. J. Rad, Oncol. Biol. Phys. 64(1), 176-181 (2006).

[191] B. Keller, R. Sankreacha, E. Rakovitch, P. O'Brien, J-P. Pignol, "A permanent breast seed implant as partial breast radiation therapy for early-stage patients: a comparison of Palladium-103 and Iodine-125 isotopes based on radiation safety considerations," Int. J. Radiation Oncology Biol. Phys., 62(2), 358-365 (2005).

[192] R. Nath, L. Anderson, G. Luxton, K. Weaver, J. Williamson and A. Meigooni, "Dosimetry of interstitial brachytherapy sources: Recommendations of the AAPM Radiation Therapy Committee Task Group No. 43," Med. Phys. 22, 209-234 (1995).

[193] A. Ravi, C. B. Caldwell, B. M. Keller, A. Reznik, J-P. Pignol,"Online gamma-camera imaging of 103Pd seeds (OGIPS) for permanent breast seed implantation," Phys. Med. Biol. 52, 5921-5932 (2007).

[194] B. Mueller. M. K. O'Connor, I. Blevis, D. J. Rhodes, R. Smith. D. A. Collins, S. W. Phillips, "Evaluation of a Small Cadmium Zinc Telluride Detector for Scintimammography," J. Nucl. Med. 44(4) 602-609 (2003).

[195] S. R. Cherry, J. A. Sorenson, M. E. Phelps, *Physics of Nuclear Medicine*, 3rd edition, (Elsevier Health Sciences, 2003).

[196] *AXS-2430*. Available (Sept 2016): http://www.analogic.com/products/digital-mammography/direct-conversion-x-ray-detectors

[197] *Nuclear Fields Collimators.* Available (Sept 2016): http://www.nuclearfields.com

[198] Mammography flat panel detector AXS-2430. Available (Sept 2016): http://www.medicalexpo.com/prod/analogic-canada-corporation-83542.html

[199] R. Grigorovici, "Amorphous semiconducting thin flms," This Solid Films 9(1), 1-23 (1971).

[200] W.C. Tan, G. Belev, K. Koughia, R. Johanson, S. K. O'Leary, S. Kasap, "Optical properties vacuum deposited and chlorine doped a-Se thin films: aging effects," J. Mater Sci: Mater Electron 18, 429-S433 (2007).

[201] G. C. Das, M. B. Bever, D. R. Uhlmann, S. C. Moss, "Relaxation phenomena in amorphous selenium-tellurium alloys," J. Non-Cryst. Solids 7, 251 (1972).

[202] M. Abkowitz, D.M. Pai, "Photoelectric behavior of a-Se and some a-Se: As alloys in their glass transition regions," Phys. Rev. B 18, 1741 (1978).

[203] M. Jin, P. Boolchand, and M. Mitkova, "Heterogeneity of molecular structure of Ag photo-diffused $Ge_{30}Se_{70}$ thin films," J. Non-Cryst. Solids 354 (19-25), 2719–2723 (2008).